SYNTHESIS AND CHARACTERIZATION OF ANODIC TITANIA NANOTUBES FOR SUPERCAPACITOR APPLICATION

ZULKARNAIN BIN ENDUT

**Thesis Submitted In Fulfillment Of The Requirement
For The Degree Of Doctor Of Philosophy**

**FACULTY OF ENGINEERING
UNIVERSITY OF MALAYA
KUALA LUMPUR**

2013

UNIVERSITY OF MALAYA

ORIGINAL LITERARY WORK DECLARATION

Name : **ZULKARNAIN BIN ENDUT** (I.C/Passport No.:

Registration / Matric No.: **KHA090070**

Name of Degree : **DOCTOR OF PHILOSOPHY IN ENGINEERING DESIGN**

Title of Project Paper/Research Report/Thesis (“this Work”)
Synthesis And Characterization Of Anodic Titania Nanotubes For Supercapacitor Application

I do solemnly and sincerely declare that :

(1) I am the sole author/writer of this Work;
(2) This Work is original;
(3) Any use of any work in which copyright exists was done by way of fair dealing and for permitted purposes and any excerpt or extract from, or reference to or reproduction of any copyright work has been disclosed expressly and sufficiently and the title of the Work and its authorship have been acknowledged in this Work;
(4) I do not have any actual knowledge nor do I ought reasonably to know that the making of this work constitutes an infringement of any copyright work;
(5) I hereby assign all and every rights in the copyright to this Work to the University of Malaya (“UM”), who henceforth shall be owner of the copyright in this Work and that any reproduction or use in any form or by any means whatsoever is prohibited without the written consent of UM having been first had and obtained;
(6) I am fully aware that if in the course of making this Work I have infringed any copyright whether intentionally or otherwise, I may be subject to legal action or any other action as may be determined by UM.

Candidate’s Signature Date :

Subscribed and solemnly declared before,

Witness’s Signature Date :

Name :

Designation :

ACKNOWLEDGEMENT

I would like to express my gratitude to Prof. Dr Wan Jeffrey and Prof Dr Mohd Hamdi Abd Shukor for being my supervisors and for his invaluable encouragement, support and guidance in completing this thesis. Your technical input during my research is highly appreciated. Also to my supervisor at Tokyo Institute of Technology, Prof. Dr. Atsushi Nishikata for helping me on investigating nanotubes formation.

I also want to thanks to MyBrain15 program (MyPhD) under Ministry of Higher Education (MOHE) for financial support during my study. Also to IPPP postgraduate fund, JASSO Scholarship and AOTULE during student exchange program at Tokyo Institute of Technology. I also wants to dedicate to faculty and department management on their support during my candidature.

Last but not least, I dedicate this work to my mother, Khatijah Bt Mustafa and all my family especially my lovely wife, Mazuin Bt Mustafa. I would like to express my heartfelt thanks to them for their moral support, love and encouragement during my research.

ABSTRAK

Tiub nano titania telah menarik perhatian banyak penyelidikan dalam bidang sains dan teknologi dari bidang bioperubatan hingga ke bidang penukaran tenaga. Ianya boleh disintesis menggunakan kaedah yang mudah dan berkos rendah seperti penganodan. Kaedah ini mampu menghasilkan tiub nano yang sangat teratur dan menawarkan ciri-ciri fizikal yang unik seperti kawasan permukaan spesifik yang tinggi, penggabungan semula elektron yang rendah dan pemindahan cas yang efisien. Kajian tesis ini melibatkan sintesis tiub nano titania dan applikasi tiub nano tersebut sebagai superkapasitor elektrod. Kajian ini melibatkan analisis struktur, morfologi, komposisi kimia dan prestasi kapasitans elektrokimia yang dikaji menggunakan alat pencirian seperti mikroskop pengimbasan elektron (FESEM), pembelauan sinar-x (XRD), spektroskopi fotoelektron sinar-x (XPS), voltammetri berkitar (CV), ujian galvanostatic caj dan nyahcas (CD), spektroskopi impedans elektrokimia (EIS) dan analisis Mott-Schottky. Mekanisme pembentukan dan pertumbuhan tiub nano sewaktu penganodan titanium dalam elektrolit NH_4F/ethylene glycol pada voltan 45 V telah dianalisa menggunakan FESEM.Peringkat awal penganodan, berlaku pembentukan lapisan oksida padat dengan lubang berskala nano. Apabila masa penganodan dipertingkatkan, lubang tersebut membesar dan lebih mendalam kerana berlaku integrasi liang kecil dan besar, yang akhirnya membentuk tiub nano titania. Struktur liang tersebut telah meningkatkan kapasitans elektrokimia daripada 18.3 $\mu F\ cm^{-2}$ untuk 10-s masa penganodan kepada 49.9 $\mu F\ cm^{-2}$ untuk 1800-s masa penganodan. Analisis CV menunjukkan bentuk simetri segiempat berubah bentuk kepada paksi-x simetri dimana ketumpatan arus yang lebih tinggi diperolehi.Ini berlaku kerana kawasan permukaan telah meningkat hasil dari struktur tiub nano yang digunakan. Saiz CV yang lebih besar di kawasan katod adalah merupakan ciri bahan separa konduktor berjenis *n* yang

menyerupai bahan titania ini seperti diterangkan dalam analisis Mott-Schottky. Pemanasan pada suhu tinggi dalam persekitaran gas ammonia telah digunakan untuk meningkatkan kekonduksian elektrik bahan ini. Dalam ujian ini, tiub nano titania disepuh lindap dalam persekitaran ammonia pada 500°C selama 3 jam. Selepas pemanasan ini, tiub nano telah bertukar menjadi struktur kristal anatase dan mempunyai kandungan Ti^{3+} yang tinggi. Selepas pengoptimuman proses penganodan menggunakan eksperimen Box-Behnken, masa nyahcas sebanyak 43.69 s dan kapasitan 145.6 μF cm^{-2} telah diperolehi. Kapasitan tiub nano titania dipertingkatkan lagi dengan menggunakan cecair ionik EMIM hidrogensulfat. Dengan menggunakan ujian cas dan nyahcas secara galvanostatik, kapasitan tiub nano titania dalam cecair ionik hidrogensulfat EMIM adalah 1.58 mF cm^{-2} telah diperolehi bagi ketumpatan arus 10 μA cm^{-2}. Peningkatan kapasitans ini boleh dijelaskan oleh teori kesesakan ion pada permukaan akibat menggunakan elektrolit berkepekatan tinggi seperti cecair ionik.

ABSTRACT

Over the past decade, titania nanotube materials have attracted increasing scientific and technological attention ranging from usage in the fields of biomedical applications to energy conversion. Titania nanotubes can be synthesized using a simple and low-cost self-organizing anodization method but is capable of producing highly ordered titania nanotube structures.This nanostructure grown directly on the conductive substrate can offer unique physical properties such as high specific surface area, lower electron recombination and excellent charge-transfer properties. Based on this motivation, this thesis attempts to synthesis, to apply, to investigate and to enhance this titania nanotubes as a binder-free supercapacitor electrode in which titanium foil can be used as a current collector while their nanotubular structure is used as charge storing and releasing area. The aim of this work is to study the structure, morphology, chemical composition and electrochemical capacitance performance by means of various characterization tools such as field emission scanning electron microscopy (FESEM), x-ray diffraction (XRD), x-ray photoelectron spectroscopy (XPS), cyclic voltammetry (CV), galvanostatic charge-discharge testing (CD), electrochemical impedance spectroscopy (EIS) and Mott-Schottky analysis. The thesis describes the mechanism of titania nanotube formation and growth during anodization of titanium in NH_4F/ethylene glycol electrolyte at 45 V applied voltage that was investigated using FESEM. The initial stage of the anodization occurs with the formation of a compact oxide layer with nanoscale pits. With the increase of anodization time, the pits transform to larger and deeper pores due to the integration of the smaller and larger pores, finally creating self-ordered titania nanotubes. The porous structure increases electrochemical capacitance from 18.3 $\mu F\ cm^{-2}$ for 10-s anodization time to 49.9 $\mu F\ cm^{-2}$ for 1800-s anodization time. The CV transforms from a near symmetry rectangular shape to *x*-axis symmetry with higher current density as the anodization time increases due to increased specific surface area of the nanotubular structure. The larger CV size at more cathodic region is characteristic of the *n*-type behavior of titania materials, as also shown in the Mott-Schottky analysis. Ammonia annealing is used to increase surface defect and improve electrical conductivity of this material. In this work, titania nanotubes are annealed in ammonia atmosphere at 500^{o}C for 3 hours, this bamboo-type titania nanotubes changed to anatase phase, and contained oxygen vacancies and Ti^{3+} oxidation state, thus, changed electrical conductivity of the titania nanotube surface. After anodization optimization of Ti foil using Box-Behnken design, the maximum discharge time of 43.69 s and specific capacitance of 145.6 μF cm^{-2} was obtained. The enhanced electrochemical performance of the titania nanotubes was obtained in EMIM hydrogensulfate ionic liquid. By using galvanostatic charge-discharge testing, the specific capacitance for this anodized titania nanotubes in EMIM hydrogensulfate is 1.58 mF cm^{-2} for current density 10 μA cm^{-2}. This greatly improved electrochemical capacitance can be explained by the crowding and overscreening theory, which is pronounced at small voltages and gradually replaced by the formation of a condensed layer of counterions, followed by complete lattice saturation at very large voltages.

CONTENTS

CHAPTER 1 : INTRODUCTION

CHAPTER 2 : LITERATURE REVIEW

CHAPTER 3 : RESEARCH METHODOLOGY

CHAPTER 4 : RESULTS AND DISCUSSIONS

CHAPTER 5 : CONCLUSION

APPENDIX A – LIST OF PUBLICATIONS

List of Figures

List of Tables

List of Abbreviations

Abbreviations	**Full Name**
FESEM	Field Effect Scanning Electron Microscopy
XRD	X-Ray Diffractometer
XPS	X-Ray Photoelectron Spectroscopy
CV	Cyclic Voltammetry
CD	Galvanostatic Charge Discharge
EIS	Electrochemical Impedance Spectroscopy
MS	Mott-Schottky Analysis
NH_4F	Ammonium Flouride
Ti	Titanium
EMIM	1-ethyl-3-methyl imidazolium
RSM	Response Surface Method
EDX	Energy Dispersive X-Ray
ANOVA	Analaysis of Variance
NiO	Nickel Oxide
KCl	Potassium Chloride
DI water	De-ionized water
NH_3	Ammonia
H_2SO_4	Sulfuric Acid
Na_2SO_4	Sodium Sulfate
3D	3-Dimensional
Li-ion	Lithium ion
O element	Oxygen element
PDA	Personal digital assistant
HEV	Hybrid electrical vehicles
EDLC	Electrical double layer capacitance

TiO_2	Titania
RuO_2	Ruthenium Oxide
Fe_3O_4	Ferum Oxide
MnO_2	Manganese Oxide
1D	1-Dimensional
KOH	Potassium Hydroxide
IL	Ionic liquid
CP	Chronopotentiometry
CPE	Constant Phase Element
FRA	Frequency Response Analyzer
F	Fluorine element
C	Carbon element
IR drop	Voltage drop
EG	Ethylene Glycol
ZnO	Zinc Oxide
CuO	Copper Oxide
RGB	RGB color model. R:Red, G:Green & B:Blue

CHAPTER 1

INTRODUCTION

1.1 Introduction

Energy storage has received wide attention in this last decades due to increasing awareness on various energy issues around the globe such as climate change, environmental pollution, rising over-consumption of fossil fuels, depletion of natural resources and development of renewable energy. Along with finding new alternative energy sources based on wind and solar and tidal, orchestrated efforts worldwide are also searching for a new approach that can offer a security of supply. Generated reneweable energy is usually stored in a system, machine or device that can be efficiently, economically and environmentally friendly and operated when needed. Lithium ion batteries, fuel cell and supercapacitors are at the frontier of the research effort for electrochemical energy storage devices (Liu et al., 2011).

Supercapacitor is defined as a device that can store electrical energy in the interface between an electrolyte and a solid electrode using two mechanisms. Charge storage mechanism using physical adsorption of ions, without any chemical reactions, are called electric double-layer capacitor (EDLC). Another mechanism is based on fast redox Faradaic reactions at the electrode-electrolyte interface or can be categorized as pseudocapacitor (Zhao et al., 2011). Both types are able to store large amounts of energy compared to conventional capacitors and are able to deliver more power than batteries. In addition, the mechanism of storing and releasing charge for the supercapacitor is reversable with good cycling ability compared to batteries. This desirable quality make them a lucrative option as energy storage devices as shown in various modern applications such as PDA, smartphones, laptops and hybrid electric vehicles (HEV). (Sharma and Bhatti, 2010)

By material types point of view, traditional materials for electrical double layer capacitors are include high specific area carbon and nanostructured low conductive substrates such as TiO_2(titania) nanoparticles network. Meanwhile transition conducting metal oxide such as RuO_2, Fe_3O_4, and MnO_2 along with conducting polymers such as polypyrrole, polyaniline and polythiopene are the typical materials used for pseudocapacitor devices (Choudhury et al., 2009)

1.2 Problem statement

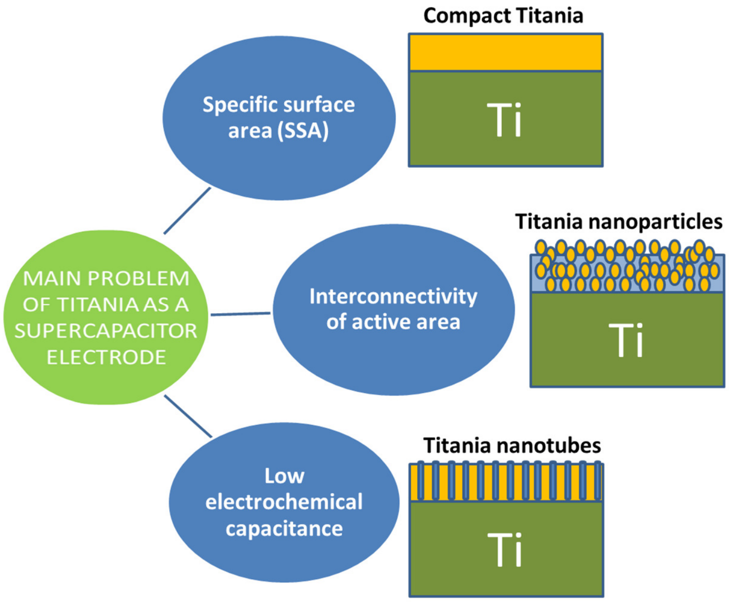

Figure 1.1 Three main problems of titania as a supercapacitor electrode

Recently, titania was used as electrode materials in energy storage and conversion devices such as dye-sensitized solar cells (Mor et al, 2006; Park et al., 2009), Li-ion battery (Kubiak et al., 2009; Chen and Lou., 2010) and supercapacitors (Mi et al, 2008; Salari et al., 2011) due to their semiconducting properties, electrochemical behavior and long term chemical stability. However, the publications related to titania materials as a supercapacitor electrode are relatively lower than other transition metal oxides due to three main issues as shown in Figure 1.1. In general, compact titania has a low specific surface and would only resemble conventional electrical double layer capacitors which contributes to non faradaic mechanism with very low specific capacitance of 10-40 $\mu F\ cm^{-2}$ in the charge-discharge process (Salari et al., 2011). This is due to the high electrical resistance of the titania oxide that result in low electrochemical capacitance.

Although titania nanoparticles based supercapacitor electrode in binder form can increase specific surface area of the electrode, the interconnectivity of active titania material in the binder can contribute to other issue. The resistance of the supercapacitor electrode based on titania nanoparticles in a binder form is expected to increase with increasing nanoparticle loading. Increased ohmic polarization and hence, reduced driving force (potential) for electron reactions can occur deep inside a thick film where the materials are less active as opposed to ones near the surface. Increasing titania nanoparticle loading also makes a thicker electrode in which ion transport becomes more difficult (Xie et al., 2011). In contrast, high binder amount is essential to retain a certain flexibility since too rigid electrodes would be mechanically unstable during electrode manufacturing (Bonnefoi et al., 1999).

To solve the problem of compact and nanoparticles titania as described previously, anodized titania nanotube was introduced as a binder-free supercapacitor electrode and the specific electrochemical capacitance of 900 μF cm^{-2} was obtained (Salari et al., 2011). The value is still smaller than 3.03 mF cm^{-2} obtained for titania-ruthenium nanotubes composite system (Xie and Fu, 2010). The latter has used titania nanotubes as a support to fabricate a composite electrode because the titania nanotubes on its own is still not electroactive for charge storage activities. As-grown titania nanotubes are amorphous and therefore are less conductive (Macak et al., 2007). Although the anodized titania nanotubes could be used as a binder-free supercapacitor electrodes, the conductivity of the nanotubes still need to be enhanced. This thesis will apply a few approach to enhance the charge storage activities and to increase specific electrochemical capacitance of the nanotubes using heat treatment or annealing, suitable electrolyte, engineering design approach and making a new composite.

1.3 Research objectives

The main objective of this research is to develop a binder-free supercapacitor electrode based on anodic titania nanotube array and to apply a few methods to enhance and increase its electrochemical capacitance performance. Using this nanotubes, binder-free electrodes can be realized in which titanium foil can be used as a current collector while their nanotubular titanium oxide is used as charge storing and releasing area. The details of the research objectives are highlighted as follows:

1. To synthesize titania nanotubes using anodization of Ti foil in ethylene glycol containing ammonium fluoride (NH_4F) electrolyte to studythe

effect of low vacuum annealing on surface morphology, crystal structure and chemical composition of titania nanotubes.

2. To investigate titania nanotube formation mechanism at its early growth stage using surface morphology analysis and to characterize it as a binder-free supercapacitor electrode. To study the effects of surface morphology on charge storage behavior in aqueous electrolyte such as sodium sulfate and to obtain specific electrochemical capacitance using cyclic voltammetry.

3. To synthesize and enhance electrochemical capacitance of titania nanotube using bamboo-type structure, to study the effect of oxygen and ammonia annealing conditions on crystal structure (eg. anatase, rutile), surface defect (e.g. oxygen vacancies and concentration of Ti^{4+} and Ti^{3+}) and charge storage characteristics in neutral (sodium sulfate) and redox (acid sulfuric) electrolytes.

4. To enhance electrochemical capacitance of titania nanotubes in sodium sulfate by optimization of anodization process using Box-Behnken design and response surface method (RSM). To investigate charge storage characteristic using galvanostatic charge-discharge testing.

5. To increase electrochemical capacitance and to broaden potential operation windows by using 1-ethyl-3-methyl imidazolium hydrogensulfate ionic liquid (EMIM hydrogensulfate) as electrolyte. To investigate charge storage mechanism of titania nanotubes in ionic liquid.

6. To investigate the effect of flat band potential on semiconducting properties and electrochemical capacitance of titania nanotubes using Mott-Schottky analysis and electrochemical impedance spectroscopy (EIS).

7. To functionalize anodized titania nanotubes with electroactive NiO to enhance charge storage performance for redox supercapacitor applications.

1.4 Scope of works

Anodization of titanium (Ti) will be done in organic electrolytes such ethylene glycol and glycerol. Tiny amounts of DI water will be added in each anodization. Water plays the key role for providing the oxygen source for tube growth, splits pores into tubes, and is responsible for sidewall ripple formation (Roy et al., 2011).

Process characterization of Ti anodization will not be experimentally covered in detail. Only important paramaters such as applied potential, flouride ion concentration and duration of anodization will be investigated. Electrochemical methods such as cyclic voltammetry, electrochemical impedance spectroscopy and Mott-Schottky analysis will be done in three electrode systems but galvanostatic charge-discharge testing will be done in a symmetrical two electrode set-up.

1.5 Structure of the thesis

Chapter 2 gives a detailed review of the supercapacitor technology, historical background, storage mechanisms, electrode materials and electrolytes and recent development related with titania as an electrode for energy and conversion devices especially in supercapacitor application. Literatures related with techniques to characterize electrochemical capacitance and charge storage behavior will be reviewed. Semiconductor electrochemistry such as energy band gap, flat band potential and interfacial properties also will be covered.

Chapter 3 describes experimental procedures of the seven projects to achieve previously defined objectives. In addition, analysis techniques such as FESEM, FEMTOSCAN, XRD, XPS, cyclic voltammetry, electrochemical impedance spectroscopy, galvanostatics charge-discharge testing and Mott-Schottky analysis will be elaborated in detail.

Chapter 4 presents results and discussion for each experimental procedures and will be organized in seven projects as follows:

(1) Synthesis and characterization of vacuum annealed anodized titania nanotubes
(2) An investigation on titania nanotubes formation and its application as a binder-free supercapacitor electrode
(3) Supercapacitance of nitrogen annealed bamboo-type titania nanotubes
(4) Enhancing electrochemical capacitance of anodized titania nanotubes

using Box-Behnken design and Response Surface Method (RSM)

(5) Enhancing electrochemical capacitance of anodized titania nanotubes
using EMIM Hydrogensulfate ionic liquid as electrolyte

(6) Influence of flat band potential on semiconducting properties of anodized
titania nanotubes in EMIM Hydrogensulfate ionic liquid

(7) Functionalization of titania nanotubes with nickel oxide particles for
redox type supercapacitor

Chapter 5 summarizes all conclusions and several recommendations for future work.

CHAPTER 2

LITERATURE REVIEW

2.1 Introduction

A supercapacitor which is sometimes also known as an electrochemical capacitor, is a device that stores electrical energy and built similarly to a battery (Figure 2.1) with two electrodes immersed in an electrolyte and a separator that separates the electrodes. The electrodes are made from high surface area, porous material that has pores of diameter in the nanometer (nm) range. Basically, the operation of supercapacitor is very similar to regular electrostatic capacitors. Definition for the capacitor voltage can be given as in the following:

$$C = \frac{Q}{V} \tag{2.1}$$

where Q represents the collective charge present in the interface of the electrode and electrolyte and C represents the charge capacitance stored in each volt (V). The major distinction between the supercapacitor and its electrostatic capacitor lies in the requirement of an electrolytic solution in order for the supercapacitor to operate. Besides that, a supercapacitor collects its charge at the double layer of the electrochemical, also known as the Helmholtz Layer (Conway et al., 1997; Conway and Pell, 2003; Kotz and Carlen, 2000). The double layer can be found at the interface of the electrode with the electrolyte and are composed of the electrode that is charged and the electrolytic ions. The following equation shows the capacitance of a supercapacitor:

$$C = \frac{k\varepsilon_0 A}{d} \tag{2.2}$$

where k is taken as dielectric constant, ε_0 as the free space permittivity, A as the summation of the electrode's structure surface area that is effective, and d is taken as the distance that separates the electrode surface and the ions, which is usually in the order of 5-10 Å (Kotz and Carlen, 2000). High capacitance is achieved through the employment of electrode materials that are porous and has a large potent inner surface area (Kotz and Carlen, 2000).

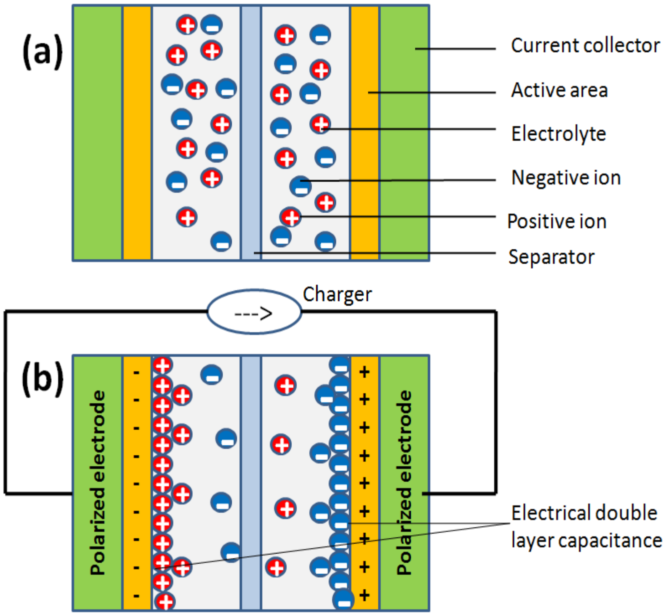

Figure 2.1 Schematic of supercapacitor definition (a) initial (b) charging

In the storage of energy of supercapacitor, chemical changes in the bulk electrode elements are not involved and the process is considered very efficient as it has minimal losses that are irreversible. Therefore, a supercapacitor has more density of volumetric power compared to a fuel cell and battery. Kotz and Carlen (2000), has projected power densities reaching up to 2 kW cm^{-3}.

However, since the bulk electrode element is not involved in the storage of charge, the energy densities of the supercapacitor are less than fuel cells and batteries. The supercapacitor can be fully charged or discharged in seconds; consequently, their energy density (about 5 Wh kg^{-1}) is lower than in batteries, but a much higher power delivery or uptake (10 kW kg^{-1}) can be achieved for shorter times (a few seconds). The supercapacitor also presents a much longer life cycle than batteries. They play an important role in complementing or replacing batteries in the energy storage field, for example, like uninterruptible power supplies (back-up supplies used to protect against power disruption) and load-levelling (Zhang et al., 2009). Comparison of the supercapacitor and battery are given in Table 2.1.

Table 2.1 Comparison between supercapacitor and battery (Zhang et al., 2009)

Characteristic	Supercapacitor	Battery
Charge Time	0.3–30 second	1-5 hour
Discharge Time	0.3–30 second	0.3–3 h
Life Cycle	>100,000	500–2000
Specific Energy (Wh/kg)	1–10	10–100
Specific power (W/kg)	1000	50–200
Cycle efficiency (%)	0.85–0.98	0.7–0.85

2.2 Storage Mechanism Based On Electrical Double Layer Principle

The ionic environment in the proximity of a charged surface can be envisioned using the double layer model. Understanding the electrical double layer structure is of great importance for the rational and optimum designing of the electrode morphology. Over the years, various models have been developed to explain the observations made by chemist. The double layer model for an electrode-electrolyte interface (Wang and Pilon, 2011; Armstrong and Horrocks, 1997; Xu and Riley, 2011) can be explained by the Hemholtz, Gouy-Chapman and Stern model below:

2.2.1 Helmholtz Model

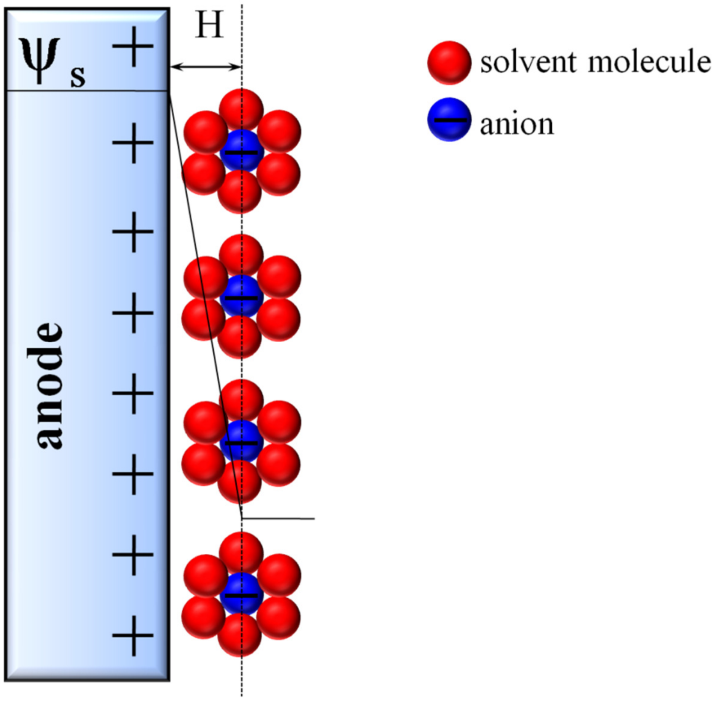

Figure 2.2 Helmholtz double layer model (Wang and Pilon, 2011)

Helmholtz was the first to introduce the concept of an electrical double layer. He realized that the charged electrode immersed in electrolyte solution is capable of storing electric charge by repelling co-ions while attracting counter ions to their surfaces. As shown in Figure 2.2, Helmholtz described this phenomenon using a model of the interphase in which all the excess charge on the metal is located at its positively charged surface, ψ_s and in the solution there is a rigidly held layer of opposite charged ions in a plane parallel to the surface of the electrode and separated by a distance, *H*. This structure is analogous to that of conventional dielectric capacitors with two planar electrodes separated by a distance. The surface charge potential is linearly used up from the surface to the counter ions fulfilling the charge. The Helmholtz theoretical treatment does not sufficiently illustrate all the features, since it hypothesizes rigid layers of opposite charges. This does not occur naturally.

2.2.2 Gouy-Chapman Model

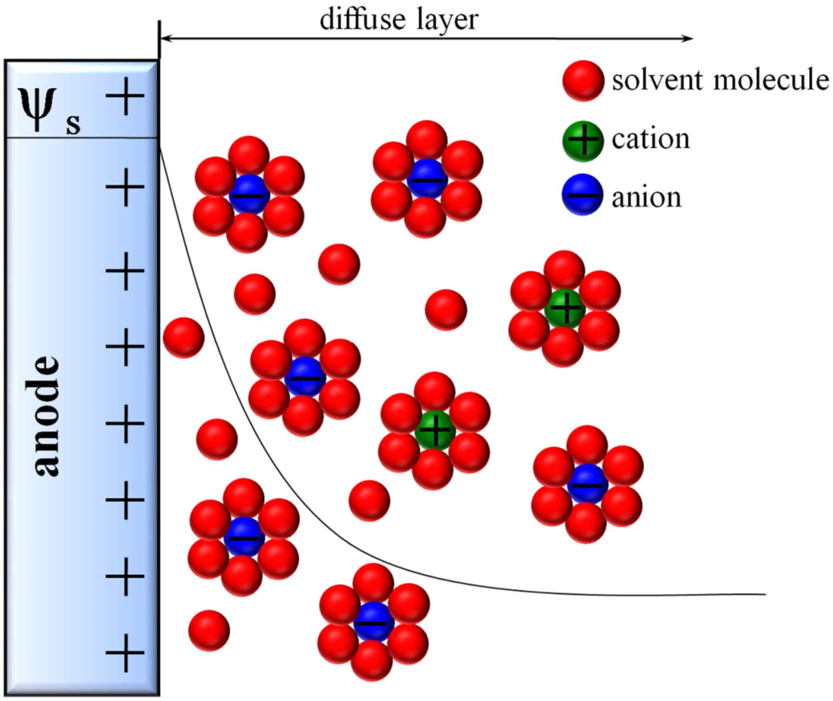

Figure 2.3 Gouy-Chapman model (Wang and Pilon, 2011)

In the early 1900, Gouy and Chapman proposed a diffuse double layer where the gathered ions, due to the Boltzmann distribution, spread to some distance from the solid surface. Gouy model accounts that the ions are mobile in the electrolyte solutions and are driven by the coupled influences of diffusion and electrostatic forces. To account for this behaviour, Gouy proposed that thermal motion kept the ions from aggregating on the surface of the electrode, instead forming a diffuse space charge as shown in Figure 2.3.

2.2.3 Gouy-Chapman-Stern Model

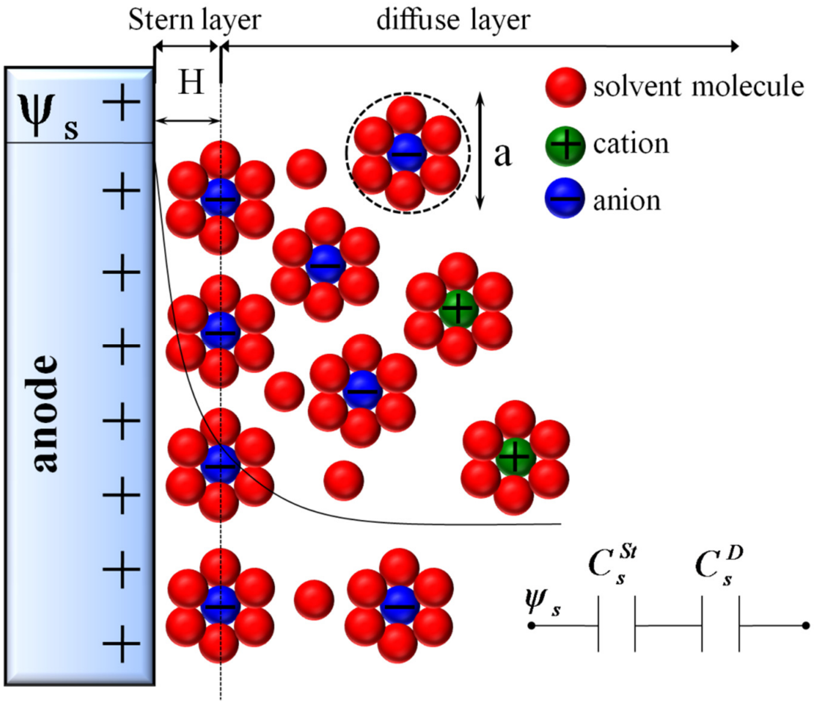

Figure 2.4 Gouy-Chapman-Stern model (Wang and Pilon, 2011)

The Helmholtz model and the Gouy-Chapman model were combined and described by Stern. According to him, the electric double layer consists of two layers (Figure 2.4), namely, (i) the Stern layer (or Helmholtz layer), which relates to the condensed layer of immobile ions strongly adsorbed to the surface of the electrode, and (ii) the diffuse layer where the ions are mobile. The Stern layer has no free charges within it. The electrical double layer capacitance consists of the Stern layer and the diffuse layer capacitances in series.

2.3 Nanostructured Metal Oxides Based Supercapacitor Electrodes

Metal oxide thin films will continue to play a major role in supercapacitor technology. Among the several transition metal oxides studied for capacitor response, the only oxide that has been widely researched and known for its superior electrochemical capacitor response to date is the various crystallographic and morphological forms of ruthenium oxide (Lokhande et al., 2011). Hydrous ruthenium oxides with amorphous structure have been reported to be promising electrode materials for pseudocapacitor applications due to their intrinsically excellent quasimetallic conductivity and high pseudocapacitance. However, the high cost of the compound has placed huge obstacles for its large scale manufacture (Patake et al., 2010). Therefore, a lot of effort has been devoted to develop alternative pseudocapacitor electrode materials such as nickel oxide (Kim et al., 2011, Lang et al., 2008, Jiang et al., 2011, Meher et al., 2011), cobalt oxide (Xia et al., 2011), copper oxide (Endut et al., 2013), zinc oxide (He et al., 2011) and manganese oxide (Jiang et al., 2009, Chang et al., 2009).

Various nanostructured metal oxides such as nanoflakes, nanowires, inverse opals, nanofibrous, nanorods and nanoparticles were synthesized to improve the electrochemical capacitance of the electrode. These nanostructures were synthesized using hydrothermal, co-precipitation, chemical bath deposition, electrodeposition and anodization. Hydrothermal synthesized ultrathin nanoflakes nickel hydroxide shows promising specific capacitance of 1715 F g^{-1} (Jiang et al., 2011). However, direct comparison of each nanostructures should be made carefully and other factors such as manufacturibility and reliability should be taken into account. The performance of nanostructured metal oxides based supercapacitor electrodes is summarized in Table 2.2.

Table 2.2 Performance of nanostructured metal oxides based supercapacitor electrodes

Material	Morphology	Synthesis Method	Electrolyte	Specific Capacitance (F g^{-1})	Ref.
MnO_2	Brush-like particles	Co-precipitation method	1 M Na_2SO_4	176	Jiang et al. 2009
RuO_2	Amorphous film	Electrodeposition	0.5 M H_2SO_4	1190	Patake et al. 2010
MnO_2	Ultrafine nanowire network	hydrothermal treatment	1 M KOH	279	Jiang et al. 2011
NiO	Shell inverse opals	electrodeposition	1 M KOH	96	Kim et al. 2011
NiO	Loose pack nanoflakes	chemical precipitation method	2 M KOH	942	Lang et al. 2008
CuO	Nanoflakes	Chemical bath deposition	1 M KOH	190	Endut et al. 2013
MnO_2	Powder particles	co-precipitation method	0.1 M Na_2SO_4	200	Toupin et al. 2002
MnO_2	Porous and nanofibrous	Anodization	0.1 M Na_2SO_4	332	Chang et al. 2009
ZnO	Nanorod	electrodeposition	0.1 M Na_2SO_4	675	He et al. 2011
$Ni(OH)_2$	Ultrathin nanoflakes	Hydrothermal method	1 M KOH	1715	Jiang et al. 2011
Co_3O_4	Nanowire arrays	hydrothermal	1 M KOH	599	Xia et al. 2011
NiO	Nanoparticle	hydrothermal method	2 M KOH	279	Meher et al. 2011

2.4 Titania Based Supercapacitor Electrodes

Among all transition metal oxides, titania is the most extensively studied material with more than 40,000 publication over the past 10 years, which makes titania to one of the most investigated compounds in materials science. Bulk titania is known to be a very useful non-toxic, environmentally friendly and corrosion-resistant material (Schmuki et al., 2011). However, it is quite suprising that publication for titania as a supercapacitor application is very limited. Not more than 10 papers are found available in journal publisher databases.

Titania has been investigated for use as a supercapacitor electrode material due to its semiconducting properties and chemical stability. In terms of charging mechanism, it has been mostly suggested that titania only contributes a very low non-faradic capacitance to almost no faradic capacitance. In general, titania capacitors would resemble conventional electric double layer capacitors, which act by a non-faradic mechanism with a very low specific capacitance of 10–40 μF cm^{-2} in the charge–discharge process (Salari et al., 2011; Xie et al., 2008; Conway and Pell, 2003).

It is widely believed that bare titania, with high electric resistance and low specific surface area, shows low electrochemical capacitance. However, it has been reported that decreasing the particle size of titania to less than 10 nm results in pseudocapacitive behaviour of the resultant material, allowing for an increase in the capacitance of anatase of up to 90–120 μF cm^{-2} (Wang et al, 2007; Salari et al, 2011). Application of high specific surface area titania materials for the supercapacitor electrodes have been investigated a few times such as nanocomplexes containing nanoribbons or nanowires (Xie and Fu, 2010), nanocrystalline titania powder (Salari et al., 2011), titania nanotubes (Salari et al., 2011), titania nanocomposites (Xie and Fu, 2010; Schmuki et al., 2011).

Titania nanocomplexes comprising disordered nanoribbon synthesized using anodization method in ethylene glycol solution with neutral ammonium fluoride and the controlled water content has a specific capacitance of 0.539 mF cm^{-2} (Xie and Fu, 2010). Titania nanoparticles with particle sizes <10 nm prepared by nonhydrolytic sol-gel route was drop cast onto plasma treated glassy carbon electrode. The electrode then calcined in air at 350 and 450°C. This electrode has a specific capacitance of 0.12 mF cm^{-2} (Wang et al., 2007). Titania nanoparticles in binder-form electrode also shows lower specific capacitance compared to binder-free electrode. For instance, nanocrystalline titania powder was synthesized via a sol–gel method employing two-stage hydrolysis of titanium (IV)-isopropoxide. The working electrode made of this nanocrystalline titania powder prepared by a conventional slurry method consisting of 70 wt.% of active material. This binder-form electrode has a specific capacitance of 0.181 mF cm^{-2} (Salari et al., 2011).

In addition, the anodized titania nanotubes has recently received wide interest due to comparatively higher specific electrochemical capacitance. This nanotube arrays which are grown directly on the conductive substrate have numerous benefits compared to binder-type electrodes. First of all, these nanostructured materials has an intrinsically high surface area that can ensure the high utilization of electrode materials with high specific capacitance. Secondly, a high charge/discharge rate can be obtained as the nanostructured materials can provide smooth and short superhighways to ions and electrons. Third, low contact resistance can be achieved as each nanotube is directly grown on the current collector, therefore, the need for binders or conducting additives that adds additional contact resistance and weight, can be disregarded in this case. Fourth, the tube structures also form surface electrical fields and decreases the recombination by restricting the injected electrons to the central zone of the tubes, as seen in dye-sensitized solar cell applications (Santiago et al., 2008; Xie et al., 2011).

Highly ordered titania nanotubes was synthesized using anodization of titanium foil in flouride containing organic electrolytes such as glycerol or ethylene glycol followed by two step annealing in argon at 580^{o}C for a few hours. The specific capacitance obtained for this nanotubes in 1 M KCl is 0.9 mF cm^{-2} (Salari et al., 2011). The hydrogenated titania nanotubes also shows an enhanced specific capacitance of 3.24 mF cm^{-2} in 0.5 M Na_2SO_4. This hydrogenated titania nanotubes was obtained by calcination of anodized titania nanotubes in hydrogen atmosphere in a range of temperatures between 300 to 600°C (Lu et al., 2012).

By making nanocomposite, enhanced specific capacitance could be obtained. For example, an electrochemical anodization of titanium metal is carried out to fabricate titania nanotube array and ruthenium oxide as a composite supercapacitor electrode. Both electroreduction and electrooxidation process are applied for electrodepositing ruthenium oxide on the titania nanotubes substrate. This method could achieved specific capacitance of 3.03 mF cm^{-2} in 1 M H_2SO_4 electrolyte (Xie and Fu, 2010). By incorporating nickel hydroxide into titania nanotubes by a one-cycle or multi-cycle alternate electrodeposition–oxidation followed by a thermal dehydration process, flower-like nickel oxide-titania composite was obtained. This composite electrode has a specific capacitance of 46.3 mF cm^{-2} (Xie et al., 2009). Table 2.3 is a summary of supercapacitor electrodes performance based on titania materials.

Table 2.3 Supercapacitor electrodes based on titania materials

Material	Morphology	Synthesis Method	Electrolyte	Operating Voltage (V)	Specific Capacitance (mF cm^{-2})	Ref
Titania	Highly ordered nanotubes	Anodization method	1 M KCl	-0.2 to 0.6	0.9	Salari et al., 2011
Titania	Nanocrystalline powder	sol–gel method	1 M KCl	-0.2 to 0.6	0.181	Salari et al., 2011
Titania	Nanocomplexes comprising disordered nanoribbon	Anodization method	1 M H_2SO_4	0.2 to 0.5	0.539	Xie and Fu, 2010
Hydroge-nated Titania	Highly ordered nanotubes	Anodization followed by calcination hydrogen atmosphere	0.5 M Na_2SO_4	0.0 to 0.8	3.24	Lu et al., 2012
Titania	Nanoparticle	sol-gel	1 M $LiClO_4$ in propylene carbonate	1.5 to 2.5	0.12	Wang et al., 2007
Titania-Rutheni-um Oxide	Nanotubes composite	anodization followed by electrodeposi-tion	1 M H_2SO_4	0.0 to 1.0	3.03	Xie and Fu, 2010
Nickel oxide-titania composite	Flower-like nickel oxide-titania composite	Anodization followed by electrodeposition	1 M NaOH	0.0 to 0.6	46.3	Xie et al., 2009

2.5 Anodized Titania Nanotubes

Titania nanotubes can be synthesized using a few methods such as the template-assisted method (Qiu et al., 2006; Qiu et al., 2007), sol-gel techniques (Deng et al., 2010; Zeng et al., 2007), solvothermal method (Santara and Giri, 2013; Chau et al., 2012), atomic layer deposition (Lee et al., 2010; Lee and Jho, 2011) and anodization (Macak and Schmuki, 2006; Paramasivam, 2008). These titanium precursor solution and processes based on templates can produce tubes individually or in disconnected clusters or bundles that are usually scattered in a solution. As a result of this, often an extensive distribution of tube length is acquired and usually the tubes on the surface of the electron are compressed into layers to employ the structures in an electrically contacted device. However, this process causes an inconsistent position of the nanotubes on the electrode that eradicates many benefits of the one-dimensional directionality.

On the other hand, the electrochemical anodization concept mentioned here is self-organizing: a multitude of oxide nanotubes aligned at right angles to the substrate surface (Figure 2.5) as well as a distinct (and amenable) tube length is obtained from it. The tubes are affixed to the surface of the metal and this will therefore connect the two electrically. Practically any form of titanium surfaces or other metal surfaces can be covered by a layer of nanotube that is densed and defined with the electrochemical anodization method and is therefore an extremely flexible parallel process of structuring (easy to scale up) (Shankar et al., 2009; Roy et al., 2010; Mor et al., 2006). For instance, rapid breakdown anodization (RBA) of TiNb, TiZr and TiTa alloys in chloride-perchlorate based solution for a short period of time could produce nanotube bundles on this alloy (Jha et al., 2010). Meanwhile, self-ordered arrays of titanium manganese mixed oxide nanotubes were produced by anodization of Ti-8Mn alloy under ultrasonication in diluted ethylene glycol containing fluoride (Mohapatra et al., 2007).

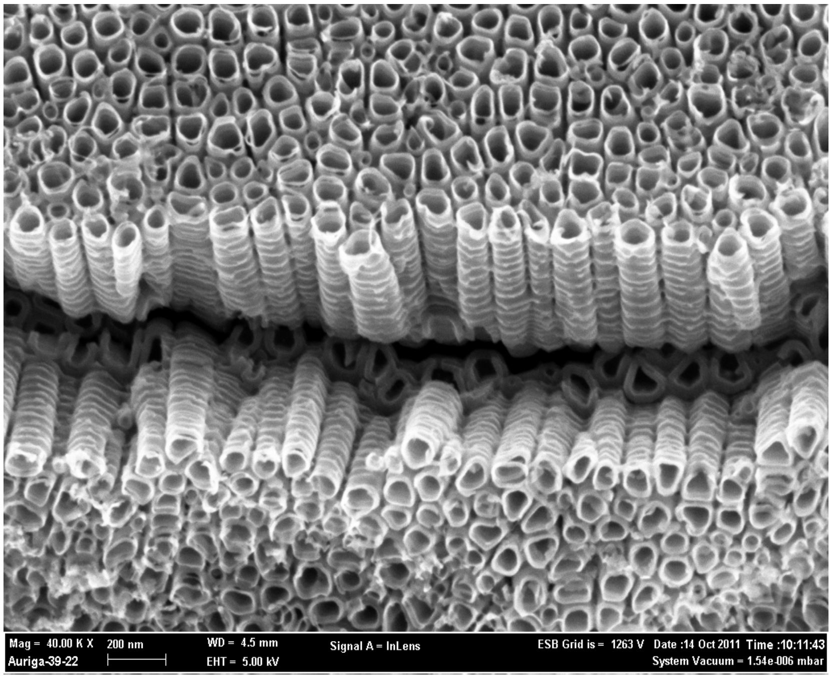

Figure 2.5 Highly-ordered anodic titania nanotubes obtained after anodization in flouride contained electrolyte

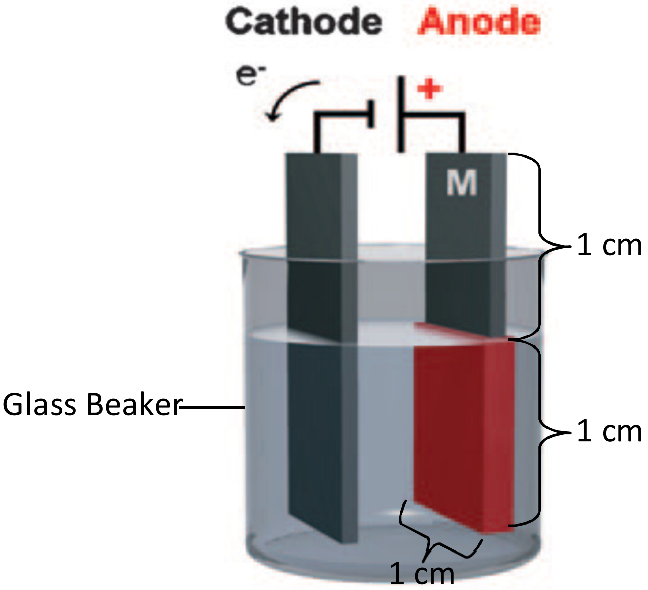

Figure 2.6 Electrochemical anodization set up

2.5.1 Synthesis

A self-ordering growth by anodic oxidation or anodization (Figure 2.6) has attracted wide interest in recent years. The approach resembles the classical approach of electrochemical anodization to form self-ordering porous alumina. For more than 50 years, anodization of aluminum metal sheets in an acidic environment will produce a porous oxide structure of several μm thickness. In 1995, Masuda and Fukuda showed that under an optimized anodic conditions, an oxide containing highly ordered pore arrays could be grown (Masuda and Fukuda, 1995). Zwilling grew the first self-ordered titania nanostructures by anodizing Ti in a fluoride-containing electrolyte (Zwilling et al., 1999). In this anodization setup, as shown in Figure 2.6, tube layer is commonly produced by the administration of a step potential (or ramp) with a consistent current. An aqueous or nonaqueous electrolyte containing roughly 0.05 M – 0.5 M (0.1–1 wt%) ions of fluoride (and most of the time some ion species will also be present in the background) will require a potential supply of 1–30 V for aqueous and 5–150 V for nonaqueous electrolyte. The current-time characteristics is recorded to show the growth of the oxide (Figure 2.7). From equations (2.3)-(2.6), it can be predicted that a compressed oxide layer forms on the titania surface in the absence of fluoride:

$$M \rightarrow M^{z+} + ze^- \qquad (2.3)$$

$$M + \frac{z}{2}H_2O \rightarrow MO_{z/2} + zH^+ + ze^- \qquad (2.4)$$

$$M^{z+} + zH_2O \rightarrow M(OH)_z + zH^+ \qquad (2.5)$$

$$M(OH)_z \rightarrow MO_{z/2} + \frac{z}{2}H_2 \qquad (2.6)$$

Simultaneously, the hydrogen evolution occurs at the cathode as a counter reaction [Equation (2.7)]:

$$zH_2O + ze^- \rightarrow \frac{z}{2}H_2 \uparrow + zOH^- \tag{2.7}$$

This is the standard anodization scheme that comprises of formation of ion [Ti^{4+}; Eq. (2.3)], reaction with O^{2-} [generated by (field aided) deprotonation of H_2O or OH^- Eq. (2.4) and (2.5)] and highfield ion transfer of Ti^{4+} and O^{2-} through the oxide.

Often, current-voltage curves are used to typify electrochemical reactions, such as anodization procedures (Figure 2.7, inset). These curves can be used to establish electrochemical process rates (such as ion-migration rates) and also to show the threshold voltages for formation of oxide. In the absence of fluorides, behavior that is typically active and passive are usually seen for oxide formation (Figure 2.7, inset). The anodization process is heavily affected by the existence of fluorides in the electrolyte, as they form water soluble $[TiF_6]^{2-}$ species. On one hand, Ti^{4+} ions are expelled at the oxide–electrolyte interface and complexation takes place [after migration through the oxide film; Equation (2.8)] however on the other hand, the titania formed undergoes chemical attack [Equation (2.9)]:

$$Ti^{4+} + 6F^- \rightarrow [TiF_6]^{2-} \tag{2.8}$$

$$TiO_2 + 6F^- \xrightarrow{H^+} [TiF_6]^{2-} + 2H_2O \tag{2.9}$$

Three various electrochemical traits can be obtained depending on the concentration of the fluoride (Figure 2.7, inset). When fluoride content is very low (≤

0.05 wt%), traits that occur in the fluoride-ion-free case will be seen, where upon anodization of the material to a current over U_p, forms a stable condensed layer of oxide or compact oxide (CO). When the concentration of fluoride is high (ca. 1 wt%), formation of oxide is not detected, as all the Ti^{4+} formed will react instantaneously with the copious amounts of fluoride for the formation of soluble $[TiF_6]^{2-}$. The reaction is then possibly managed by $[TiF_6]^{2-}$ diffusion from the surface, and the sample undergoes electropolishing (Beranek et al., 2003).

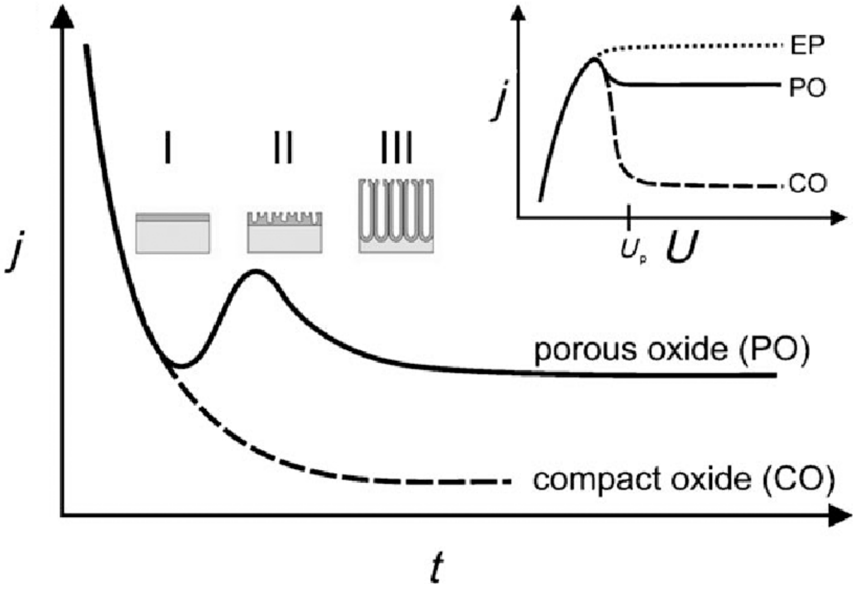

Figure 2.7 Conventional traits of current–time (j–t) after a voltage step in the absence (- - - -) and presence (———) of fluoride ions in the electrolyte. The inset shows normal linear sweep voltammograms (j–U curves) for different oxide morphology which are electropolished oxide (EP), porous oxide (PO) and compact oxide (CO) (Schmuki et al., 2011).

For intermediate concentrations of fluoride, formation of oxide will compete with Ti^{4+} solvatization and porous oxide (PO) or formation of nanotubes will be seen. Conditions that causes formation of nanotubes can be shown by a standard *j-t* curve as shown in Figure 2.7 (Schmuki et al., 2011). There are three stages shown by the curve: I) The early phase of anodization basically involves the curve following the fluoride-free instance, where a compact oxide layer will be present if samples are taken out from the electrolyte. In stage II, an increase in current takes place, and nanoscale pores that are irregular and permeate the initial condensed oxide are formed. This is due to the increase in reactive area leads to the increase in current. In the third stage, an ordinary nanopore or layer of nanotube forms and again the current will drop. At current densities that are steady, the growth of the tube continues upon the completion of self-organization (Mor et al., 2005; Mor et al., 2003; Bai et al., 2008; Sun et al., 2010; Taveira et al., 2005; Yasuda et al., 2007; Berger et al., 2009; Bhargava et al, 2009).

2.5.2 Properties

Titania is an *n*-type semiconductor that, depending on its crystal structure, has a band gap energy of 3.2 eV for anatase, 3.0 eV for rutile or 3.2–3.5 eV in its amorphous state. The material also has a high corrosion and photocorrosion resistance. Furthermore, it shows high biocompatibility, non-toxicity and has a comparably low price, thus, it is used in self-cleaning and anti-fogging glass, gas sensing and photocatalysis (Mi et al., 2008; Xiou et al., 2010; Liu et al., 2011). In 1D structures such as tubular geometries, the electronic properties are of great importance for many applications as they determine how efficiently electricity can be transferred (along the long path) from the oxide to the substrate. After the anodization process the titania tubes have an amorphous crystal structure with a band gap of 3.2 eV.

Thermal treatments above 300°C allow the amorphous material to convert into the anatase state, or a mixture of anatase and rutile. Some results indicate that for tubes formed under certain conditions—typically at comparably high voltages—some nanocrystallites may be present in the otherwise amorphous oxide (Mi et al., 2008;

Xiou et al., 2010; Liu et al., 2011; Beranek et al., 2005). Up until now, annealing treatments that lead to a complete conversion to the rutile state have not been successful, as the tubes tend to suffer from significant morphological deterioration (sintering and collapse) at around 700°C. Therefore, conversion of amorphous nanotubular structure to anatase is typically carried out by thermal annealing at temperatures between 300 and 500°C (Albu et al., 2008).

2.6 Types of Electrolytes

There are three kinds of electrolytes mostly used in the supercapacitor: aqueous, organic electrolyte and ionic liquid (Stoller et al., 2008). Aqueous electrolytes like acids (H_2SO_4), alkalis (KOH) and neutral salt (Na_2SO_4) have benefits such as high ionic conductivity (up till 1 S cm^{-1}) as well as low cost and wide acceptance. However, they also have the indispensable disadvantage of a relatively low decomposition voltage. The operating voltage is usually not able to go beyond 1.2 V to avoid decomposition of water as the thermodynamic stability of water is typically at 1.23 V and the nominal cell voltage of aqueous electrolyte cells is around 0.8 V. The small cell voltage restricts energy/power density of single cells and their applications (Kim et al., 2010; Lokhande et al., 2011). Propylene carbonate or acetonitrile are non-aqueous electrolyte mixtures that contain dissolved quaternary alkyl ammonium salts. They have been commonly used in commercial supercapacitors. Non-aqueous electrolytes has an electrical resistivity of at least an order of magnitude higher compared to that of aqueous electrolytes. This results in a high internal resistance for the resulting capacitors. The size of ions in an organic electrolyte is much larger than in an aqueous electrolyte (Sharma and Bhatti., 2010; Pandolfo and Hollenkamp., 2006).

In recent years, ionic liquids which have excellent properties such as in particular high-ionic conductivity and wide potential windows have been used as an electrolyte for the supercapacitor. Ionic liquid (IL) electrolytes comprising of thermally stable organic salts have excellent thermal stability, non-volatility, and non-flammability properties. Thus the IL electrolyte is expected to be good for high temperature and high-safety supercapacitor applications. For example, electrochemical behaviour of nanoporous titania in 1-ethyl-3-methylimidazolium bis(trifluoromethyl)sulfonyl amide (EMITFSI) had been studied (Francisco Fabregat-Santiago et al., 2006) and was found IL to be a suitable medium to replace any solvent used in titania-based devices, such as solar cells and supercapacitors. The ionic liquids such as 1-ethyl-3-methyl imidazolium (EMImþ), 1-butyl-3-methyl imidazolium (BMImþ) and 1-methyl-1-propyl pyrrolidinium (BMPyþ) cations, as well as tetrafluoroborate, hexafluorophosphate and bis((trifluoromethyl)sulfonyl) imide anions have also been tested in activated carbon powder based electrical double layer capacitor (Lewandowski and Galin´ski., 2004). Ionic liquid also can offer pseudocapacitive effect as found in butylmethylpyrrolidinium–dicyanamide (BMP–DCA) ionic liquid (IL) using MnO_2 electrode (Li et al., 2012).

However, storage mechanism of ionic liquid interface with solid electrode is suggested to be different from conventional electrical double layer capacitance as proposed by Gouy-Chapman-Stern model. Kornyshev et al, 2011 has proved systematically using experimental, theoretical and computational that the storage mechanism in ionic liquid can be elaborated by a mean-field theory for the clustering of ions with a definable size, and suggested bell or camel shapes of the differential capacitance versus voltage, decaying as $C=V^{-1/2}$. Wu et al, 2011 investigated the theoretical framework to further comprehend the capacitance of electrical double layers in nanopores and its mechanistic details into the origins of the observed scaling behavior.

2.7 Theory of Supercapacitor Testing Method

Investigation of supercapacitor electrode/electrolyte system can be made using cyclic voltammetry, galvanostatic charge-dischage testing and electrochemical impedance spectroscopy (EIS).

2.7.1 Cyclic Voltammetry

Cyclic voltammetry (CV) is a technique that is very substantial in the field of electrochemistry. CV measurement is taken at the electrode of which an electrical potential that differs periodically and linearly with time is applied. The resulting electric current is noted. The integration of the electric current with respect to time will give the total charge acquired at the electrode surface. Then, taking the total charge divided by the potential window will give the approximation of the capacitance.

Different scan rates are normally used in measuring capacitance to characterize the efficiency of energy storage devices like the electric double layer capacitors (EDLCs). At low scan rates, the capacitance measured is at a maximum and almost like the capacitance measured under equilibrium conditions.The shape of CV curves has widely been employed to estimate the electrochemical processes that involve the charging and discharging of titania based supercapacitor (Salari et al., 2011; Yang et al., 2011; Xie et al., 2008; Conway and Pell, 2003; Wang and Pilon, 2012).

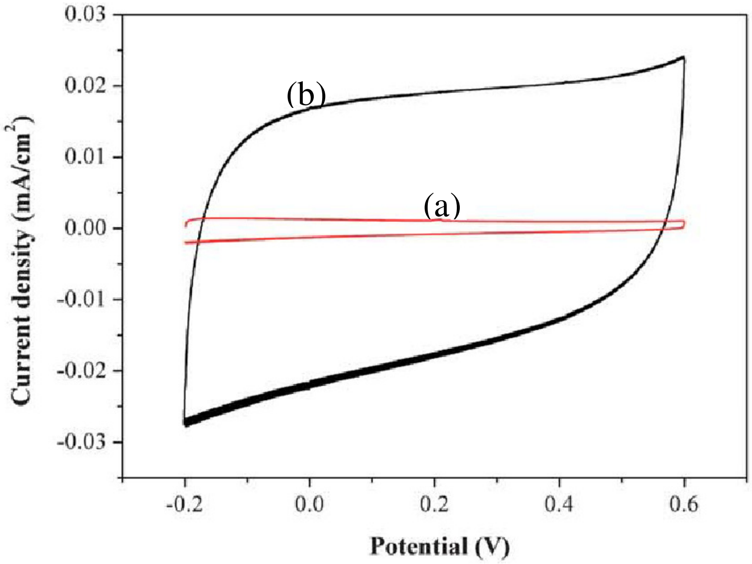

Figure 2.8 CV curve of argon annealed titania nanotubes in 1 M KCl electrolyte. (a) without argon gas, (b) with argon gas (Salari et al., 2011)

As shown in Figure 2.8, the CV of argon-annealed titania nanotubes material has a nearly symmetrical rectangular shape that indicates the charging process is based on electrical double layer capacitance (Salari et. al., 2011). By comparison of curve (a) for CV without argon annealed titania nanotubes and curve (b) with argon annealed titania nanotubes, the voltammetric charge or specific capacitance of curve (b) should be higher than curve (a). The specific capacitance (*C*) for both curves in the Figure 2.8 can be calculated using equation (2.10), where *I* is the average current (mA), *V* is the scan rate (mV s^{-1}) and *A* is the active area (1 cm^2).

$$C = I/V \ x \ A \tag{2.10}$$

$$C = \int_{e1}^{e2} i(E)dE/2(E_2 - E_1)v \tag{2.11}$$

Another method to calculate specific capacitance from the cyclic voltammogram is by using equation (2.11) where E_1 and E_2 are the cutoff potentials in cyclic voltammetry, i(E) is the instantaneous current, $\int_{e1}^{e2} i(E)dE$ is the total voltammetric charge obtained by integration of positive and negative sweep in cyclic voltammograms. $(E_2 - E_1)$ is the potential window width.

2.7.2 Galvanostatic Charge-discharge Testing

Chronopotentiometry (CP) or galvanostatic charge-discharge testing is the most basic constant current experiment used to investigate the suitablity of any materials for supercapacitor application. The technique as shown in Figure 2.9, refers to applying a constant current to an electrochemical system and recording the potential response as a function of time. It can also be used to investigate the cycleability of supercapacitor electrode-electrolyte system. In the constant-current chronopotentiometry,

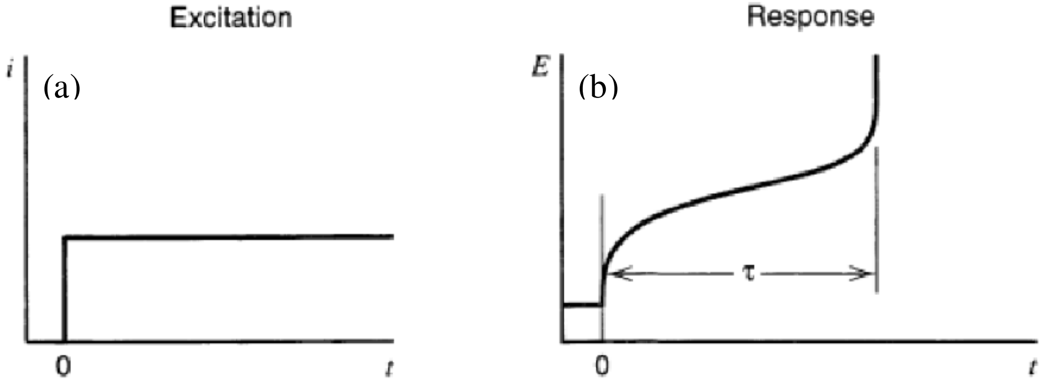

Figure 2.9 Constant current chronopotentiometry (a) excitation, (b) response

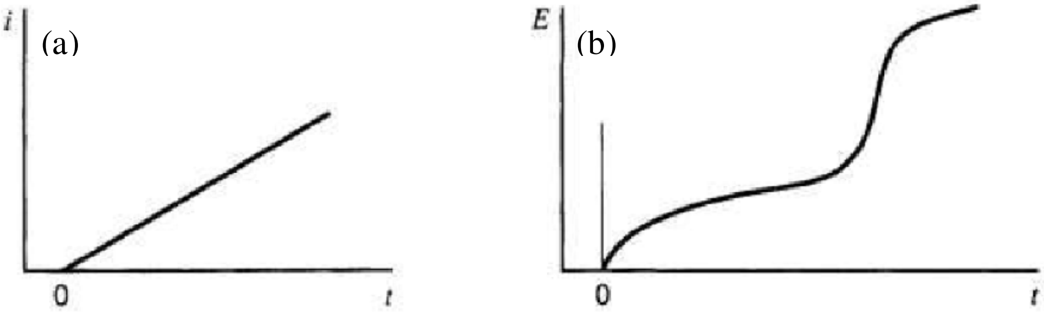

Figure 2.10 Chronopotentiometry with a linearly increasing current (a) excitation, (b) response

the constant current applied to the electrode causes its oxidation or reduction at a constant rate. The applied current can also be inverted after a time step or when a determined potential value is reached (current reversal chronopotentiometry) as shown in Figure 2.11(a) and 2.11(b). As an extension of this technique, the current can be continuously inverted obtaining a cyclic chronopotentiometry such as in Figure 2.11 (c) and Figure 2.11(d). By defining the potential cut-off point (anodic and cathodic) at which the current is inverted, the electrode behaviour can be studied in a defined potential range by avoiding side reactions, such as electrolyte decomposition.

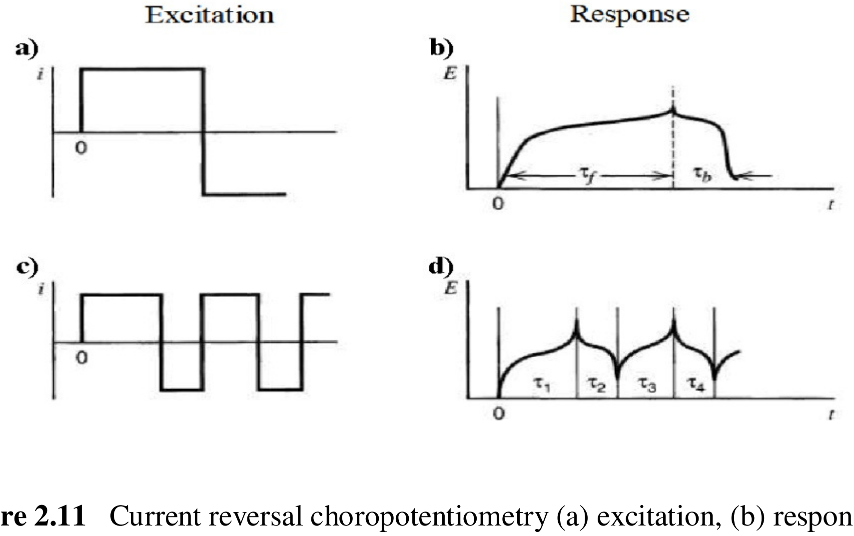

Figure 2.11 Current reversal choropotentiometry (a) excitation, (b) response and cyclic chronopotentiometry (c) excitation, (d) response

The discharge time during the response, τ_b (Δt) is used in specific capacitance of the electrode material tested. The specific capacitance can be calculated using the equation given below:

$$Z = \frac{I\Delta t}{A\Delta V} \tag{2.15}$$

where C (F cm^{-2}) is the specific capacitance, I (mA) is the discharge current, A (cm^2) is the nominal surface area, ΔV (V) and Δt (s) represent the potential drop during discharge and total discharge time respectively.

2.7.3 Electrochemical Impedance Spectroscopy (EIS)

Electrochemical Impedance Spectroscopy (EIS) is a technique used to evaluate the semiconducting properties of titania electrode surface (Schmickler, 1996; Orazem, 2008; Krause, 2007). This technique is based on applying a series of small voltage with different frequencies. In the EIS case, mostly the Bode and Nyquist plot is used to interpret the semiconducting properties of titania nanotubes. An equivalent electrical circuit can be simulated from EIS results in a porous electrode like titania nanotubes. The equivalent electrical circuit is called Randles circuit which includes a capacitor for the double layer interface capacitance, C_{dl} and resistor (R) for the polarization resistance (R_p).

Sinusoidal perturbations are the perturbations usually employed by an electrochemical system. For the purpose of simplification, only the sinusoidal perturbations of the voltage that has been employed will be studied.

$$V(t) = V_0 \, sin \, \omega t \tag{2.13}$$

where V (t) represents voltage at time t, V_0 is taken as voltage amplitude, and ω is taken as radial frequency (rad s^{-1}). The radial frequency and the frequency f (Hz) is related by ω = 2πf. At the same frequency, a sinusoid with a shift in phase will be the current response I(t).

$$I(t) = I_0 \, sin(\omega \, t + \Phi) \tag{2.14}$$

where I(t) represents current at time t, I_0 taken as current amplitude, and $\sin(\omega \, t + \Phi)$ as the phase shift where the voltage lags the current (Figure 2.12). Akin to the dc circuit law by Ohm, the ratio of voltage and current is the definition for impedance.

$$Z = \frac{V(t)}{I(t)} \tag{2.15}$$

The magnitude of the impedance is $Z_0 = V_0/I_0$ and the phase is Φ thus, it is a vector quantity. Presenting impedance in complex notations is therefore, more befitting (Figure 2.13).

$$Z = Z_0(cos\Phi + j \, sin \, \Phi) = Z' + jZ'' \tag{2.16}$$

where j =√(−1), Z' is taken as the part of the impedance that is real and Z" is taken as the the impedance imaginary part. Employing Euler's relationship, the equation can also be written as

$$Z = Z_0 e^{j\Phi} \tag{2.17}$$

The association of the two varying forms of presentation are shown by the complex diagram in Figure 2.13.

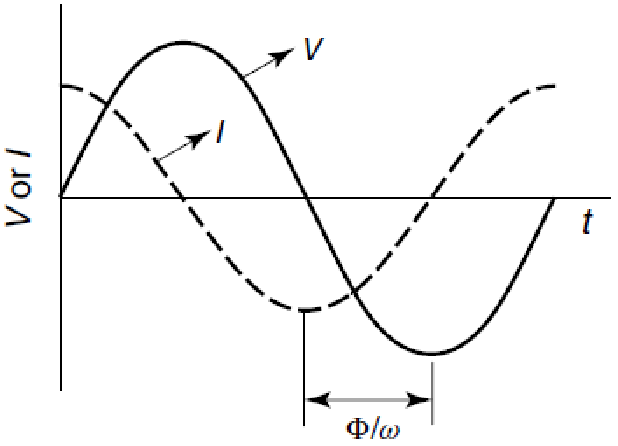

Figure 2.12 Sinusoidal voltage perturbation (V) and current response (I) (Krause, 2007)

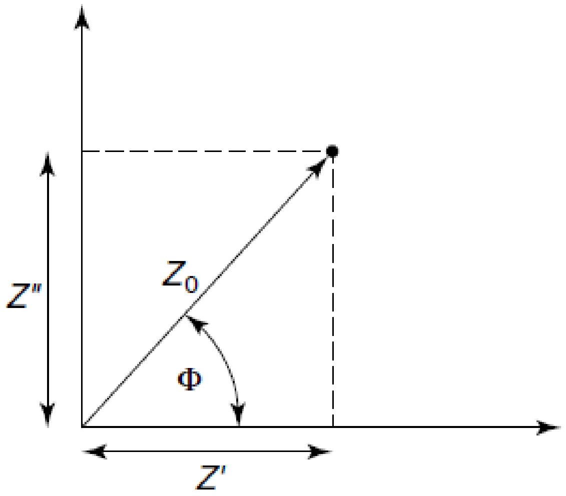

Figure 2.13 Impedance presentation in the complex plane. Z" and Z' represents the parts of the impedance that are imaginary and real, respectively. Z_0 represents the magnitude of the impedance, and Φ represents the phase angle (Krause, 2007)

Impedance is a vector quantity that can be connoted either in regards to the imaginary and real parts or in regards to the phase and magnitude. The two most accepted forms of data presentation can be acquired from these two forms of mathematical expressions. As explained above, the computation of the impedance parameters have proven very useful using the complex plane or Nyquist diagrams (Figure 2.14c), with plots of the parts of the impedance which is real versus the imaginary.

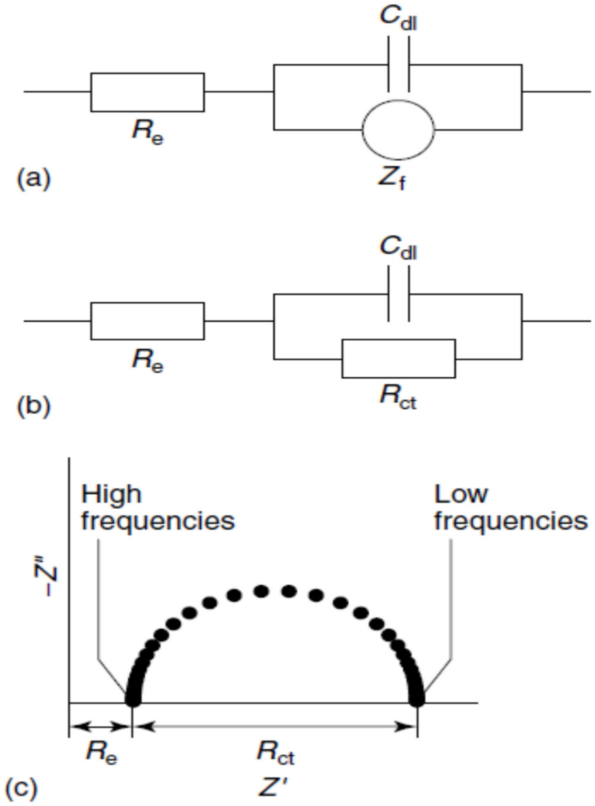

Figure 2.14 Equivalent circuits **(a)** general electrochemical cell; **(b)** simpleelectrochemical cell without diffusion; and **(c)** Nyquist plot for a simple electrochemical cell without diffusion (Krause, 2007).

The computation is taken from impedance spectra that is present as individual or numerous curves in the complex plane. However, since the impedance was measured at a frequency that was not indicated, the information they present is deficient. The presentation of experimental data has labels of the frequencies corresponded by each point in the Nyquist plot. The Bode plot can be used as an alternative for data presentation. Generally, it plots the phase angle and the logarithm of the impedance magnitude versus the logarithm of the frequency (Figure 2.15).

In the representation of log Z_0 versus log f, a horizontal line is seen when behavior of resistance dictates the behavior of the impedance. In contrast, a linear with a slope of –1 is seen when a capacitance determines the response of the impedance (Figure 2.15a). Occasionally, alternative Bode plots with correlations of log Z_o and log Z' versus log f are presented (Figure 2.15b). The two types of Bode plots has all the data given by the measurements of ac-impedance, which is a contrast to the Nyquist plots (Schmickler, 1996; Krause, 2007).

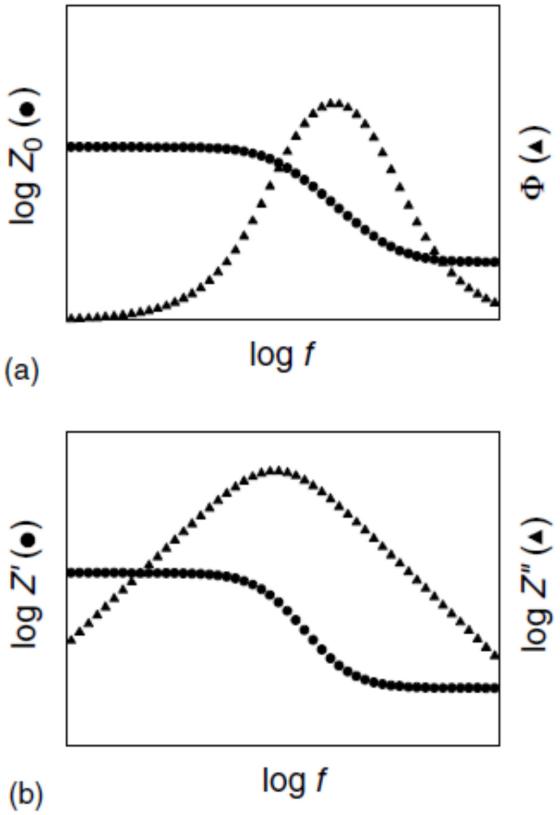

Figure 2.15 Bode plots for the equivalentcircuit shown in **Figure 2.14(b)**

2.8 Porous Electrode

Many authors has verified the fact that without the presence of faradaic processes, the impedance for solid electrodes does not comply to pure capacitive behavior. Surface coarseness or porosity is most often the cause of the deviation from ideality. The impedance behavior of rough electrodes is usually predicted using a constant phase element (CPE) with $0.5 < \alpha < 1$. A number of trials to determine the association of the CPE and the fractal surface morphology has been done. The initial transmission line model was first produced by De Levie to explain the dispersion of frequency in electrodes that are porous (Krause, 2007). This discussion emphasize on the double-layer charging effect without a faradaic procedure. Cylindrical pores of consistent diameter and near infinite length, without interconnections and filled homogeneously with electrolytes, is the basis of the model produced by De Levie. The material of the electrode is presumed to have no resistance. In conditions such as this, a pore reacts very much like a consistent RC transmission line that is depicted as shown in Figure 2.16.

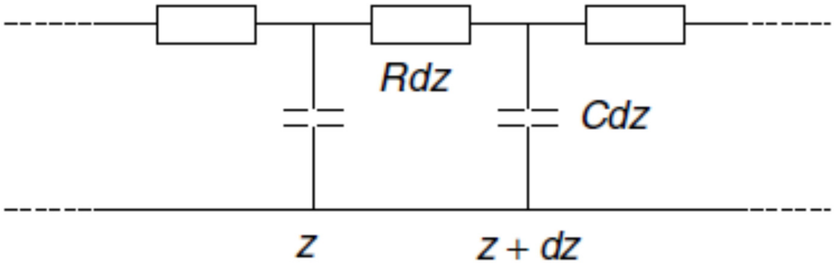

Figure 2.16 Section of the equivalent circuit of a pore, where z represents the distance from the pore entrance. Solution resistance and double-layer capacitance are evenly distributed (Krause, 2007).

When an excitation that is sinusoidal is used and the distance from the pore opening increases, the distance from the pore opening will be decreased by the amplitude of the signal which is caused by the behavior of the transmission line. This means only a small part of the pore is efficiently participating in the process of double-layer charging. From this, a saturation depth, λ of the signal, that is inversely proportionate to the square root of the frequency and directly proportionate to the square root of the pore can be determined,

$$\lambda = \frac{1}{2}\sqrt{\frac{kr}{C_{dl}\omega}} \tag{2.18}$$

where r represents the pore radius, κ is taken as the conductivity of the electrolyte, and C_{dl} is taken as the capacitance of the double layer. The depth of saturation is negligible at very high frequencies, therefore, only the flat external electrode surface capacitance effects are computed. The saturation depth and the pore influence become increasingly valuable at lower frequencies as the surface inside the electrode is enormous in comparison to the outer surface. Hence, a frequency decrease corresponds to a capacitance increase that results in a −45 phase angled linear in the complex plane diagram which equals to a Warburg impedance or a CPE with α = 0.5. At an adequately low frequency, the depth of saturation of the model will ultimately approach the extent of the pore length if it is expanded to pores with exact and even length.

A classic capacitive behavior will be observed with a decrease of the frequency as the surface of the electrode involved in the process of double-layer charging is now not dependent on the frequency (Figure 2.17, curve b). At high frequencies, the results obtained experimentally, matches the assumptions of De Levie’s model. However, at frequencies that are low, ideal capacitive behavior deviations are seen (Figure 2.17, curve c). This indicates that the nonideal behavior could be a result of the distribution of pore size. As each pore possesses a varied depth of saturation that is dependent on their dimensions,, therefore even at a single frequency, it leads to the depth of saturation distribution.

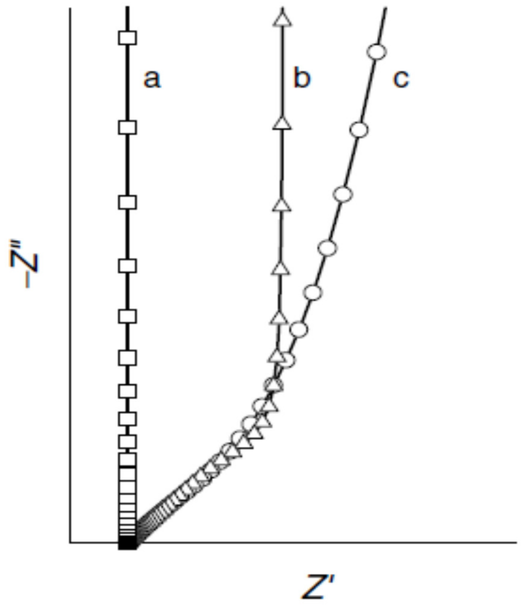

Figure 2.17 Impedance behavior of an electrode in the absence ofelectroactive species for **(a)** a perfectly flat electrode; **(b)** aporous electrode with evenly sized pores as in DeLevie's model; and **(c)** an electrode with a pore size distribution (Schmickler, 1996; Krause, 2007).

A model that integrates dispersion from the distribution of the pore size and in-the-pore dispersion that fits the description by De Levie is described (Schmickler, 1996). It gives an accurate description of the details for an electrode that is porous, obtained from the branch of the impedance that is of low-frequency. The average pore radius, the distribution width of the pore size, the mean length of the pore and the surface area can also be gauged using this model (Barcia et al., 2002; Barghava et al., 2009; Bisquert et al., 2000; Santiago et al., 2006; Levie, 1964; Munoz, 2007; Munoz et al., 2007; Krause, 2007)

2.9 Flat-band Potential

A perfect semiconductor would have delocalized electronic states like that in metals, and there are permissible electronic energy bands. According to Fermi level theorem, bands that are either completely filled or completely empty do not contribute to the conductivity. The difference between metals and semiconductors is that the bands carrying the current does not lap over and the band gap, where the level of Fermi lies, separates them as shown in an intrinsic semiconductor band structure (Figure 2.18). The valence band is the one below the Fermi level that is completely filled at T = 0 and the band of conduction is the one that lies above and is devoid at T = 0. The band of conduction contains low concentrations of electron and the band of valence contains holes of equal concentrations at higher temperatures. Lower energy bands such as shown above, are always completely filled.

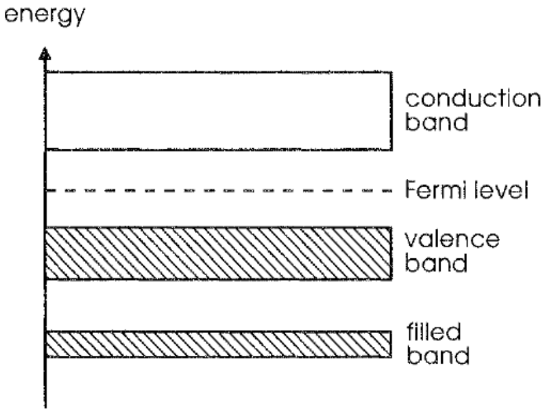

Figure 2.18 An intrinsic semiconductor band structure (Schmickler, 1996)

The Fermi level reaches the band gap center in a genuine or basic semiconductor. From the valence band, a few electrons are dispersed into the conduction band at room temperature and results in electron vacancies or holes. The electrons from the conduction band and the holes from the valence band are responsible for carrying the electric current. Fermi statistics is used to predict the conduction electron concentrations, N_c and p_v of the holes. E_c denotes the lower boundary of the band of conduction, and N_c, the density of states that are effective at E_c. The electron concentration is:

$$n_c = N_c f\left(E_c - E_f\right) \approx N_c \exp\left(-\frac{E_c - E_f}{kT}\right) \tag{2.19}$$

The above estimation is conclusive if E_C — E_F>> kT (that is if the band boundary is somewhat a few kT over the Fermi level), and also if the distribution of Fermi-Dirac f(e) can be substituted by the dispersion of Boltzmann. Therefore, the valence band has hole concentrations that can be calculated as follows:

$$p_v = N_v[1 - f(E_v - E_F)] \approx N_v \exp\left(-\frac{E_F - E_v}{kT}\right) \tag{2.20}$$

where E_v represents the uppermost boundary of the valence band and N_v represents the density of states that are effective at E_v. The estimation is conclusive if E_f — E_v>> kT. A degenerate semiconductor is indication when the Fermi level lies in the interior of a band, or near (namely, within kT) to a band boundary.

Typically, the band gap E_g of titania is valued at 3.2 – 3.5 eV and consequently the conductivity of this intrinsic semiconductor is small. The controlled introduction of suitable impurities, also known as doping, can increase the conductivity considerably. Dopants are of two kinds: donors and acceptors. Donors come with electronic states that are localized with energies right under the conduction band and their electrons can be donated to the conduction band; in accordance to Eq. (2.20). This causes the Fermi level to approach the lower boundary of the conduction band (see Figure 2.19a). The n-type semiconductors are those with an excess of donors and in this case, the electrons are considered as the majority carriers whereas the minority carriers are the holes. However, acceptors have devoid states right on top of the valence band, that accepts electrons from the valence band, thus inducing holes. Consequently, the Fermi level is displaced towards the valence band (see Figure 2.19b) in the case of a p-type semiconductor, and the majority carriers are the holes while the minority carriers are the electrons.

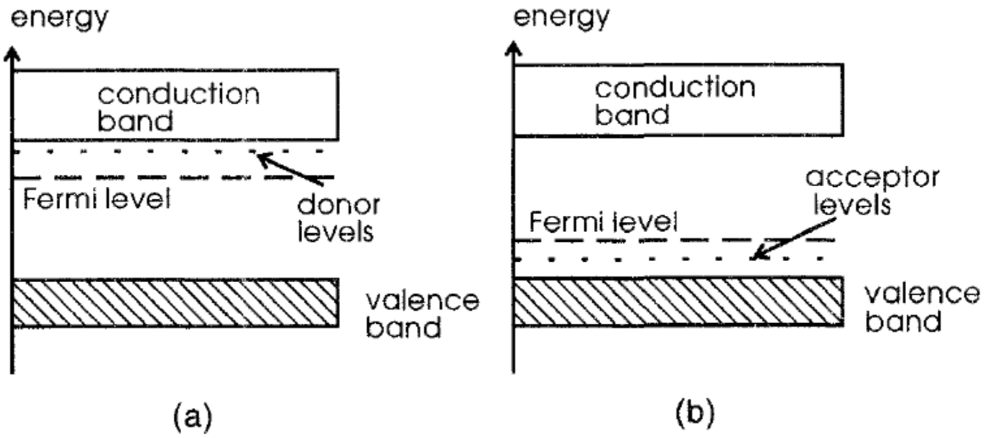

Figure 2.19 Band structure of (a) an n-type and (b) a p-type semiconductor (Schmickler, 1996).

A potential difference is created at the interface when a semiconducting electrode comes in contact with an electrolyte solution. Doped semiconductors usually have conductivity that is lower than the conductivity of an electrolyte solution; so basically most of the potential drop takes place in the boundary layer of the electrode while only a minute amount in the solution side of the interface (see Figure 2.20). This is a case that is opposite on metal electrodes, but akin to that at the interface between a semiconductor and a metal.

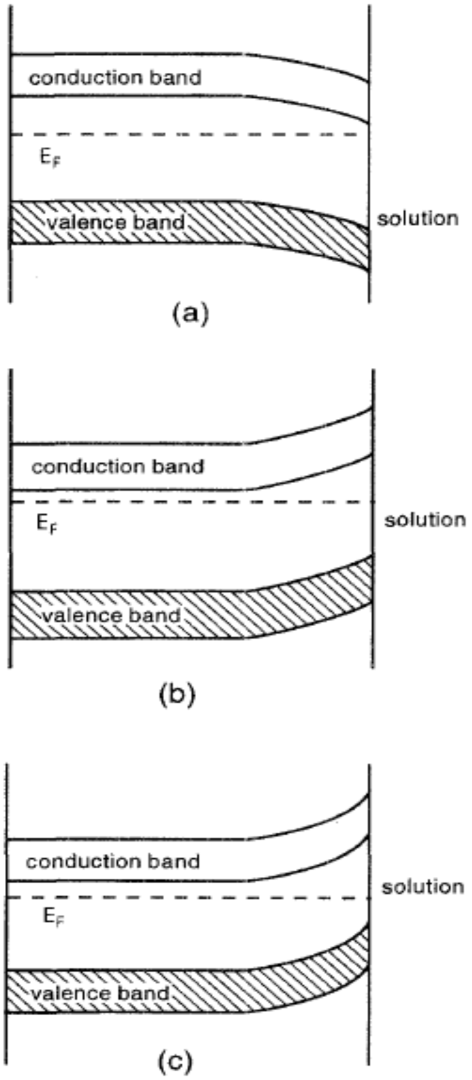

Figure 2.20 Band bending at the interface between a semiconductor and an electrolyte solution; (a)-(c) n-type semiconductor: (a) enrichment layer, (b) depletion layer, (c) inversion layer (Schmickler, 1996)

The bending of the bands is the distinction of the electrostatic potential in the surface region. The flat-band potential is a special potential where the electrostatic potential is constant. This potential is equivalent to a zero charge potential. Figure 2.20 showsband bending at the interface between a semiconductor and an electrolyte solution for n-type semiconductor.

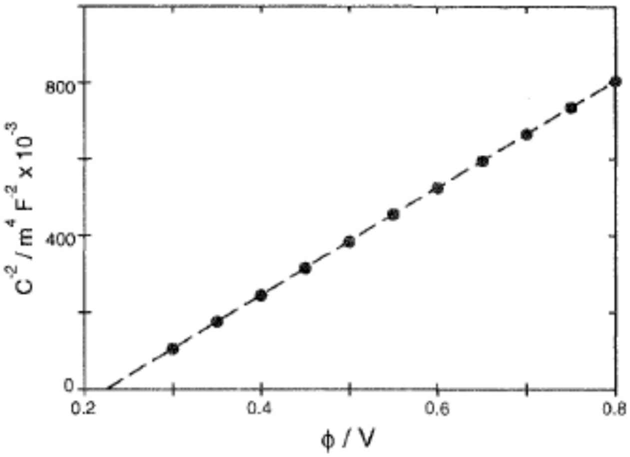

Figure 2.21 Mott-Schottky plot for the depletion layer of an n-type semiconductor; the flat-band potential E_{fb} is at 0.2 V. The data extrapolate to $E_{fb} + kT/e_0$ (Schmickler, 1996)

A common tool used for the specification of the semiconductor/electrolyte interface is the Mott-Schottky equation, which is valid in the depletion zone of the semiconductor. Thus, the determination of the flat band potential U_{fb} and the donor concentration N_D in a specific electrochemical system can be done by plotting C^{-2}_{sc} versus U (Figure 2.21) following the equation below:

$$C_{sc}^{-2} = \left(\frac{2}{\varepsilon\varepsilon_0 e N_D}\right)\left(U - U_{fb} - \frac{kT}{e}\right) \tag{2.21}$$

where C^{-2}_{sc} is taken as the space charge layer's differential capacitance. Indirect tunneling of electrons through the semiconductor layer usually occurs due to the high concentrations of numerous donor levels in the band gap. This ultimately results in a variation of the slope of Eq. (2.21) with frequency. The dependence on frequency is influenced by the distribution of relaxation times for the electron emanation, which in turn depends on the position of the states relative to the conduction band. The response of a large fraction of the frequency dependent donors is expected at sufficiently low frequencies (Munoz et al., 2007; Munoz, 2007; Krause, 2007; Bisquert, 2007, Santiago et al., 2003)

2.10 Response Surface Method (RSM)

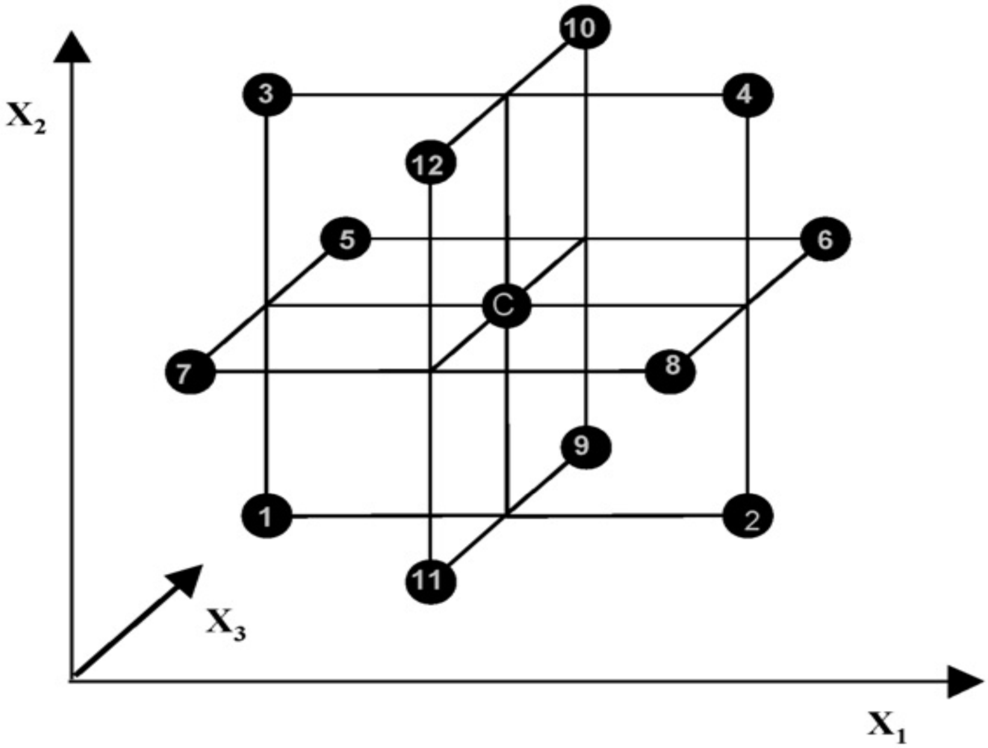

Figure 2.22 Box-Behnken design

Box–Behnken design is a spherical, revolving response surface methodology (RSM) design that consists of a central point and the middle points of the edges of the cube outlined on the sphere as shown in Figure 2.22. It consists of points lying on the surface of a sphere surrounding the center of the design. There are no points at the pinnacle of the cubic region created by the upper and lower limits for each factor in the Box-Behnken design. This is useful when the points on the edges of the cube represent factor level combinations that are prohibitively costly or impossible to test due to physical process limitations. These designs are rotatable (or near rotatable) and require at least 3 levels for each factor. The modeling and analysis of problems uses these designs where several variables influence the response of interest, with the objective being to optimize this response. Box-Behnken is a good design for response surface methodology because it allows: (i) estimation of the parameters of the quadratic model; (ii) building of sequential designs; (iii) detection of lack of fit of the model; and (iv) use of blocks (Li et al., 2010; Mourabet et al., 2012; Liu et al., 2011; Ferreira et al., 2007).

CHAPTER 3

RESEARCH METHODOLOGY

3.1 Introduction

This chapter describes and explains the materials, methods, experimental procedures and instrumentations used in this study which contains three main parts: electrode preparation, electrode characterization and electrochemical analysis. They will be organized based on seven projects. Titania nanotubes array synthesized using anodization method will be applied as the binder-free supercapacitor electrode. The electrode will be characterized by various instruments and analyses in order to study and investigate the performance of synthesized materials as a supercapacitor electrode.

3.2 Experimental Procedures

3.2.1 The First Project : Synthesis and Characterization of Vacuum Annealed Anodized Titania Nanotubes

3.2.1.1 Electrode preparation

Titanium foils (0.125 mm thick) were sonicated and degreased in acetone, ethanol and de-ionised (DI) water for 10 minutes each to remove surface impurities and contaminants. Electrochemical anodization was done in a two electrode cell using applied potential at 20 V to 50 V in an electrolyte containing ethylene glycol and DI water with the ratio 98:2 and ammonium fluoride, NH_4F (0.2 wt % to 0.5 wt %) at room temperature. Ti foil was used as the anode and stainless steel as the cathode (Figure 2.6). After anodization, the titania nanotubes electrode were rinsed with DI water and annealed in low vacuum furnace for 3 hours at 300°C to 600°C.

3.2.1.2 Electrode Characterization

The effect of vacuum annealing, applied potential and NH_4F concentration on anodized surface structure, composition and morphology were studied using the following equipments. Scanning electron micrographs and elemental analysis were taken using a Zess Auriga 40 Field Effect Scanning Electron Microscopy (FESEM) coupled with Energy Disperse X-Ray (EDX) using an operating voltage of 5 kV. The X-ray photoelectron spectroscopy (XPS) analysis of titania nanotubes was performed using an XPS Axis Ultra from Kratos equipped with monochromatic Al Kα radiation (BE = 1486.6 eV). The sample was analyzed inside an analysis chamber pressure of approximately 1×10^{-10} Pa. To correct the possible deviation caused by electrical charging of the samples, the C 1s peak of carbon at 284.5 eV was taken as an internal standard or reference. The phase detection of titania nanotubes was determined by x-ray diffraction (XRD) Siemens D5000, with a Cu-Kα radiation source mounted on a horizontal θ–2θ goniometer.

3.2.2 The Second Project: An Investigation on Titania Nanotubes Formation and its Application as a Binder-Free Supercapacitor Electrode

3.2.2.1 Electrode Preparation

Titanium foils (0.125 mm thick) were sonicated and degreased in acetone, ethanol and de-ionised (DI) water for 10 minutes each to remove surface impurities and contaminations. Electrochemical anodization was done in a two electrode cell using optimized process parameter at 45 V applied potential in an electrolyte containing ethylene glycol and DI water with the ratio 98:2 and NH_4F (0.5 wt %) at room temperature. Ti foil was used as the anode and stainless steel as the cathode. After anodization, the titania nanotube electrode were rinsed with DI water and annealed in oxygen gas for 3 hours at 500^oC.

3.2.2.2 Electrode Characterization

The mechanism of titania nanotube formation at the early growth stage was investigated using field emission scanning electron microscopy FESEM (Jeol JSM-840A) with an operating voltage of 5 kV. A specialized software package, FEMTOSCAN online (Advanced Technologies Center, Moscow) was also used for image processing and analysis of nanoscale morphology of anodized titania surface.

3.2.2.3 Electrochemical Analysis

The effect of titania surface morphology on charge storage behavior in sodium sulphate electrolyte was investigated using cyclic voltammetry (CV). The CV was carried out using a Potentiostat/Galvanostat Model PGSTAT-302N from Autolab, controlled by a USB_IF030 interface card and GPES/FRA software installed in a computer. A three electrode electrochemical cell with Ag/AgCl as the reference electrode and a Pt wire as the counter electrode was used in all experiments. The electrochemical experiments were done at room temperature in 1 M Na_2SO_4. The as-prepared titania nanotube film was used as binder-free working electrode with 1 cm^2 nominal surface area.

3.2.3 The Third Project: Supercapacitance of Nitrogen Annealed Bamboo-Type Titania Nanotubes

3.2.3.1 Electrode Preparation

Pieces of titanium foil (0.125 mm thick) were sonicated and degreased in acetone, ethanol and water (DI) for 10 minutes each to remove surface impurities and contamination. Electrochemical anodization was performed in a two electrode cell at 20 V in an electrolyte containing glycerol and DI water in a ratio of 75:25 and NH_4F (0.5 wt. %) at room temperature. Ti foil was used as the anode, and platinum wire was used as the cathode. The anodization time was 1 hour for sample A and 5 hours for sample B. Both samples were annealed at 500°C for 3 hours in an O_2 atmosphere with heating and cooling rates of 10°C min^{-1}. Sample C was prepared with a 5 hour anodization and was annealed at 500°C for 3 hours in an NH_3 atmosphere. NH_3 atmosphere was achieved by annealing titania nanotubes in closed autoclave tube vessel containing concentrated NH_3 (Kun Lai et al., 2010).

3.2.3.2 Electrode Characterization

Scanning electron micrographs was taken with a Zeiss Auriga 40 FESEM with an operating voltage of 5 kV. The phase determination of titania nanotubes was determined by X-ray diffraction (XRD) Siemens D5000, with a Cu-Kα radiation source mounted on a horizontal θ–2θ goniometer. The X-ray photoelectron spectroscopy (XPS) analysis of titania nanotubes was performed using an XPS Axis Ultra from Kratos equipped with monochromatic Al Kα radiation (BE = 1486.6 eV). The sample was analyzed inside an analysis chamber pressure of approximately 1 x 10^{-10} Pa. To correct the possible deviation caused by electrical charging of the samples, the C 1s peak of carbon at 284.5 eV was taken as an internal standard or reference.

3.2.3.3 Electrochemical Analysis

Cyclic voltammetry (CV), electrochemical impedance spectroscopy (EIS) and galvanostatic charge-discharge testing (CD) were carried out using a Potentiostat/Galvanostat Model PGSTAT-302N from Autolab, controlled by a USB_IF030 interface card and GPES software installed on a computer. A three-electrode electrochemical cell with Ag/AgCl as the reference electrode and a Pt wire as the counter-electrode was used in the CV experiments with scan rates from 5 mV s^{-1} to 100 mV s^{-1} between 0 V and 0.6 V. EIS measurements were performed between 100 kHz and 1 Hz under a constant potential of 0 V using a 5mV rms sinusoidal modulation. CD testing was done using the same applied potential as CV and a current density of 10 µA. The electrochemical experiments were performed at room temperature. The as-prepared titania nanotube film was used as a binder-free working electrode with a 1 cm^2nominal surface area. The electrochemical measurements of sample A and sample B were performed in 1 M Na_2SO_4, while sample C was measured in 1 M H_2SO_4.

3.2.4 The Fourth Project: Enhancing Electrochemical Capacitance of Anodized Titania Nanotubes Using Box-Behnken Design and Response Surface Method (RSM)

3.2.4.1 Electrode Preparation

Titania nanotube arrays were grown by electrochemical anodization of titanium foils (0.125 mm thick, 99.5% purity). Prior to anodization, the titanium foils were ultrasonically cleaned consecutively in acetone and ethanol for 15 minutes and rinsed with water (DI). The foils were anodized using a two-electrode configuration connected to a DC power supply, with graphite used as the counter electrode. The distance between two electrodes was fixed at 2 cm for all experiments. The electrolyte is a mixture of ethylene glycol, DI water (2 vol.%) and ammonium fluoride (0.3 to 0.5 wt. %). Titanium foil was anodized using a potential of between 30 V to 50 V for about 40 to 120 minutes. After anodization, the samples were rinsed with DI water and annealed in a muffle furnace for 3 hours at 500^{o}C, operated at atmospheric pressure.

3.2.4.2 Electrode Characterization and Electrochemical Analysis

Scanning electron micrographs were taken using a Zeiss Auriga 40 FESEM with an operating voltage of 5 kV. Charge-discharge measurements (CD) were conducted using a Potentiostat/Galvanostat model PGSTAT-302N from Autolab (Netherlands), controlled by a USB_IF030 interface card and GPES software. The experiments were performed in a three electrode electrochemical cell containing 1 M Na_2SO_4 aqueous solution as the electrolyte at room temperature, with Ag/AgCl as the reference electrode and graphite rod as the counter electrode. The as-prepared titania nanotube structure that was used as the binder-free working electrode had nominal surface area of 1 cm.

Table 3.1 The actual and coded level of factors for Box-Behnken design

Factors	Range and levels		
Time (min)	-1	0	1
Voltage (V)	-1	0	1
NH_4F concentration (wt%)	-1	0	1

3.2.4.3 Optimization by Box-Behnken Design

Box–Behnken statistical experiment design and the response surface methodology (RSM) were used to investigate the effects of the three independent variables on the response functions and to determine the optimal conditions to maximize the titania nanotube discharge time in 1 M Na_2SO_4. The experiment design using three anodization factors (anodization time, applied potential and ammonium fluoride concentration) is as shown in Table 3.1 with all the factors having a minimum, centre point and maximum level. The optimization procedure involves evaluating the response of the statistically designed combinations, estimating the coefficients by fitting the experimental data to the response functions, predicting the response of the fitted model and checking the adequacy of the model.

3.2.5 The Fifth Project: Enhancing Electrochemical Capacitance of Anodized Titania Nanotubes Using EMIM Hydrogensulfate Ionic Liquid as Electrolyte

3.2.5.1 Electrochemical Analysis

Sample preparation for this analysis used the same method as stated in 3.2.3.1. All electrochemical experiments were done at room temperature in EMIM hydrogensulfate electrolytes which was used as received. The as-prepared titania nanotube film was used as binder-free working electrode with 1 cm^2 nominal surface area. Cyclic voltammetry (CV), electrochemical impedance spectroscopy (EIS) and galvanostatic charge-discharge testing (CD) were carried out using a potentiostat/galvanostat model PGSTAT-302N from Autolab, controlled by a USB_IF030 interface card and GPES software installed in a computer. A three-electrode electrochemical cell with Ag/Ag^+ in 0.01 M $AgNO_3$ and 0.1 M TBAP (acetonitrile) as the reference electrode and a Pt wire as the counter electrode was used in the CV experiments with scan rates from 5 mV s^{-1} to 90 mV s^{-1} between 0 V to 1.8 V. EIS measurements were performed between 100 kHz and 1 Hz under a constant potential of 0 V using a 5 mV rms sinusoidal modulation. CD was obtained using current densities from 4 μA cm^2 to 10 μA cm^2 and applied potential from 0 V to 0.6 V.

3.2.6 The Sixth Project: Influence of Flat Band Potential on Semiconducting Properties of Anodized Titania Nanotubes in EMIM Hydrogensulfate Ionic Liquid

3.2.6.1 Electrochemical Analysis

Sample for this analysis is prepared using the same method as stated in 3.2.3.1. All electrochemical experiments were done at room temperature in 0.02 M H_2SO_4 at pH 2. The as-prepared titania nanotube film was used as binder-free working electrode with 1 cm^2 nominal surface area. Cyclic voltammetry (CV), electrochemical impedance spectroscopy (EIS) and galvanostatic charge-discharge testing (CD) were carried out using a potentiostat/galvanostat model PGSTAT-302N from Autolab, controlled by a

USB_IF030 interface card and GPES software installed in a computer. A three-electrode electrochemical cell with Ag/AgCl as the reference electrode and a Pt wire as the counter electrode was used in the CV experiments with scan rates from 5 mV s^{-1} to 30 mV s^{-1} between – 0.6 V to 0.6 V. To determine the flat-band potential, EIS potential scan was used to obtain Mott-Schottky spectra by applying a small amplitude sinusoidal potential perturbation (10 mV) superimposed on the d.c. potential at f = 100 Hz. Effect of flat-band potential on semiconducting properties of titania nanotubes was investigated by EIS. EIS measurements were performed between 100 kHz and 1 Hz under constant potential of 0 V and -6 V using a 5 mV rms sinusoidal modulation.

3.2.7 The Seventh Project : Functionalization of Titania Nanotubes with Nickel Oxide Particles for Redox Type Supercapacitor

The titania nanotube was prepared using the anodization method in electrolyte containing 75 vol.% glycerol, 25 vol.% DI water and 0.5 wt.% ammonium fluoride at 20 V for 1 hour. The nanotube was successfully deposited with NiO nanoparticles via potentiostatic electrodeposition at -1.25 V in 0.02 M $Ni(Ac)_2$ aqueous solution for 30 mins. After electrodeposition, the samples were annealed at 200°C for about 2 hours in a muffle furnace in atmospheric pressure and room environment to convert the low loading of electrodeposited Ni or $Ni(OH)_2$ to NiO nanoparticles (Xie et al., 2009; Prasad and Meura, 2004; Xing et al., 2004). The annealing was done in air environment. The surface was characterized using FESEM and XRD while the supercapacitance behaviour was studied using cyclic voltammetry and charge-discharge testing.

3.3 Instrumentation

3.3.1 Autolab PGSTAT-302N Potentiostat/Galvanostat

Autolab PGSTAT-302N Potentiostat/Galvanostat has been used for investigation of electrochemical performance of titania nanotubes. The GPES software is included in Autolab PGSTAT-302N. This software can run some useful DC techniques such as cyclic voltammetery and galvanostatic charge-discharge testing. The cyclic voltammetry technique was used to study supercapacitance performance of titania nanotube electrodes. The experiments could be done at various scan rates in a wide range of potential window.

In addition, semiconduction of the surfaces was studied by electrochemical impedance spectroscopy (EIS) through the FRA software. Figure 3.1 shows the Autolab PGSTAT-302N connected to the working electrode, reference electrode and counter electrode in the electrochemical cell.

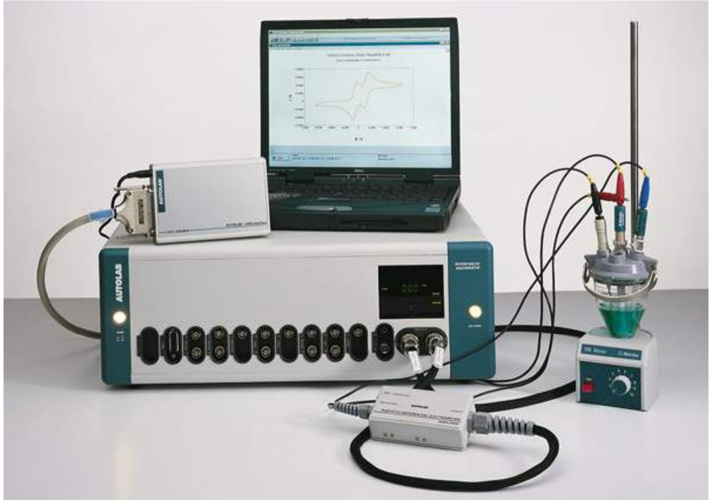

Figure 3.1 Autolab PGSTAT-302N connected to: the working electrode, reference electrode and counter electrode in the electrochemical cell (www.ecochemie.nl).

3.3.2 Field Emission Scanning Electron Microscope (FESEM) and Energy Dispersive X-Ray (EDX)

Field Emission Scanning Electron Microscopy (FESEM) is a renowned analytical methods that is among the most comprehensive. An electron microscope has many benefits in comparison to a conventional optical microscope. Among the many are high magnification, large focus depth, and high resolution. It also allows samples to be easily prepared and observed. In this technique, an electron gun produces electrons that enter the sample surface and in turn, produce numerous secondary electrons that are low in energy as shown in Figure 3.2.

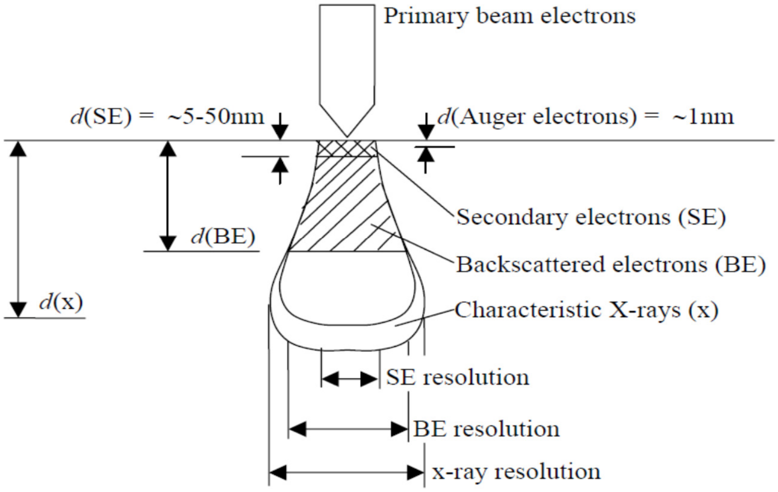

Figure 3.2 Illustrative representation of the interaction between primary electron beam and a solid surface showing the depth and volume of the interaction.

The sample's surface topography determines the secondary electron intensity of the sample. The intensity of the secondary electron is measured and used as a function of the position of the scanning primary electron beam to build an image of the surface of the sample. X-ray radiation from the sample consists of well-defined energy atoms and therefore, are used for elemental analysis. An X-ray emission occurs when an excited atom returns to its ground state. The excited atom is generated when a primary electron collides with a core electron of the sample atom that will then cause the core electron to be ejected. For elemental analysis, the SEM should be loaded with X-ray detectors.

3.3.3 X-Ray Diffraction (XRD)

X-ray diffraction crystallography for powder samples is well-established and widely used in the field of materials characterization to obtain information on the atomic scale structure of various substances in a variety of states. X-ray crystallography relies on the dual wave/particle nature of x-rays to discover information about the structure of crystalline materials.

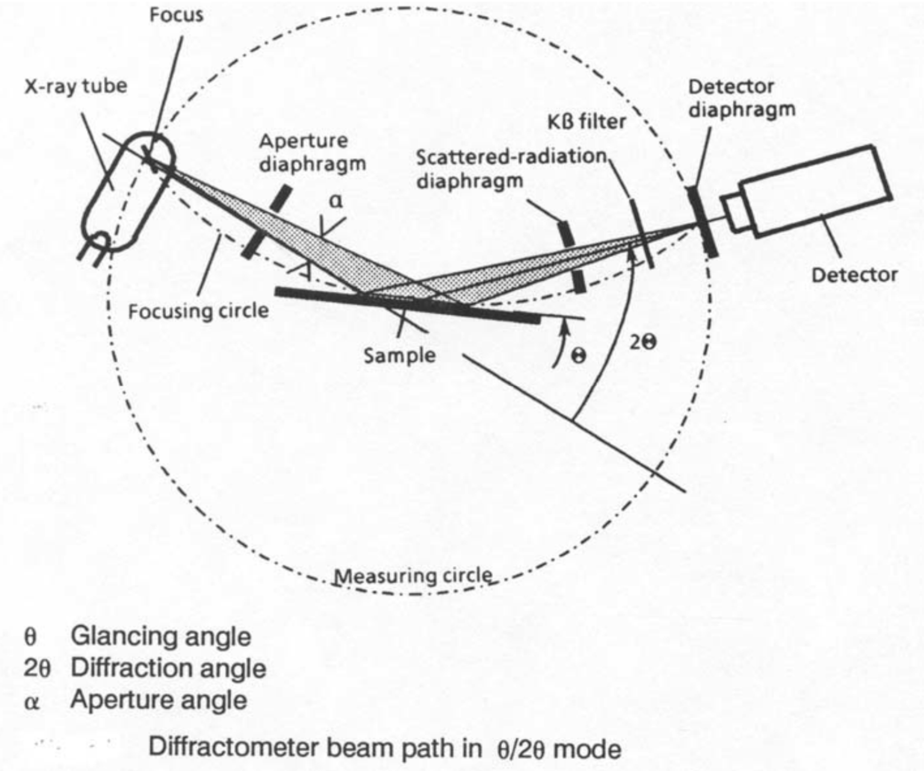

Figure 3.3 The schematic diagram of the Brukker AXS D5000 diffractometer.

The fundamentals of XRD analysis are based on Bragg's law. When X-rays of wavelength λ are incident at an angle θ on a crystal lattice, a portion of these beams will be scattered in all directions. The necessary and sufficient condition for constructive interference is known as Bragg's law. According to this law, scattered waves originating from each atom will be in phase with each other. The basic features of a typical XRD is shown in Figure 3.3, a Brukker AXS D5000 XRD unit, with an X-ray source having wavelengths of K_{α} = 1.5406 A_o. Usually, diffraction experiments are applied at a fixed wavelength; therefore, measurement of the diffraction angles enables calculation of the associated d_{hkl} and the lattice constants.

3.3.4 X-ray Photoelectron Spectroscopy (XPS)

X-ray photoelectron spectroscopy (XPS) is a quantitative spectroscopic method of measuring elemental composition, empirical formula, chemical state and electronic state of elements that is presentin a material. An XPS spectrum is produced when a material is irradiated with X-ray beams while concurrently measuring the kinetic energy and amount of electrons that has escaped from the uppermost 1 to 10 nm of the material undergoing the analysis. They interact with atoms in the surface region, causing electron to be emitted by the photoelectric effect as shown in Figure 3.4. The kinetic energies of the emitted electron given by:

$$KE = hv - BE - \Phi s \tag{3.1}$$

Where hv is the energy of the photon, BE is the binding energy of the atomic orbital from which the electron originates and Φs is the spectrometer work function. The binding energy for the elements obtained was used and compared with database to determine the composition and surface state conditions of titania nanotubes. The x-ray photoelectron spectroscopy (XPS) analysis was performed using XPS Axis Ultra from Kratos equipped with monochromatic Al Kα radiation (BE = 1486.6 eV).

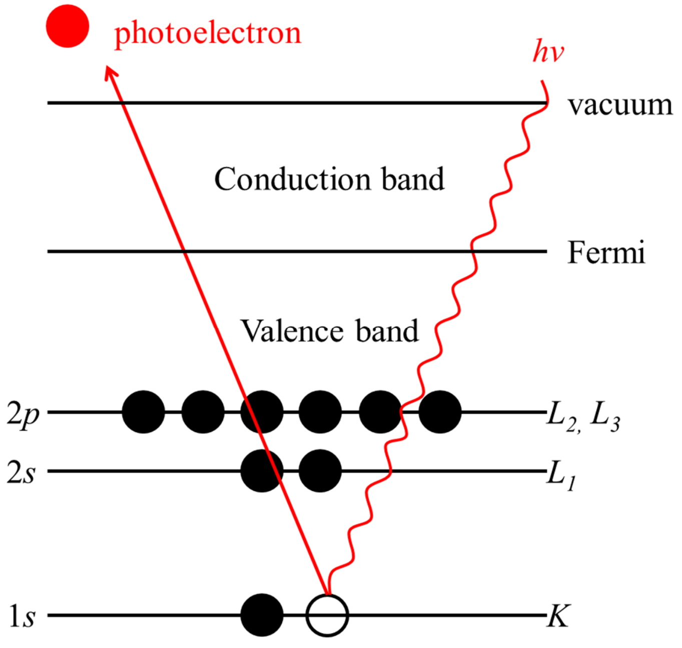

Figure 3.4 A scheme showing the principles of x-ray photoelectron spectroscopy (XPS)

CHAPTER 4

RESULTS AND DISCUSSIONS

4.1 The first project : Synthesis and characterization of vacuum annealed anodized titania nanotubes

4.1.1 Current-time characteristic

The behavior during anodization of Ti and nanotube formation can be studied by examining the current-time characteristics in the solution. Figure 4.1 shows the current-time characteristics recorded in ethylene glycol (EG) with addition of 0.5 wt% ammonium flouride and 2 vol % of DI water at 45 V. The current density decreased when the anodization time increased. This characteristic is different compared with the characteristic of anodization in aqueous electrolyte containing intermediate fluoride concentration as shown in the inset of Figure 4.1.

The inset of Figure 4.1 shows three stages: I) In the initial stage of anodization the curve essentially follows the fluoride-free case which shows the initial decay. In stage II, a current increase occurs as the reactive area increases and irregular nanoscale pores are formed. In stage III, the current drops again as a regular nanotube is formed. However, the current increase and rise in stage II before reaching a steady state value observed in the aqueous solutions was absent in this organic electrolyte as shown in Figure 4.1.

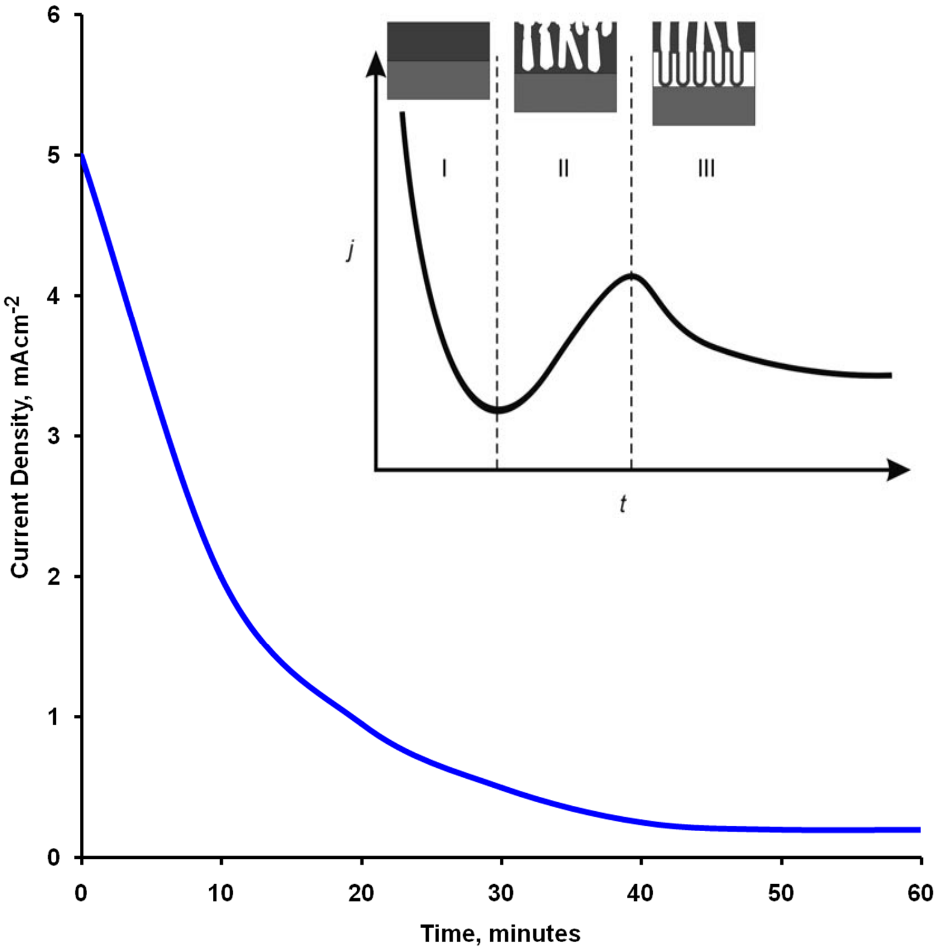

Figure 4.1 Current-time characteristic of Ti anodization in EG/NH_4F/H_2O at 45 V applied voltage for 1 hour anodization obtained in this study. The inset shows typical current/time characteristics and corresponding growth stages during self-organization process. I: initial compact oxide, II: perforated, random tubular layer, III: self-organized tube growth (Schmuki et al., 2008).

This indicates faster kinetics of a corrosion resistent barrier layer formation with the addition of water (Raja et al., 2007). The nanotube formation during early stage stage will be discussed in depth in the next project.

4.1.2 FESEM

Figure 4.2 shows FESEM image of un-anodized titanium surface. From the micrograph, the surface is flat and some debris are also noticed. The inset image shows the visual inspection and natural color of un-anodized titanium surface. After anodization at 45 V in ethylene glycol, 0.5 wt % NH_4F and 2 vol % DI water for 1 hour, the color has changed from a silver bright color to a dark yellowish color. After low-vacuum annealing at 500°C for 3 hours, the color changed to blue color (Figure 4.2 inset). High magnification analysis using FESEM indicates the surface has transformed from flat surface to porous structure containing nanotubular titania as can be seen from the top view of FESEM micrograph (Figure 4.3).

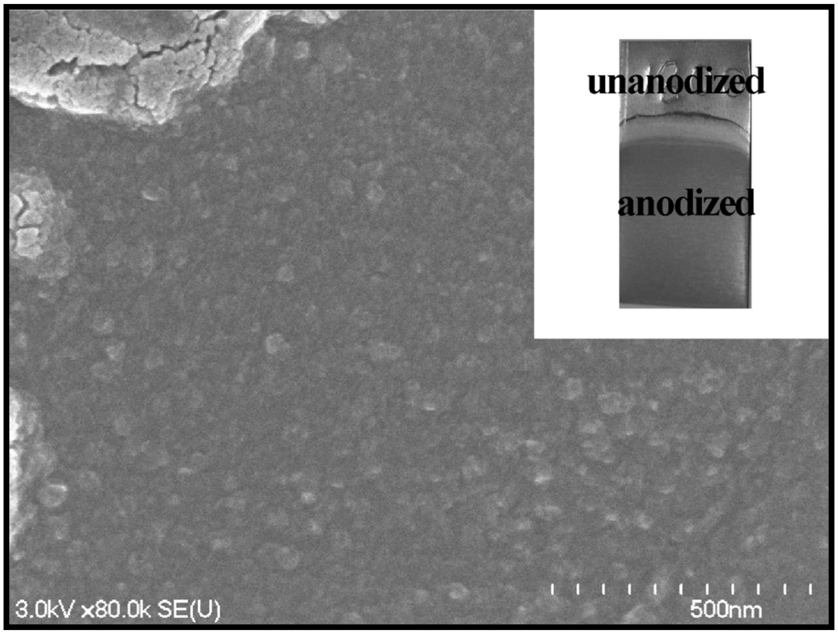

Figure 4.2 Top view of FESEM image of un-anodized surface. The inset figure shows the actual anodization sample. The color of titanium foil changed from bright silver (before anodization) to dark bluish (after anodization and annealing)

The nanotube is self-organized, highly ordered and aligned perpendicular to the substrate surface with a tube opening of around 80-90 nm in diameter. The nanotubes are attached to the metal surface, electrically connected and providing a 1D electron path if used as a supercapacitor electrode. From the Figure 4.3, the remnants or initiation layer that was produced during anodization can be seen and removed by a few techniques.

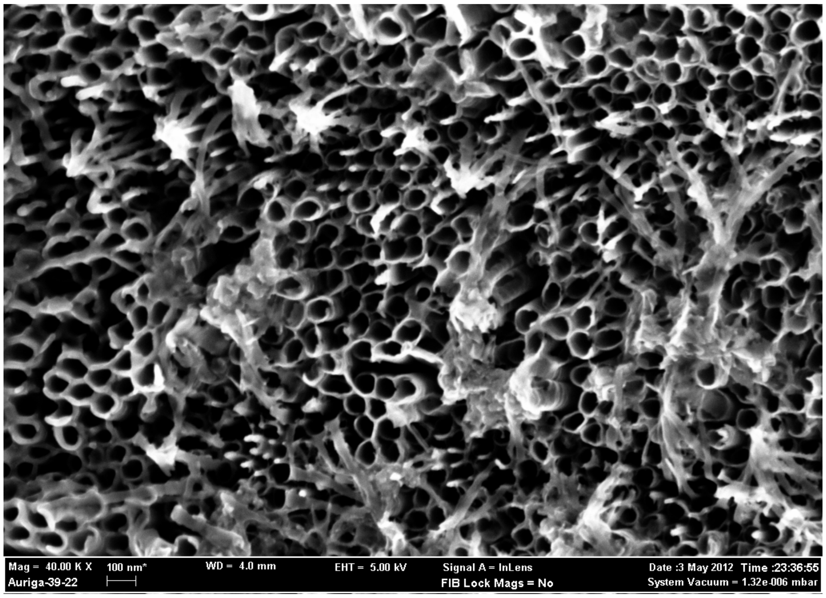

Figure 4.3 FESEM image of anodized titania nanotubes synthesized in ethylene glycol, 2 vol % DI water and 0.5 wt % NH_4F at 45 V for 1 hour anodization.

Figure 4.4 shows the FESEM images of anodized titania surface from a side view. Before anodization, the Ti surface already has a naturally thin titania passive layer around 5 nm caused by interactions between Ti and O_2 from the environment. After anodization, the thickness of the anodized titania layer or nanotube length is 1.2 μm. From the figure, the dimples are also noticed. These dimples are metallic surfaces from which the tube layers have been removed. This scalloped interface becomes visible when oxide layers are lifted off by mechanical breakaway or selective oxide dissolution. The inset figure shows the bottom of the nanotubes (Figure 4.4 inset). Table 4.1

summarizes the nanotube structure based on the FESEM measurements. The values are based on average of five measurements for each morphological parameter.

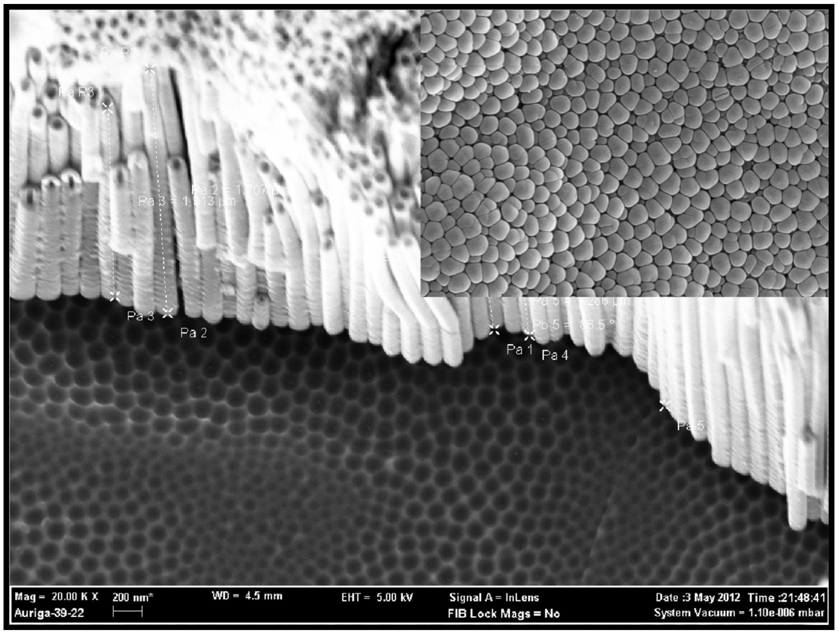

Figure 4.4 Anodized titania nanotubes from the side view. The inset image shows the bottom morphology of the nanotubes**.**

Table 4.1 Measured morphological parameter of nanotubes obtained by FESEM measurement

Morphological parameter	**Measurement**
Nanotube length	1.2 µm
Tube diameter	60 nm
Wall thickness	15 nm

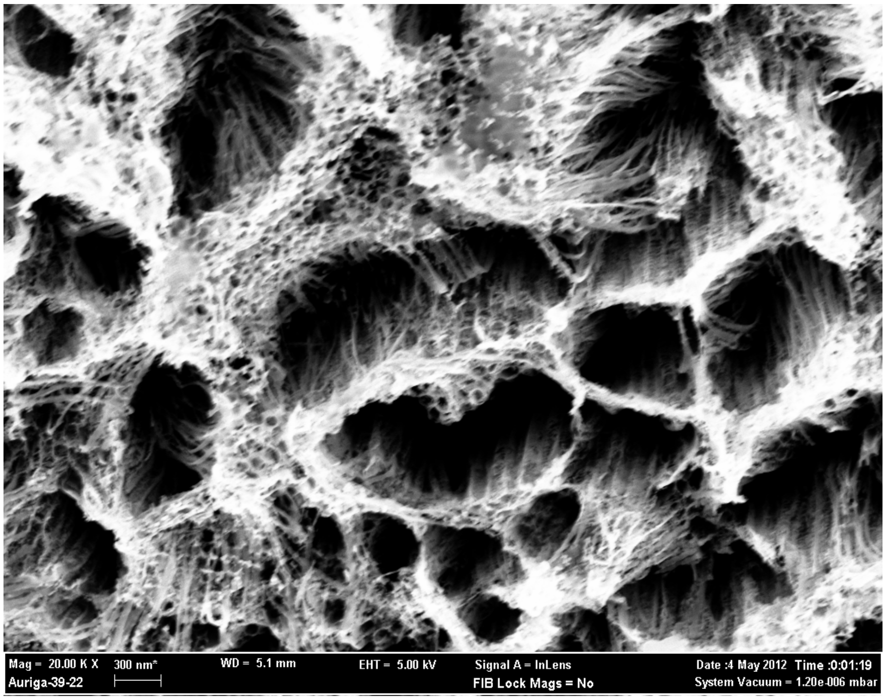

Figure 4.5 Disordered titania nanotubes growing in bundles due to un-optimized anodization process

Highly ordered titania nanotubes as shown in Figure 4.3 and Figure 4.4 can only be achieved using optimized anodization process. Factors such as anodization time, NH_4F concentration and applied anodization voltage will affect the nanotube geometry. Figure 4.5 shows the disordered titania nanotubes growing in bundles after anodization at 60 V in ethylene glycol containing 0.6 wt % of ammonium fluoride for 1 hour anodization.

In order to evaluate if the tube length can be improved by extended anodization, a time series was performed for the ethylene glycol/NH_4F electrolytes. Figure 4.6 plots the nanotube layer thickness as a function of the anodization time for the anodization in ethylene glycol containing 0.5 wt % NH_4F and 2 vol % DI water mixture at room temperature. The values were measured directly from the cross sectional images of the respective samples and based on five measurements. It shows that the nanotube layer thickness increases linearly from 1.2 μm for 1 hour to 3.2 μm for 5 hours anodization.

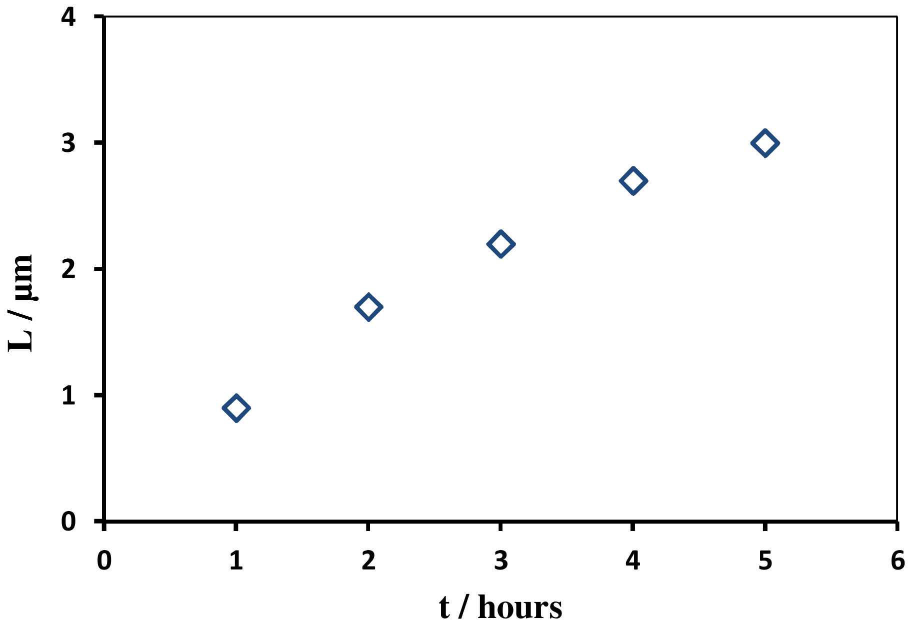

Figure 4.6 The nanotube layer thickness as a function of anodization time obtained directly from cross-section measurements of samples formed during different times in ethylene glycol + 0.5 wt.% NH_4F + 2 vol.% DI water

The effect of water content can also alter tube wall surface and a stratified layer can be obtained on the surface as shown in Figure 4.7. Figure 4.7 (a) shows the FESEM micrograph of an anodized titania nanotube with addition of 2 volume percent DI water and Figure 4.7 (b) with addition of 20 volume percent of DI water. These stratified layers (Figure 4.7b) can be synthesized using two methods: either by voltage pulsing or water-induced oscillation during anodization in organic electrolytes as shown in this work. This bamboo-type nanotubes with stratified layer will increase the aspect ratio and specific surface area and will be useful to enhance electrochemical capacitance as discussed in Section 4.3 later.

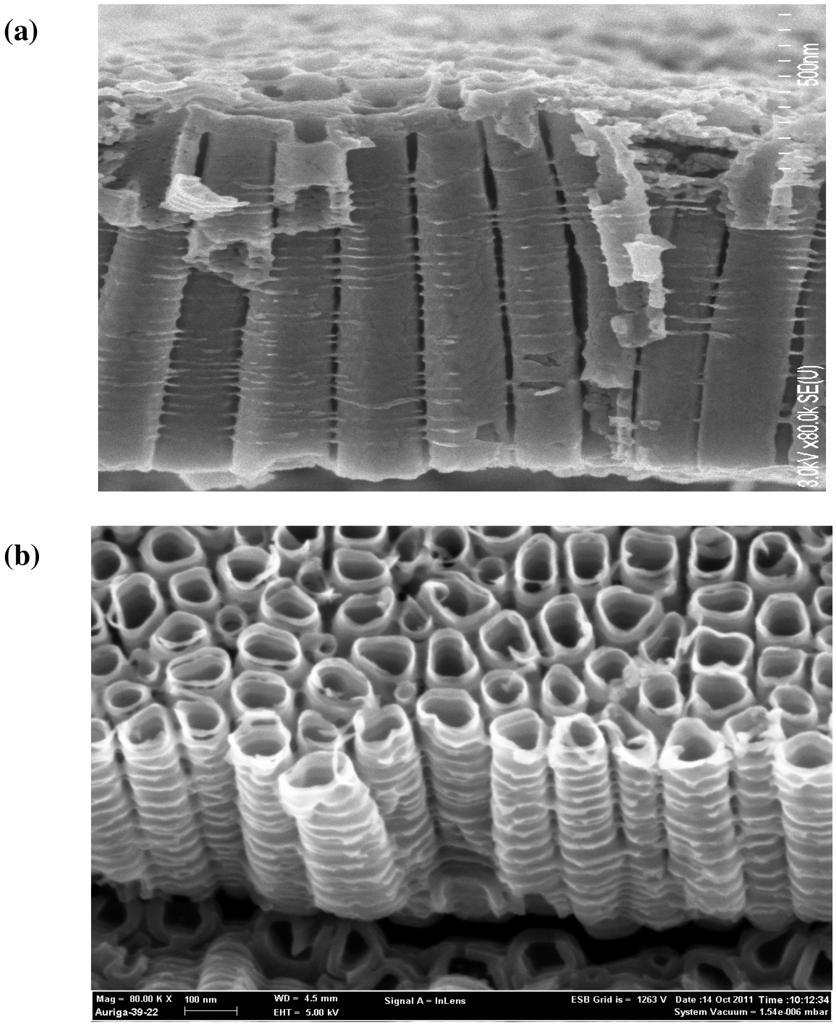

Figure 4.7 Effect of water content on anodized surface (a) 2 vol % DI water, (b) 20 vol % DI water

Low vacuum annealing was introduced to study the effects of annealing on non-stoichiometry and point defects such as oxygen vacancy and reduction of Ti^{4+} to Ti^{3+}. Titania materials are known to have high electrical resistance and low electrical conductivity. Creating non-stoichiometric titania composition with point defects will increase conductivity of titania material and improve electrochemical capacitance of titania nanotubes. Figure 4.8 depicts EDX spectroscopy of titania nanotubes after being annealed at 300°C for 3 hours in a low-vacuum furnace. From the measurements shown, apart from Ti and O species which belongs to the titania nanotube compound, a significant amount of F and C species are also present in the nanotubes. This finding can be ascribed to a residual amount of the electrolyte species that remained trapped in the inner tube. The C species comes from ethylene glycol and F species belongs to the ammonium fluoride absorbed and trapped during anodization (Ali et al., 2011).

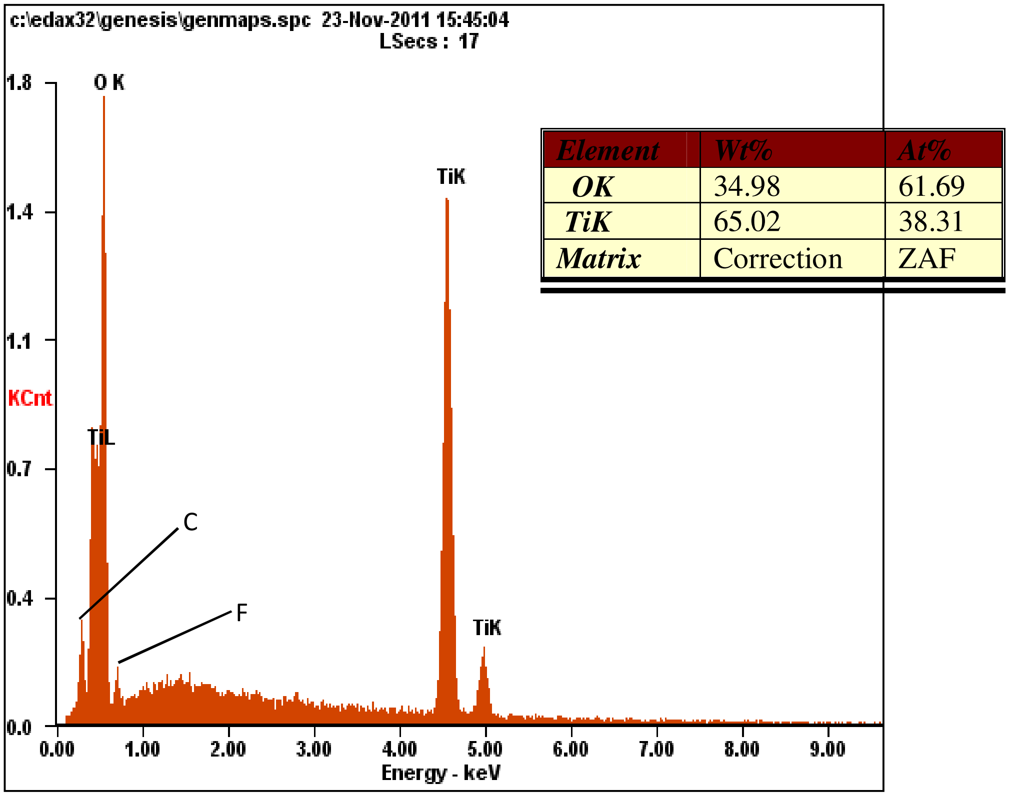

Element	*Wt%*	*At%*
OK	34.98	61.69
TiK	65.02	38.31
Matrix	Correction	ZAF

Figure 4.8 Energy dispersive X-ray spectroscopy of titania nanotubes after annealed in low-vacuum furnace at 300°C for 3 hours**.**

Interestingly, the ratio of Ti and O is approximately 1:2 in the sample of 300°C (Figure 4.8). This confirm the samples purely titania nanotubes without non-stoichiometries in its structure. In addition, there is a significant amount of F species present in the layer, coming from the fluorides (from the electrolyte) that remained inside the nanotubes after the anodization. These traces slightly influenced the EDX weight proportions.

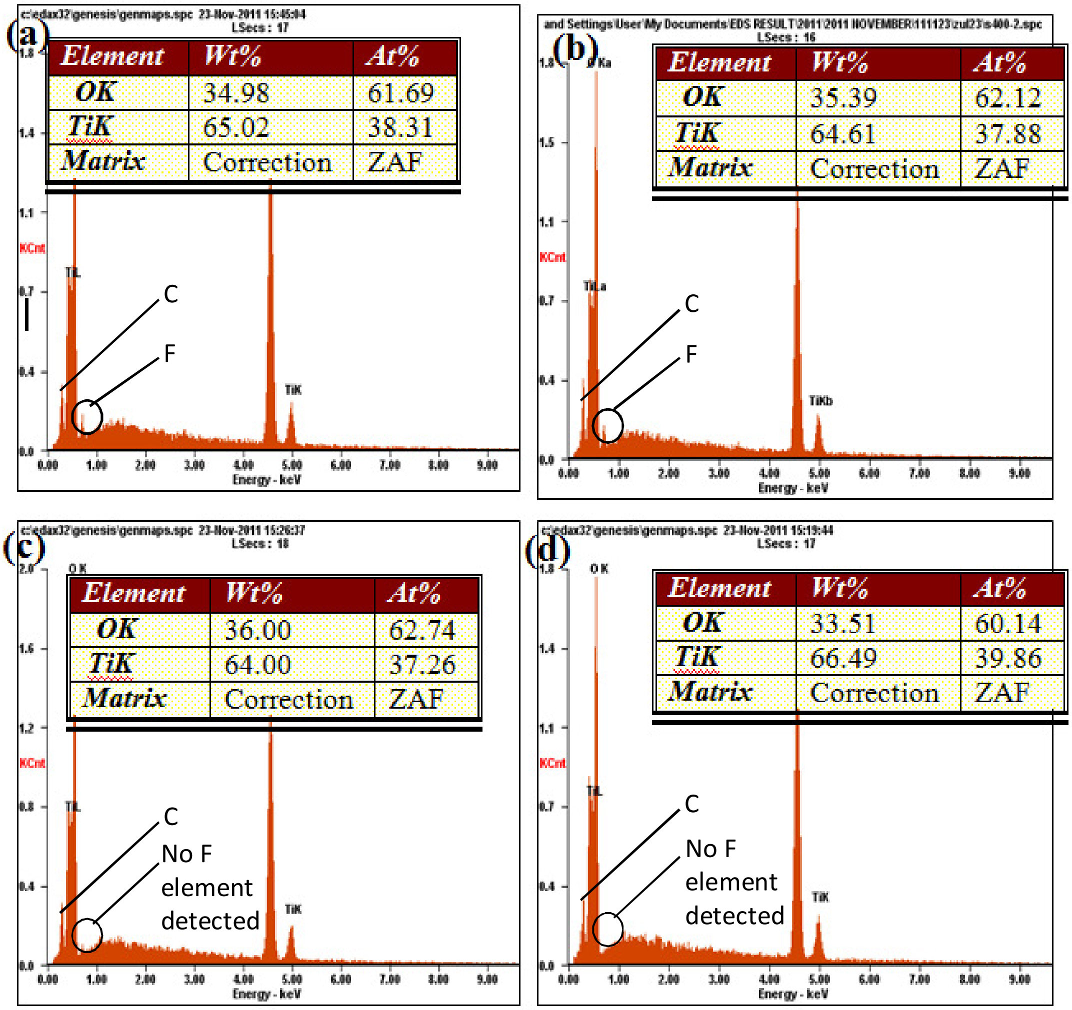

Element	Wt%	At%
OK	34.98	61.69
TiK	65.02	38.31
Matrix	Correction	ZAF

Element	Wt%	At%
OK	35.39	62.12
TiK	64.61	37.88
Matrix	Correction	ZAF

Element	Wt%	At%
OK	36.00	62.74
TiK	64.00	37.26
Matrix	Correction	ZAF

Element	Wt%	At%
OK	33.51	60.14
TiK	66.49	39.86
Matrix	Correction	ZAF

Figure 4.9 EDX measurement taken at different levels of annealing temperatures of the nanotubes in low-vacuum condition. (a) 300°C, (b) 400°C (c) 500°C, and (d) 600°C.

Figure 4.9 shows EDX measurement taken at different levels of annealing temperatures of the nanotubes. According to the EDX measurements, significant changes in the nanotubes occur, particularly the C and F concentrations are strongly reduced in the annealing process. The flourine element were not detected in 500°C and 600°C samples suggesting that the F bonding is broken during high temperature treatment or desorption has occured.

In order to study the effect of annealing temperatures on non-stochiometric titania composition, we summarized the atomic and weight percentages of Ti and O elements in Table 4.2 and plotted it in Figure 4.10. From Figure 4.10, we can see the opposite trend between Ti and O elements. The atomic and weight percentage of Ti was reduced up to the 500°C sample and gained again for the 600°C sample.

Table 4.2 Summary of weight percentage (wt%) and atomic percentage (at%) of Ti and O elements for each annealing temperature.

	Ti element		**O element**	
°C	**wt %**	**at %**	**wt %**	**at %**
300	65.02	38.31	34.98	61.69
400	64.61	37.88	35.39	62.12
500	64	37.26	36	62.74
600	66.49	39.86	33.51	60.14

The values are taken from Figure 4.8.

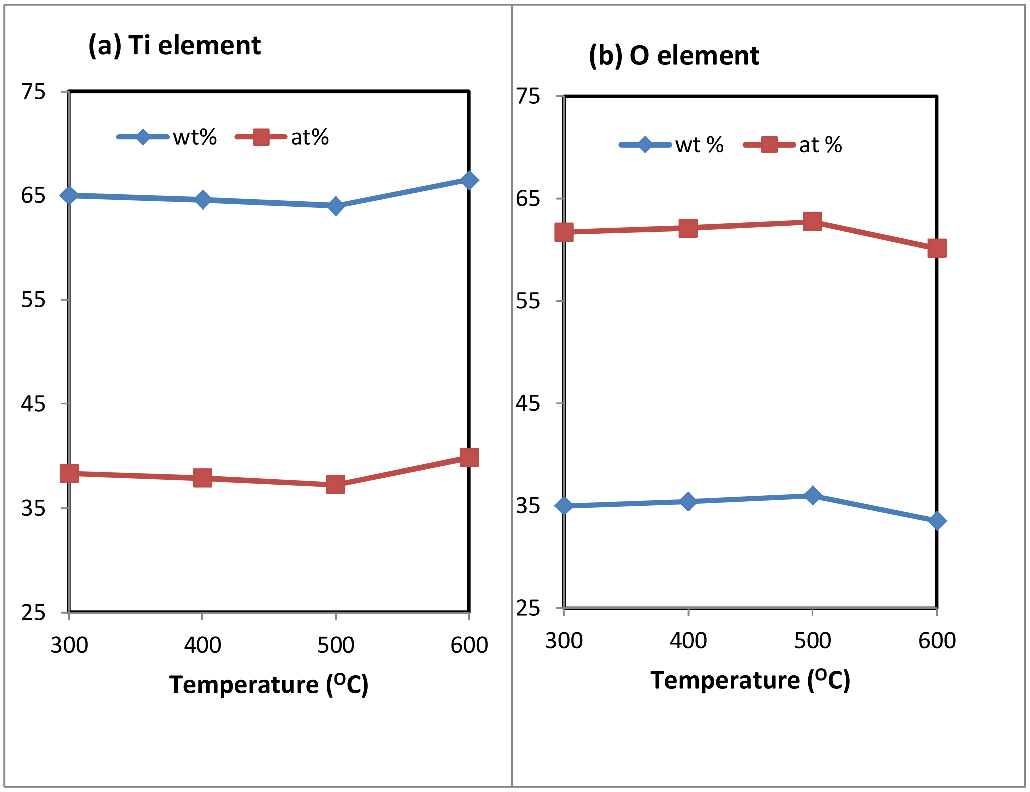

Figure 4.10 Comparison between atomic percentage (at %) and weight percentage (wt %) of Ti and O elements obtained in Table 4.2 at different annealing temperatures.

A similar trend is observed for O element but in the opposite direction. This trend suggests that the non-stoichiometric and point defect such as the reduction of Ti^{4+} cation and oxygen vacancies do not occur during low-vacuum annealing. The reduced atomic and weight percentage of Ti element for 300°C, 400°C and 500°C come from the shrinkage of titania nanotubes during annealing. Recent study has found that the nanotubes starts to shrink after thermal annealing, crack at 450°C and collapse at 650°C and above (Albu et al., 2008).

For the O element, low-vacuum annealing gives the same results as oxygen annealing because an exposure to environment during the sending of the samples to XPS will re-oxidize the titania nanotubes in which the oxygen from the environment will refill the vacated O element after low-vacuum annealing. In addition, the pressure is not sufficient to induce point defect and non-stoichiometry such as oxygen vacancies in the titania structure. Diebold found that high vacuum pressure as high as 12 Torr should be produced in order to induce oxygen vacancies in the titania materials (Diebold, 2003).

The explanation of an increased Ti element and decreased O element after 500°C annealing is assumed to have relation with transformation of crystal structure from anatase to rutile. In order to accurately confirm the EDX results and the degree of non-stoichiometry of titania, further experiments with X-ray photoelectron spectroscopy (XPS) were introduced.

4.1.3 XPS

Binding energy and intensity of the XPS results were used to confirm the composition and non-stoichiometry as well as point defects in titania nanotubes after low-vacuum annealing. The XPS revealed the chemical composition and also the oxidation states of the relevant species. Figure 4.11 shows a typical XPS wide spectrum taken at the nanotubular layer grown by anodization in ethylene glycol containing 0.5 wt% NH_4F and 2 wt % DI water at 45 V. After low-vacuum annealing at 300°C for 3 hours, the peaks of Ti and O were detected in XPS wide spectrum (Figure 4.11). F and C peaks were also detected in narrow scan (Figure 4.12) even though these two peaks could not be seen clearly in XPS wide spectrum because the intensities of the peaks are very small. These peaks are difficult to eliminate as it comes from the contamination by organic molecules adsorbed on the titania surface or adsorption occurred during anodization.

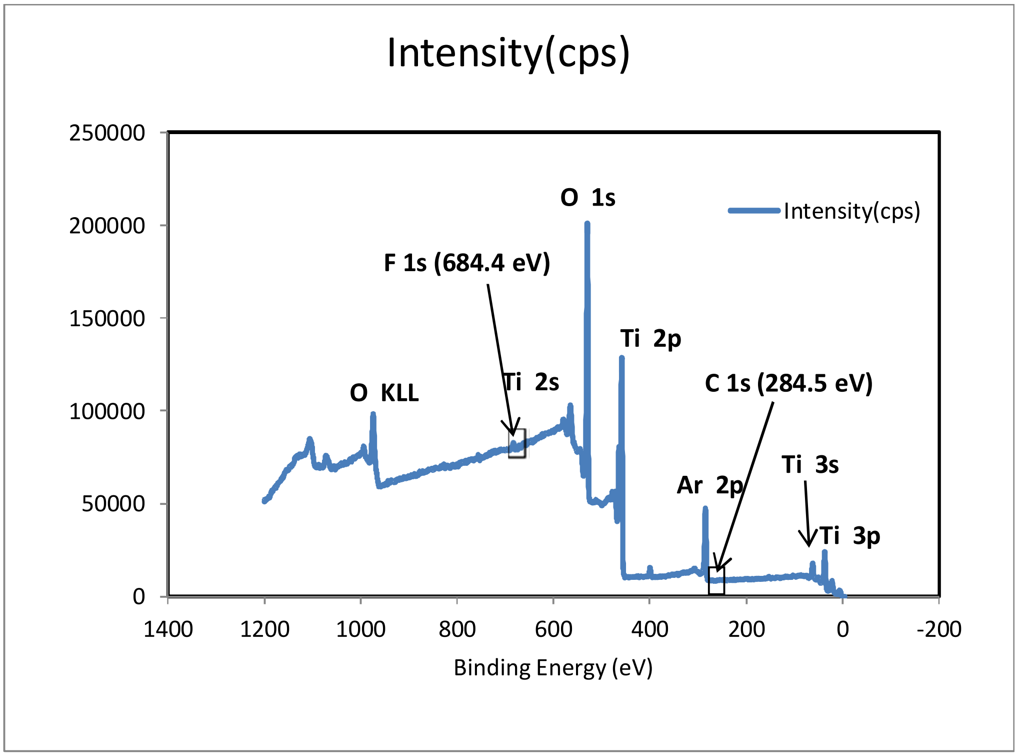

Figure 4.11 XPS wide spectrum of of anodized titania nanotubes after low vacuum annealing at 300°C for 3 hours

Figures 4.12(a)-4.12(d) show the narrow scan peaks of Ti 2p, O 1s, C 1s and F 1s XPS spectra of the sample in Figure 4.11. After calibration and curve fitting, the binding energies were obtained for each peak. Figure 4.12(a) is the Ti 2p peak showing the presence of the main doublet composed of two symmetrical peaks at binding energy, E_b (Ti $2p_{3/2}$) = 458.5 eV and E_b (Ti $2p_{1/2}$) = 464.18 eV attributed to Ti=O bonding.

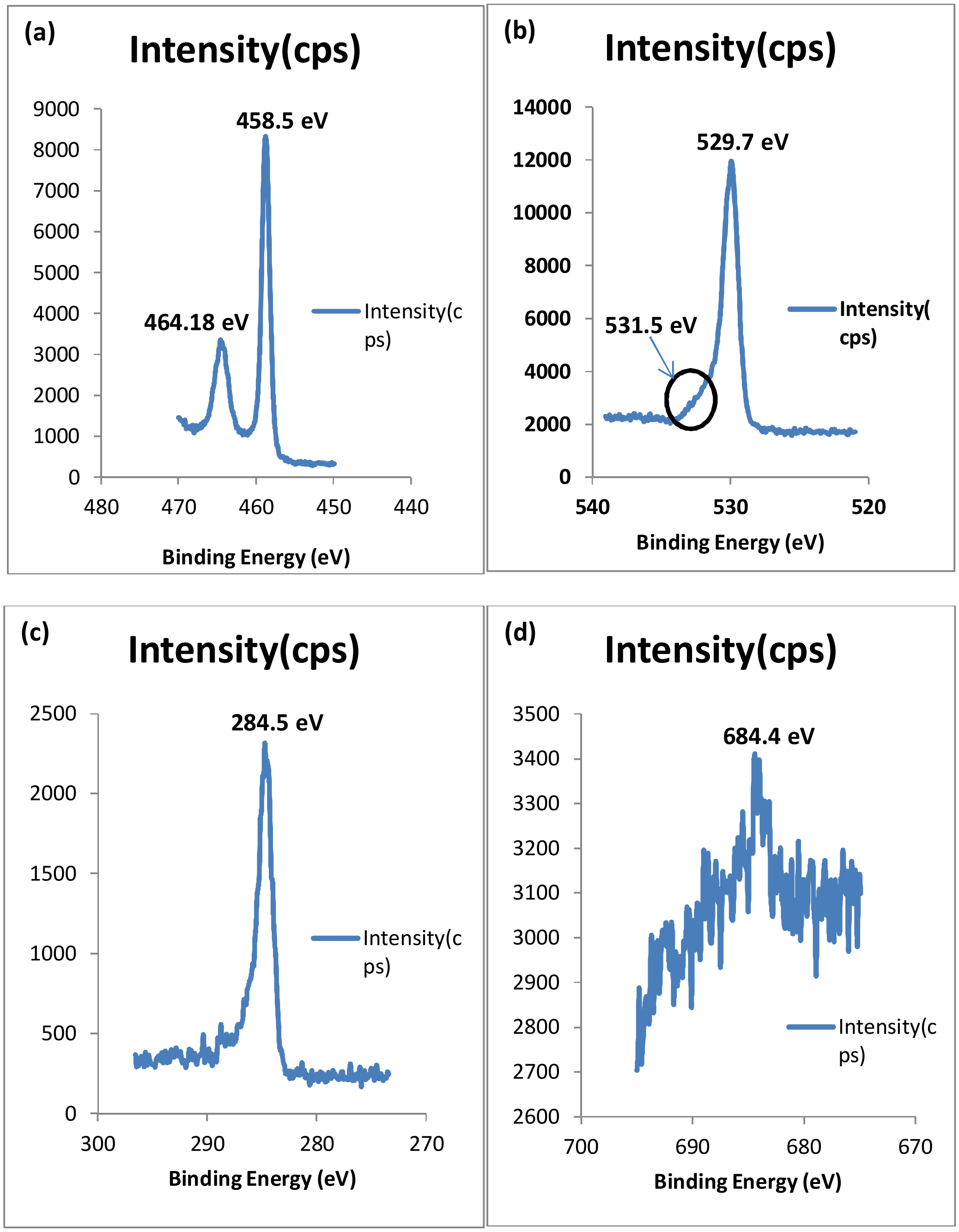

Figure 4.12 XPS spectrum for titania nanotube element after annealing at 300°C for 3 hours (a) Ti, (b) O, (c) C and (d) F

From the Figure 4.12(a) of Ti 2p element, there is no other peak was obtained indicating that the nanotubes is pure and all the surfaces are covered by the nanotubes. No Ti^{3+} or Ti^{2+} oxidation state binding energy of this sample was found either. From this, a low electrical conductivity of this material is expected. After deconvolution with

Gaussian functions, a peak at 529.7 eV was obtained for the O 1s spectrum as shown in Figure 4.12(b). The O 1s peak at 529.7 eV could be assigned to TiO_2 covalent bonding and a shoulder at 531.5 eV could be related to the presence of organic compounds with C-O or C=O bonds, possibly $(RCOO)_4Ti$ type products (Raja et al., 2007).

The existence of the C element at 284.5 eV binding energy as shown in Figure 4.12(c) can be ascribed to the adventitious hydrocarbon from the XPS instrument itself. As shown in Figure 4.12(d), the peak located at 684.4 eV can be attributed to the F^- ions adsorbed on the surface of titania nanotubes. The peak was not detected in sample 400°C and above indicating that this F^- ion is only physically adsorbed on the surface of titania nanotubes. The fluoride anion uptake during anodization is quite common for oxide layers grown electrochemically in the presence of NH_4F, or fluoride salts. The effect is usually ascribed to competition of fluoride ions with mobile oxygen ions during oxide growth, or to a specific adsorption of these ions and encapsulation by overgrowth, or to precipitation. Recently, Macak et al. (2006) showed that the fluoride content could be minimized by thermal annealing at 450°C for 3 hours.

The flourine element that were eliminated after 300°C low-vacuum annealing confirmed that this element was being physically adsorbed during anodization on the surface of titania nanotubes in ammonium flouride containing electrolyte. From this experiment, it is understood that an important factor for the fluoride incorporation into the nanotubes could be the flexibility of the amorphous state or at lower thermal annealing. Table 4.3 is the quantification report summary of deconvoluted binding energies of each element for sample annealed in low-vacuum at 300°C for 3 hours.

Table 4.3: Quantification report summary of binding energies of each element for sample annealed in low-vacuum at 300°C for 3 hours

Peak	Position BE (eV	FWHM (eV)	Raw Area (cps V)	RSF	Atomic Mass	Atomic Conc %	Mass Conc %
O 1s	529.711	1.402	15592.7	0.78	15.999	41.29	32.27
O 1s	531.5	1.671	2655.5	0.78	15.999	7.03	5.49
Ti 2p	458.5	1.515	12796	2.001	47.878	13.27	31.03
Ti 2p	464.187	1.828	4650.8	2.001	47.878	4.82	11.27
F 1s	684.4	2.048	524.7	0.477	14.007	2.28	1.56
C 1s	284.502	1.894	4213.9	0.278	12.011	31.31	18.37

In order to confirm if low-vacuum annealing can produce non-stochiometry in titania nanotube composition as found in previous EDX results, the comparison of deconvulated binding energy of Ti 2p for Ti element is done as shown in Figure 4.13 and Table 4.4 for annealing temperatures of 300°C, 400°C, 500°C and 600°C. According to XPS measurements of high-energy resolved Ti $2p_{3/2}$, the Ti $2p_{3/2}$ peaks for all annealing temperatures located in the range of 458.5 eV and 458.95 eV can be attributed to Ti^{4+}. No Ti^{3+} shoulder at lower binding energy on the Ti $2p_{3/2}$ peak is detected, suggesting that all samples have a stoichiometric titania surface. It means that the annealing treatment in this study is still not enough to produce Ti^{3+} oxidation state and not sufficient to produce non-stoichiometry in the nanotube composition. Annealing in reducing gas such as in ammonia (Zhang et al., 2010) or carbon monoxide (Xiao et al., 2011) could be applied in order to produce Ti^{3+} oxidation state and oxygen vacancies. However, this low-vacuum annealing regime can change the crystal structure of the nanotubes as shown in XRD results later.

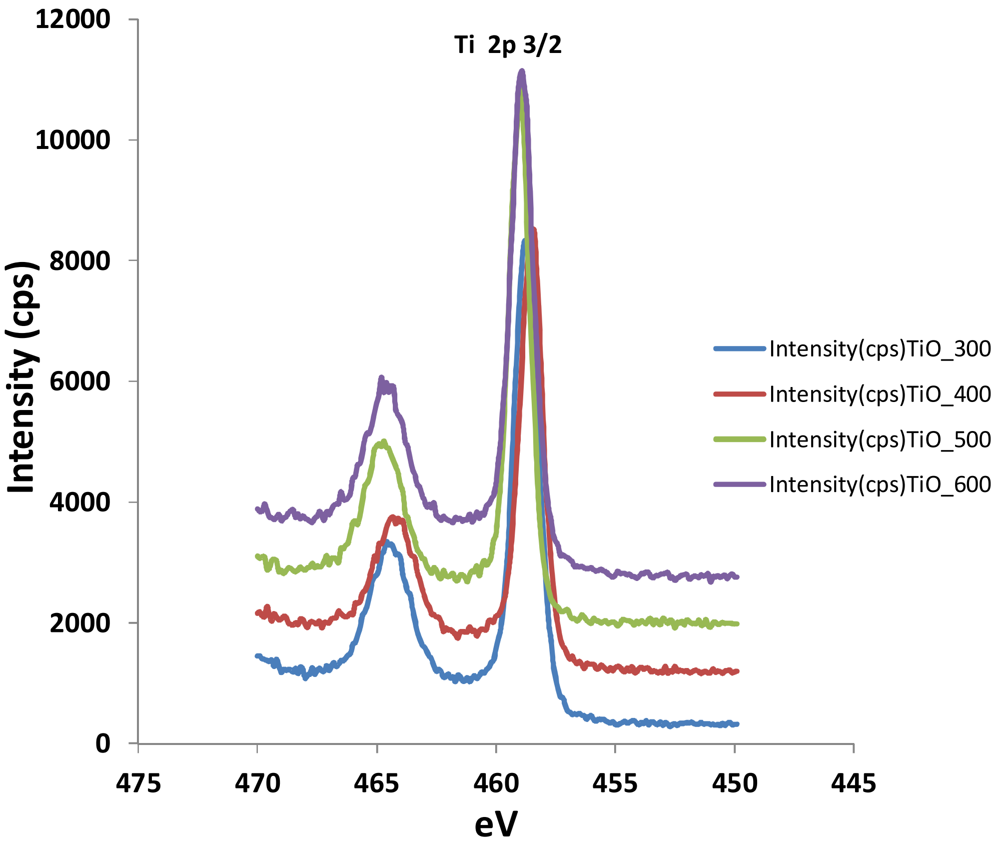

Figure 4.13 XPS for Ti 2p for different annealing temperatures

Table 4.4 Binding energy of Ti 2p for different annealing temperatures

Temp (°C)	Position BE (eV)	FWHM (eV)	Raw Area (cps eV)	RSF	Atomic Mass	Atomic Conc %	Mass Conc %
300	458.5	1.515	12796	2.001	47.878	13.27	31.03
400	458.637	1.217	9528.3	2.001	47.878	8.47	22.71
500	458.7	1.485	13941.9	2.001	47.878	10.62	27.74
600	458.95	1.49	13149.2	2.001	47.878	10.19	26.23

4.1.4 XRD

To analyze the impact of low-vacuum annealing on the structure of the crystal, examination of their crystalline structures was done after the annealing process at 300, 400, 500, and 600°C for 3 h in low-vacuum furnace. Figure 4.14 depicts the X-ray diffractograms of titania nanotubes after annealing at various temperatures. It is well known that anodized titania nanotubes is in an amorphous state before the annealing treatment (Beranek et al., 2003; Albu et al., 2008; Albu et al., 2010). After the annealing process, the amorphous structure transforms into the crystalline phase (Figure 4.14). From the figure, the annealing done on samples at 300, 400 and 500°C are mostly anatase. In contrast, the annealing done at 600°C on the sample consists of anatase along with rutile in considerable amounts; however anatase weight fractions were reduced. Above 500 ^{o}C, the rutile phase starts to appear, and with a further increase in the annealing temperature the quantity of rutile increases.

The annealing duration and ramping speed also has a significant effect on the crystal structure of titania nanotubes and furthermore affects the composition of the nanotubes. For instance, at 900 ^{o}C and relatively short-time annealing (2 hour) and with a ramping speed of 1^{o}C s^{-1}, the titania nanotube layer is completely converted into a rutile structure (Schmuki et al., 2011). However, the ramping rate and temperature of 10 ^{o}C s^{-1} and 600 ^{o}C, respectively, that are used in this experiment may not sufficient to have a complete anatase to rutile conversion. From the kinetic point of view, the phase transformation from anatase to rutile makes the Ti-O bonds of the anatase phase break and are re-arranged to form rutile (Shannon and Pask, 1965; Pan and Ma, 2004; Salari et al., 2011).

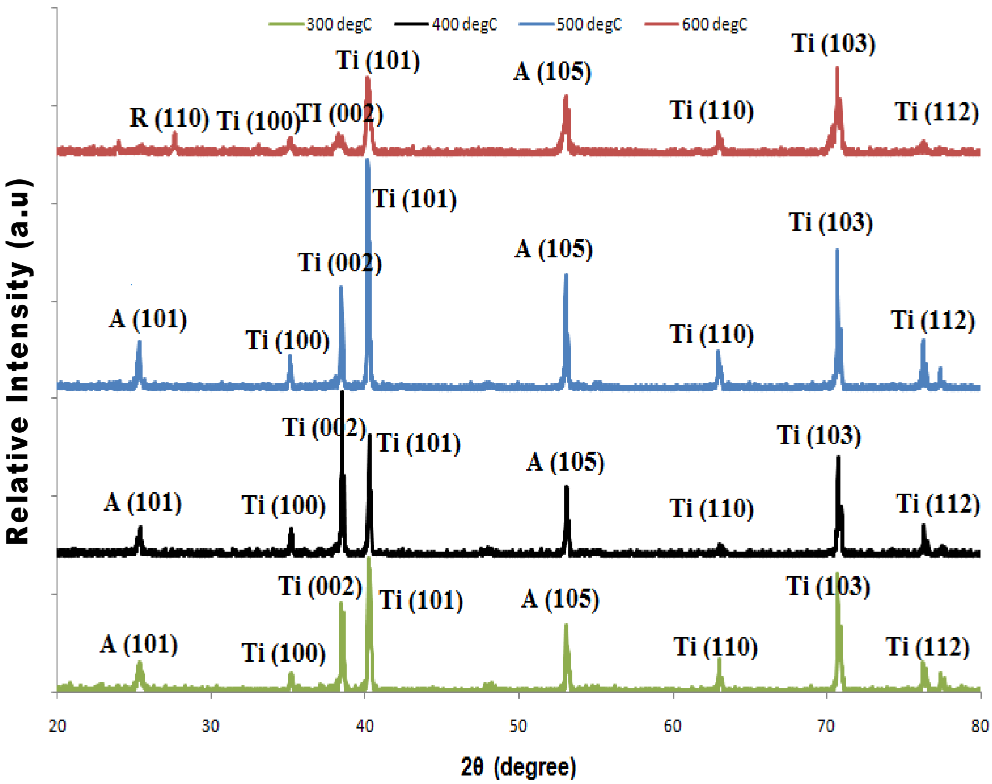

Figure4.14 XRD spectrum of titania nanotubes after vacuum annealing at different temperature

4.2 The second project : Titania nanotube formation and its application as a binder-free supercapacitor electrode

Anodizing of titanium generates a wide array of colors without applying an organic dye or artificial coating to the surface of the metal. It is an electrolytic process that slightly manipulates the native oxide layer of the titanium, generating a perceived color. As the molecules of the oxide layer increase in thickness, light entering the layer refracts at different angles, resulting in the color we see, similar to how a prism works. The color perceived through the oxide layer will not change, fade or discolor over time. Since we are simply observing a perceived color, the base substrate of the titanium remains unchanged and the oxide layer stable and passive. The color of anodized titanium surface also shows the stage of nanotube formation during anodization.

Figure 4.15 shows the image of an anodized surface taken by visual inspection for different anodizations from 0 s to 1800 s. Before anodization, the sample had the original silver bright color. After 5 s of anodization, the color of the surface turned to dark blue color and then changed to a bright blue color for 10 s. The color than transformed to a bluish silver for the 30 s sample and finally obtained its dark yellow color. This color can be used as an indicator to predict the surface of anodized titania in high magnification. The dark yellow is found as the color of ordered titania nanotube formation. After annealing, the color will change to a combination of dark yellow and blue color.

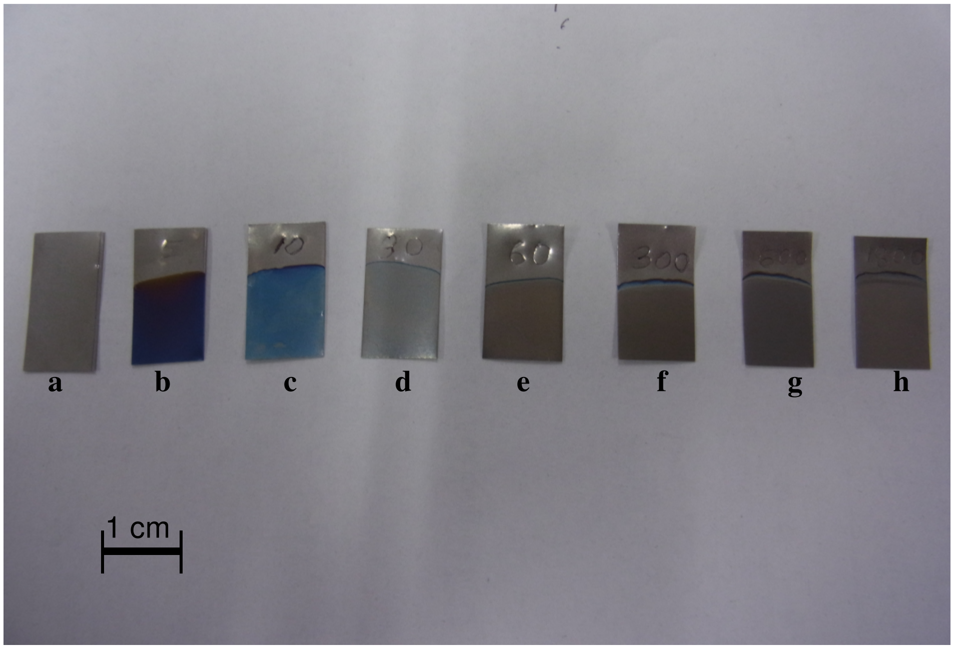

Figure 4.15 Color changes of anodized surface taken by visual inspection for different anodization times (a) Un-anodized, (b) 5 s, (c) 10 s, (d) 30 s, (e) 60 s, (f) 300 s, (g) 600 s and (h) 1800 s

4.2.1 FESEM

Generally, the key process which contributes to the formation of anodized titania nanotubes can be explained by using the same approach as the anodized alumina nanotubes (Su et al., 2008; Mor et al., 2003). Figure 4.16 depicts the surface morphology of the samples anodized at 45 V for 1800 s anodization in 0.5 wt. % NH_4F and 2 vol. % DI water in ethylene glycol electrolyte. The titania nanotube formation can be analyzed by subjecting the surface to FESEM analysis and obtaining its morphology during an early growth. The anodization times for this analysis as shown in Figure 4.17 were 5 s, 10 s, 30 s, 60 s, 300 s and 600 s.

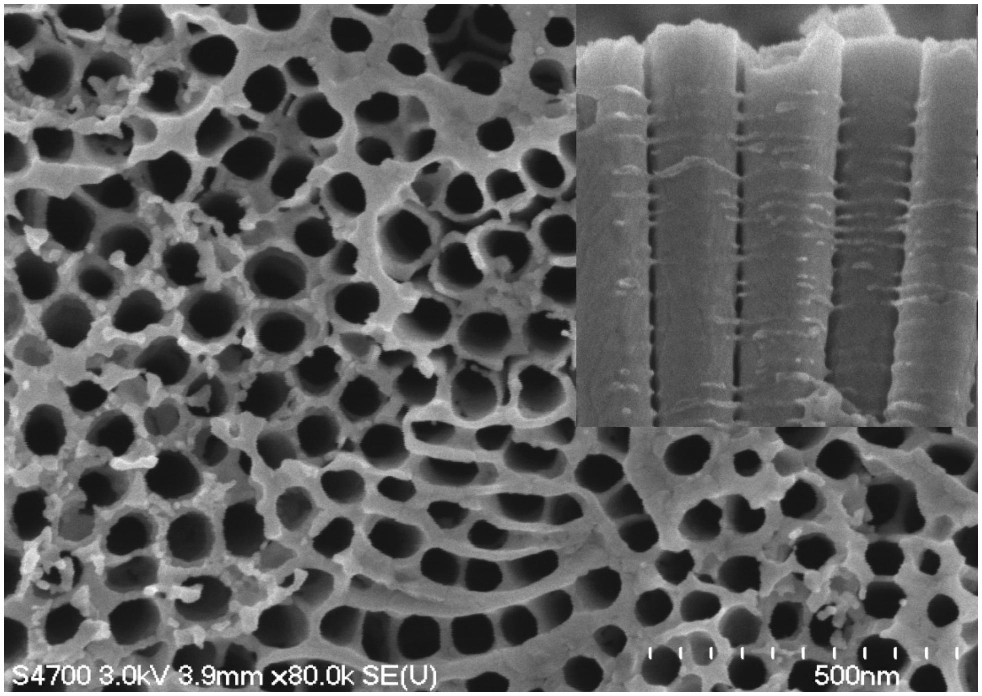

Figure 4.16 Surface morphology of the samples anodized at 45 V for 1800 s anodization in 0.5 wt.% NH_4F and 2 vol.% DI water in ethylene glycol electrolyte. (Inset) Nanotubular structure from the side view.

Figure 4.17(a) is the FESEM image of the titanium foil surface after 5 s anodization time. From this image, the initial dense oxide layer with small nanopit formation uniformly scattered across the surface is due to the chemical dissolution process, i.e. from the interaction of the Ti^{4+} ions on the surface with oxygen ions (O^{2-}) in the electrolyte (Zhou et al., 2008).

At 10 s anodization time (Figure 4.17b), the nanopits grow and become larger due to the localized dissolution of the oxide. At this stage, field assisted dissolution is dominant compared to the chemical dissolution process due to the relatively large electric field across the thin oxide layer. Extended anodization time of 30 s will transform the nanopits to nanopores as shown in Figure 4.17c. The nanopit initially is a pore formation centre and will become high density pores when the anodization time increases as shown in Figure 4.17d for the 60 s sample, due to integration between the nanopores and the nanopits.

With further increase of the anodization time to 300 s, a deeper nanotubular structure starts to appear due to the integration of the larger and smaller pores as shown in Figure 4.17(e). A clearer nanotubular structure of the titania surface after 600 s anodization time is shown in Figure 4.17(f). The smaller pores located between the larger pores also serve as a separation point for the creation of the nanotubular structure (Taveira., 2005). At 1800 s anodization time (Figure 4.16), a highly ordered discrete titania nanotube structure is established when the chemical dissolution rate of the oxide at the mouth of the tube is equal to the rate of inward movement of the metal– oxide boundary at the base of the tube, and this effect slows the thickness growth of the tubular structure (Su et al., 2011).

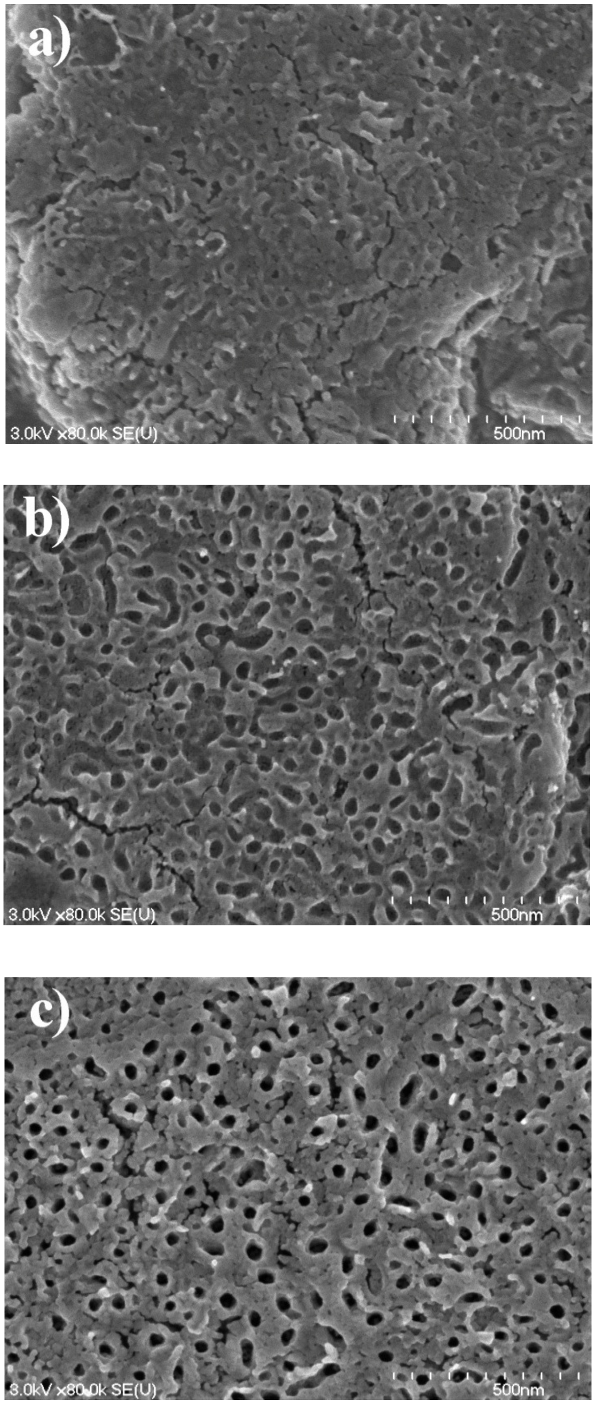

Figure 4.17 FESEM images of anodized titania surface from different anodization time (a) 5 s sample, (b) 10 s sample (c) 30 s sample, (d) 60 s sample (e) 300 s sample and (f) 600 s sample

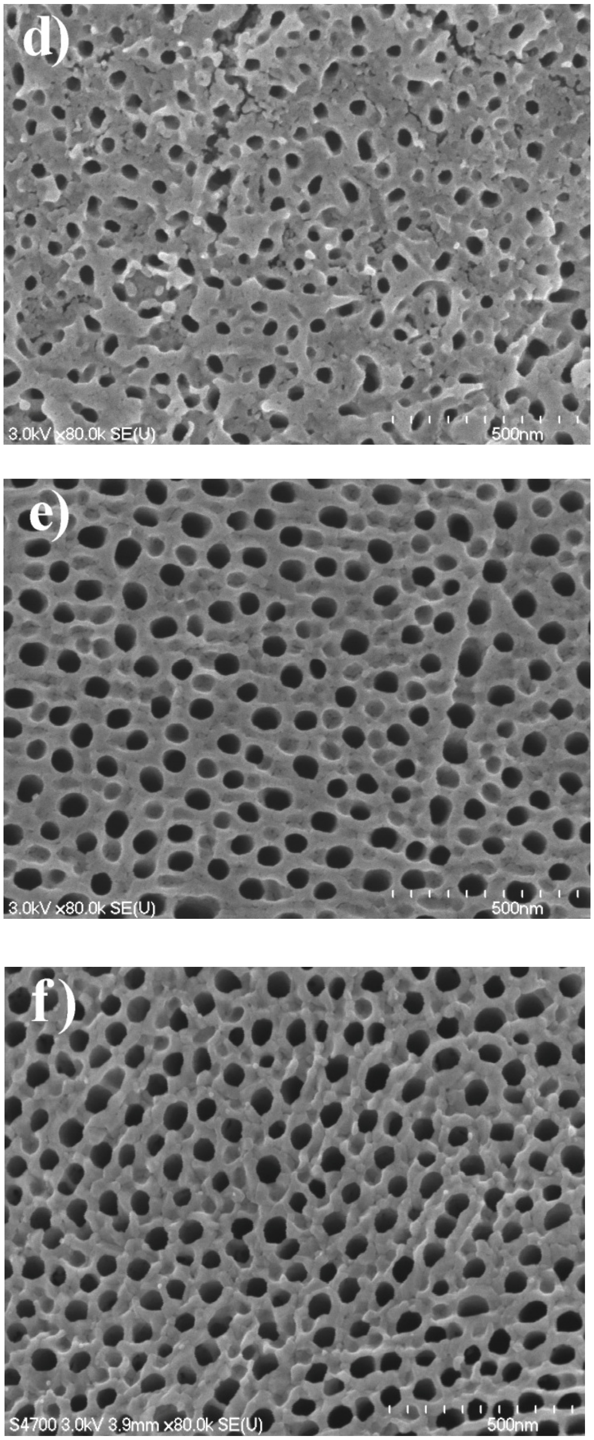

Figure 4.17 (Continue): FESEM images of anodized titania surface from different anodization time (a) 5 s sample, (b) 10 s sample (c) 30 s sample, (d) 60 s sample (e) 300 s sample and (f) 600 s sample

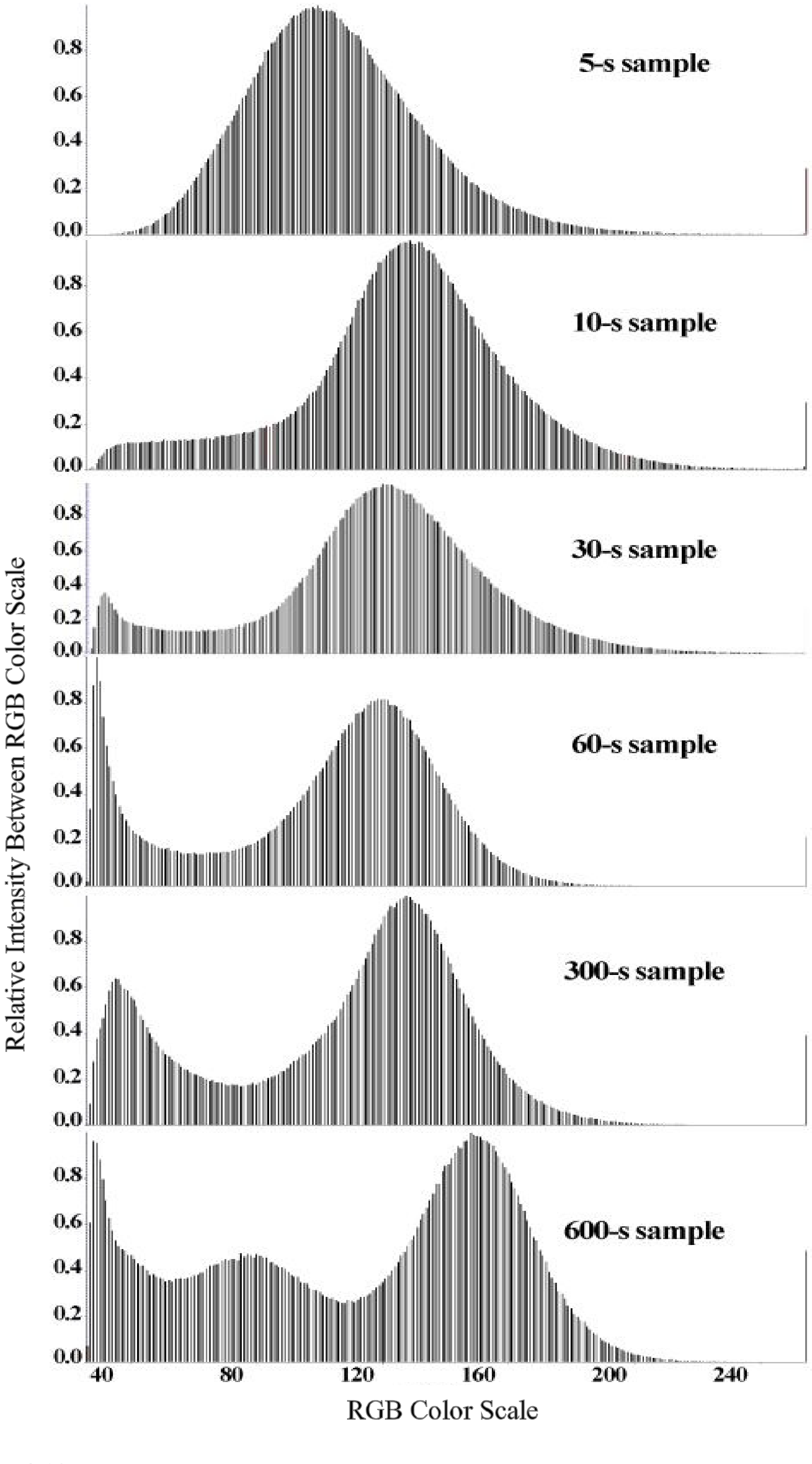

Figure4.18 Histograms of surface morphology at different anodization time generated by using FEMTOSCAN image analysis software. X-axis is RGB color scale and Y-axis relative intensity of RGB color scale

To further analyze the nanotube formation, the FESEM images in Figure 4.17 were subjected to FEMTOSCAN image analysis and the surface height distribution of each images (Z-axis) were plotted using histogram menu. The surface height distribution could be distinguished by investigating the differences of the color intensity between all the images. The color intensity of the images in Figure 4.17 were converted to RGB scales where 1 RGB scale represents the color intensity of the darkest area of the images and 240 RGB scale represent the color intensity of the brightest area of the images. From this technique, the theory of nanopits as pores and nanotube formation centres can be distinguished by monitoring the RGB intensity color relative count changes at 40 RGB scale. At this RGB scale value, the activities of nanotube formation from nanopits to pores and finally to nanotubes structure could be monitored.

Figure 4.18 shows the histograms of color intensities of FESEM images generated by FEMTOSCAN. X-axis indicates the surface height distribution and represented by the RGB color scale from 0 to 240 RGB. Meanwhile, Y-axis represents the count of the intensity using a relative scale from 0 to 1. The relative count peak found at 120 RGB scale for 5 s sample indicates the low surface roughness of the sample and the chemical dissolution process is still at the beginning stage. For 10 s sample, the relative count starts to develop at 1 to 60 RGB scale. This darker area development (Figure 4.17b) indicates the formation of nanopits. At 30 s sample, a relative count peak developed at low RGB scale of 40 indicating that the nanopits become larger and deeper. These nanopits behaved as the origin of nanopores and nanotubes. These nanopits then grew and transformed to complete nanotubes structure at 600 s sample. The relative count for RGB scale of 40 for this sample has achieved the highest value.

The formation of nanotubes in fluoride containing electrolytes is the result of the interplay between three processes occurring simultaneously (Su and Zhou, 2009); field assisted oxidation of the Ti metal to form titania, field assisted dissolution of the Ti metal to form titania and chemical dissolution of the Ti metal and titania due to etching by the fluoride ions. The following equations represent the oxide layer formation (4.1) and (4.2), and dissolution (4.3) and (4.4):

$$2H_2O \rightarrow O_2 + 4H^+ + 4e^- \tag{4.1}$$

$$Ti + O_2 \rightarrow TiO_2 \tag{4.2}$$

$$TiO_2 + 6F^- + 4H^+ \rightarrow [TiF_6]^{2-} + 2H_2O \tag{4.3}$$

$$Ti^{4+} + 6F^- \rightarrow [TiF_6]^{2-} \tag{4.4}$$

4.2.2 Cyclic voltammetry

Cyclic voltammetry is used to investigate electrochemical capacitance of titania nanotubes for different anodized titania morphologies. From this analysis, early results for the performance of anodized titania nanotubes as supercapacitor electrode can be investigated. Figure 4.19 shows the cyclic voltammograms of the titania nanotubes electrode in 1 M Na_2SO_4 for 10 s, 30 s, 600 s and 1800 s anodization time with scan rates from 5 mV s^{-1} to 70 mV s^{-1} and the potential scan between 0 V to 0.6 V. This scanning range is used in order to make the result comparable with the literatures. The CVs for 10 s anodization time (Figure 4.19a) shows a nearly rectangular and symmetrical shape for scan rates of 5 mV s^{-1}, 10 mV s^{-1} and 20 mV s^{-1} which indicates a reversible process (Wang and Pilon., 2012). However, at 30 mV s^{-1} and above, the CVs have irreversibly unsymmetrical shapes where the anodic region is distorted. From the CVs, no redox peaks are observed at these scan rates, therefore the nanotubes show electrical double layer capacitance behaviour. The irreversibly distorted CVs at scan rates higher than 30 mV s^{-1} is due to the breakdown of the oxide surface and dissolution, originated from the electrical field during the CV experiment. From the previous FESEM image shown in Figure 4.17b, the original surface of 10 s anodization sample contained nanopits due to the localized oxide dissolutions during anodization. At this stage, the anodized surface have a very thin oxide layer with nanopit formation on its surface, which is unstable and poorly adhered to Ti metal to sustain electrical field at 30 mV s^{-1} scan rate and resulted in the breakdown of the oxide surface.

For the 30 s anodization sample shown in Figure 4.19b, the CVs also show a symmetrical and nearly rectangular shape for all scan rates from 5 mV $s^{-1}$to 70 mV s^{-1}. This indicates that the process is highly reversible and the nanotube capacitance behaviour is based on the electrical double layer principle. The CV shape is not distorted compared to Figure 4.19a which indicates that the oxide layer is strongly adhered to the Ti surface and no oxide layer breakdown occurred at the specified scan rates. For the 600 s anodization sample (Figure 4.19c), the same reversible characteristic are observed as in Figure 4.19b but with higher current density which indicates the influence of porosity of the surface (Arulepp et al., 2004). The larger pores and nanotubular structure increased the current density as the specific surface area is increased. The effect of increased specific surface area can also be seen in the 1800-s anodization sample (Figure 4.19d) where the highest current density was obtained for 5 mV s^{-1} scan rate.

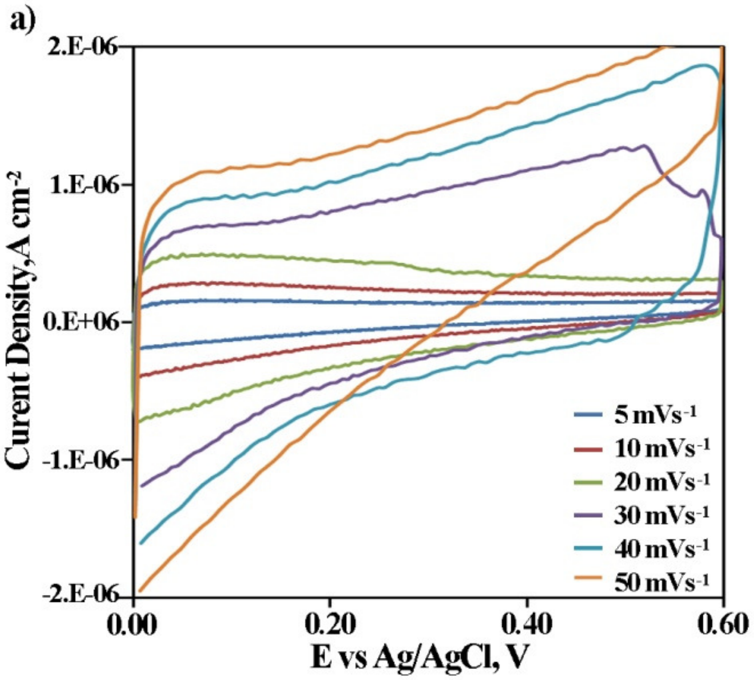

Figure 4.19 (a) The CVs for anodized titania nanotubes in 1 M Na_2SO_4, (a) 10-s sample

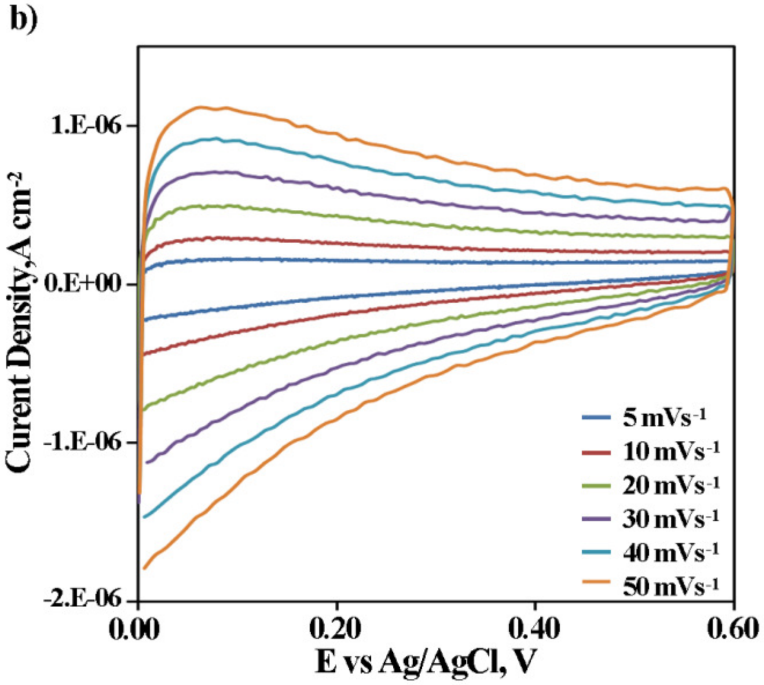

Figure 4.19 (b) The CVs for anodized titania nanotubes in 1 M Na_2SO_4, (b) 30-s sample

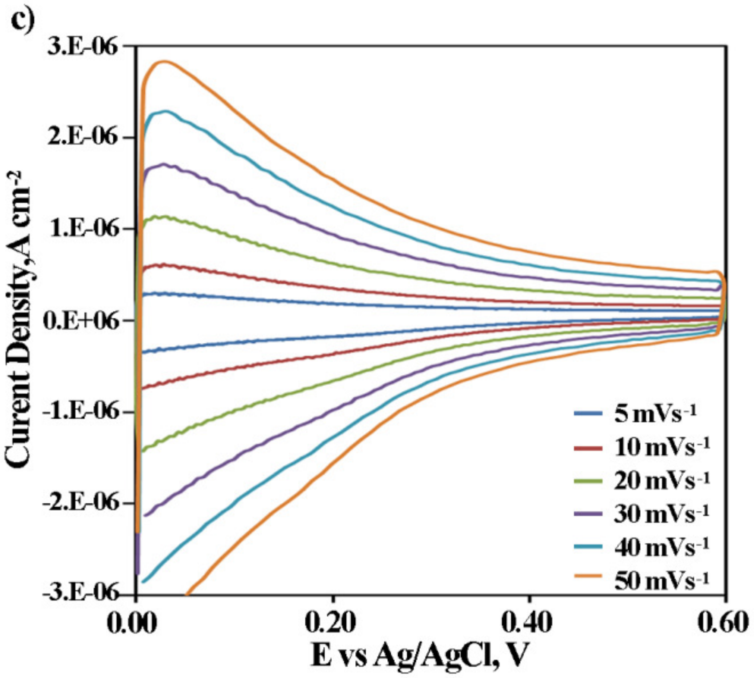

Figure 4.19 (c) The CVs for anodized titania nanotubes in 1 M Na_2SO_4,
(c) 600-s sample

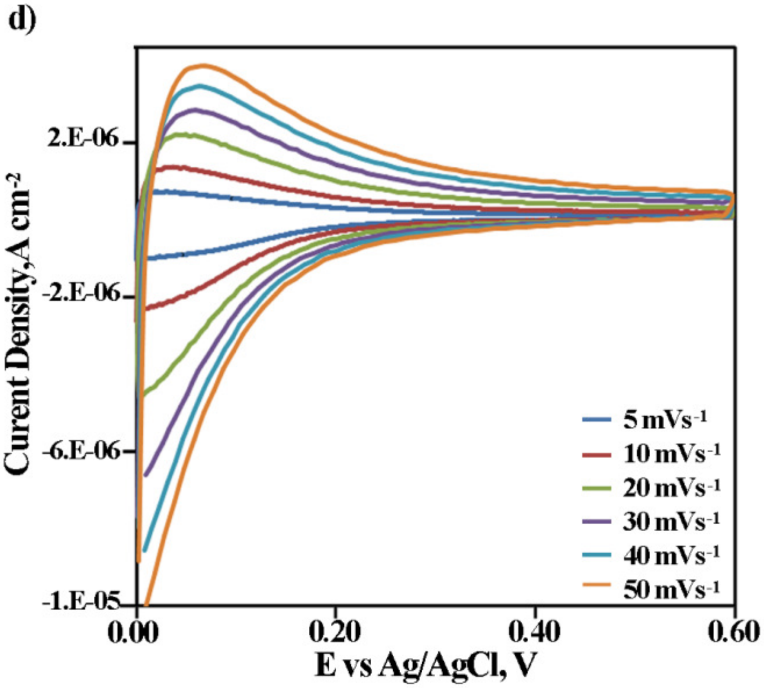

Figure 4.19 (d) The CVs for anodized titania nanotubes in 1 M Na_2SO_4,
(d) 1800-s sample

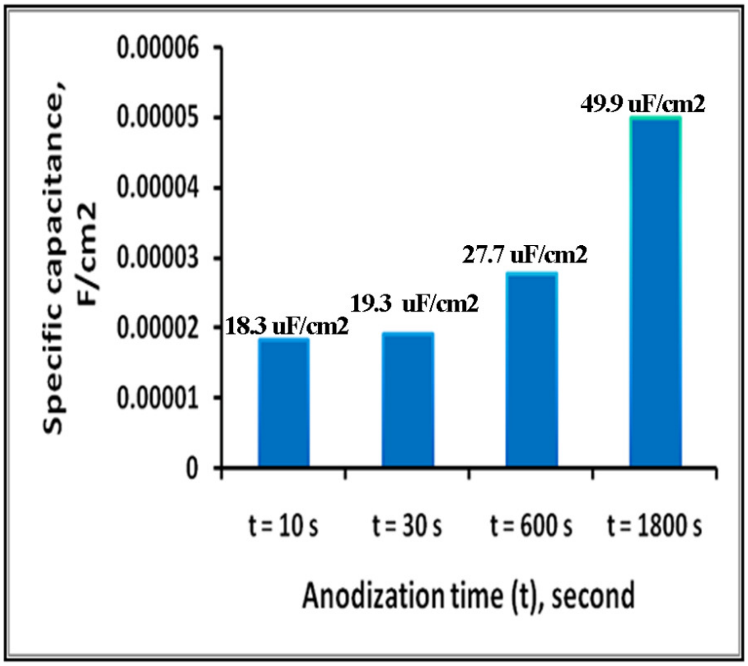

Figure4.20 Specific capacitance of anodized titania nanotubes in 1 M Na_2SO_4 for different anodization times.

It can be seen in all CV curves that the size of CVs will become lower when approaching a more positive applied potential. This phenomenon will be discussed in the next sections.

$$C = \int_{E_1}^{E_2} i(E)dE/2(E_2 - E_1)v \tag{4.5}$$

Specific capacitance from the CV curves can be calculated using equation (4.5) where E_1 and E_2 are the cut-off potentials in the cyclic voltammograms, i(E) is the instantaneous current, $\int_{E_1}^{E_2} i(E)dE$ is the total voltammetric charge obtained by integration of the positive and negative sweeps from the cyclic voltammograms, and (E_2–E_1) is the width of the potential window. With calculations using 5 mV s^{-1} and normalized 1 cm^2 surface area as an example, the specific capacitance for 10 s, 30 s, 600 s and 1800 s of anodized titania surface are 18.3 µF cm^{-2}, 19.3 µF cm^{-2}, 27.7 µF cm^{-2} and 49.9 µF cm^{-2} respectively, as shown in Figure 4.20.

These results clearly show the effect of nanotubular structure on the enhancement of specific capacitance of the titania materials. This titania nanotube arrays which were grown directly on conductive Ti substrate provides an intrinsically high surface area of these nanostructured materials and ensures the high utilization of electrode materials with higher specific capacitance.

4.3 The third project : Supercapacitance of ammonia annealed bamboo-type titania nanotubes

4.3.1 FESEM

This section deals with bamboo-type nanotubes obtained by anodizing Ti in glycerol consisting of 0.5 wt% NH_4F and 25 wt% of DI water. This anodization is done at 45 V applied voltage at room temperature. Figure 4.21 represents the FESEM micrographs for titania nanotubes with different anodization times: 1 hour (sample A, Figure4.21a) and 5 hours (sample B, Figure4.21b).

Table 4.5 presents a summary of the measurements performed on these micrographs. It is apparent that the extended anodization time increased the nanotube length by 142%, from 413 nm (sample A) to 1000 nm (sample B), while the stratified layer spacing decreased by 30.8%, from 26 nm to 18 nm. Anodization of titanium in organic electrolytes such as glycerol could lead to increase nanotubes layer thickness (Macak et al., 2005).

This results in an increased aspect ratio, a higher specific surface area and a higher electrochemical capacitance. It is worth noting that a ring structure has formed in sample B due to the stratified layer detachment from the tube opening body. This effect will increase the porosity and produce a larger electro-active surface area of the nanotubes for easy diffusion of the electrolyte (Song and Schmuki, 2010).

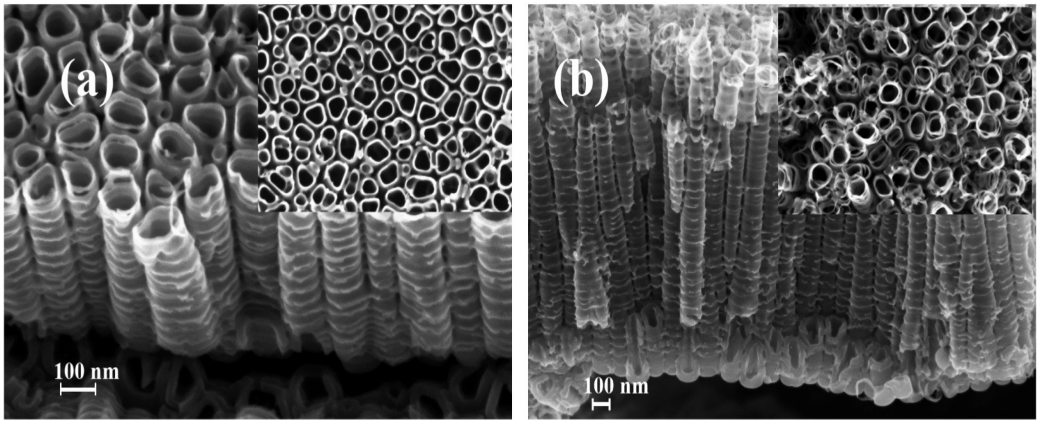

Figure4.21 Side-view FESEM micrographs of anodic titania nanotube array for different anodization times: (a) Sample A (1 hour) and (b) Sample B (5 hours).

Table 4.5 Nanotube structure measurement of both samples based on FESEM micrographs

Structure Measurements (nm)	**Anodization time**		**Change (%)**
	Sample A	**Sample B**	
Tube Length	413	1000	142
Tube opening	90	107	18
Tube bottom	150	140	-6.6
Wall spacing	22	14	-36.4
Stratification layer	26	18	-30.8

4.3.2 XRD

Figure 4.22 shows the XRD patterns of the titania nanotube arrays annealed in O_2 at 500°C for 2.5 hours (sample B) and the titania nanotube arrays annealed in an NH_3 atmosphere (sample C) with the same setting as those of sample B. The diffraction peaks can be indexed as the anatase crystalline phase, but the rutile phase was only detected in the O_2 annealed sample (sample B). It is widely reported that annealing at more than 500°C in O_2 will convert the anatase phase to the rutile phase, while annealing above 650°C will result in tube collapse (Roy et al., 2011; Albu et al., 2008; Roy et al., 2010; Zhang et al., 2010). Nitridation below 550°C does not change the titaniacrystalline phase, as suggested by Zhang et al., (2008). This explains the absence of the rutile phase in the sample annealed in NH_3. The XPS analysis also did not show the presence of any nitrogen peak, which supports the XRD results.

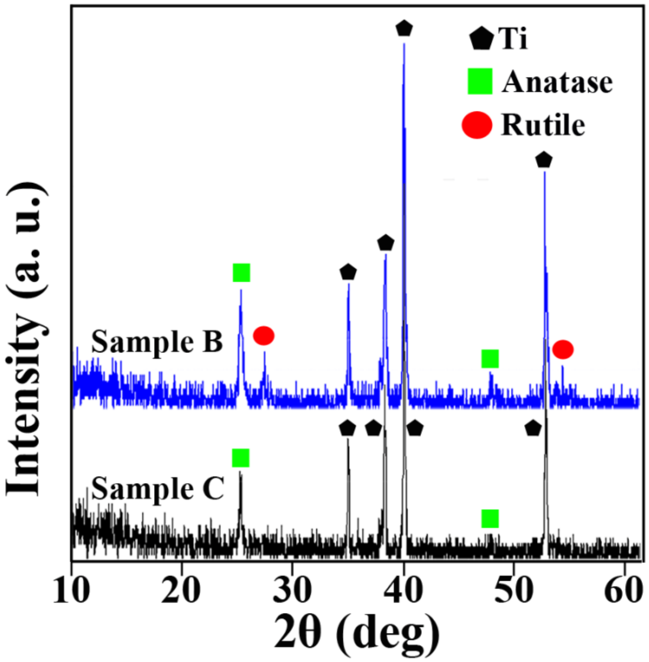

Figure4.22 XRD pattern of anodic titania nanotube arrays after annealing at 500°C for 2.5 hours. Sample B (annealed in O_2) and sample C (annealed in NH_3).

4.3.3 XPS

To further confirm the identity of the oxide film, an XPS analysis is used to identify the Ti oxidation states of this film. All the binding energies obtained in the XPS analysis are calibrated using the C 1s peak at binding energy of 284.5 eV as the reference. Figure 4.23 is the overlaid spectra of sample B and sample C. The Ti 2p spectra for both samples show the presence of a main doublet composed of two symmetrical peaks with binding energies of 458.48 eV (Ti $2p_{3/2}$) and 464.15 eV (Ti $2p_{1/2}$), which are attributed to the Ti-O bond (Xiao et al., 2010). However, the sample annealed in NH_3 (sample C) shows a peak at binding energy of 457.7 eV, which suggests that the reduction of Ti^{4+} to lower valence Ti^{3+} may have occurred during NH_3 annealing.

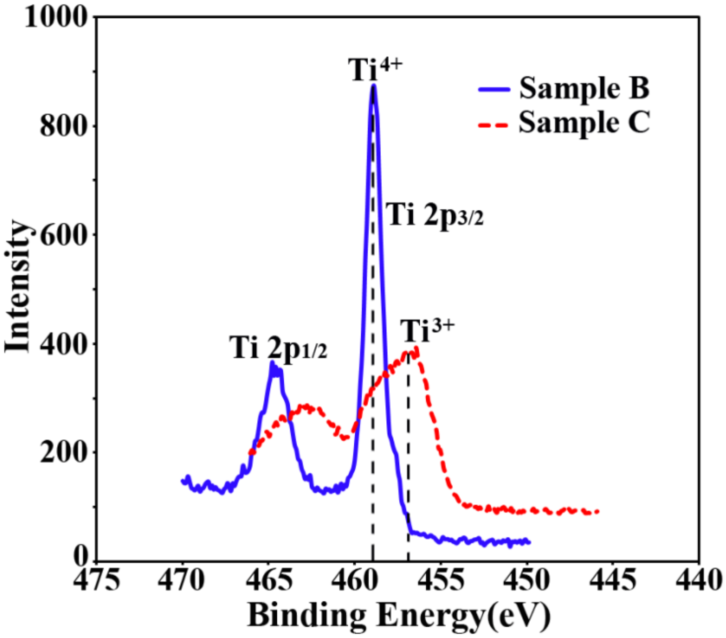

Figure4.23 XPS Ti 2p spectrum after annealing at 500°C for 2.5 hours. Sample B (annealed in O_2) and sample C (annealed in NH_3).

According to the literature (Zhang et al., 2010; Xiao et al., 2010; Li et al., 2006), this peak is attributed to titanium with oxidation states between +3 and +4, which correlate with the titanium in a distorted lattice located between the titania and TiN phases. However, the XPS results did not detect the presence of nitrogen; thus, nitridation did not occur below 500°C. This phenomenon indicates a synchronous increase in the surface electron density for Ti and O atoms. Considering that the N binding energy represents the same change as those of Ti and O, some authors proposed that the electron-donating effect may originate elsewhere, instead of N, O, and Ti atoms (Zhang et al., 2010; Tarlov and Evans, 1987). In this work, the electron donating effect must come from the annealing with NH_3, which is also a reducing agent.

4.3.4 Cyclic voltammetry

The electrochemical performance of the titania nanotubes was elucidated by cyclic voltammetry in 1 M Na_2SO_4 for samples A (Figure 4.24a) and B (Figure 4.24b) and in 1 M H_2SO_4 for sample C (Figure 4.24c). From the figures, samples annealed in O_2 (samples A and B) exhibit almost rectangular and symmetrical CV curves, as expected from an ideal electrochemical double layer capacitor, while sample C annealed in NH_3 shows redox peaks, which are due to redox reactions occurring on the surface.

For samples A and B, the shape of the CV curves are symmetrical with the increase of the scan rate, which suggests excellent reversibility (Salari et al., 2011). Sample C shows pseudo-capacitance behaviour, which can be observed by the peak shift to more anodic and cathodic potentials (Kim et al., 2010). This redox reaction is attributed to the oxidation-reduction of the Ti^{3+} and Ti^{4+} and is additional proof that the reduction from Ti^{4+} to Ti^{3+} has taken place during the process of annealing in the NH_3 atmosphere.

Furthermore, the peak current for all samples increased with the increase of the scan rate from 5 mV s^{-1} to 100 mV s^{-1}, which shows the good reversibility of fast charge-discharge response (Kim et al., 2009). The specific capacitance (C) for samples

A and B can be calculated by equation (4.6), where I is the average current (mA), V is the scan rate (mV s^{-1}) and A is the active area (1 cm^2).

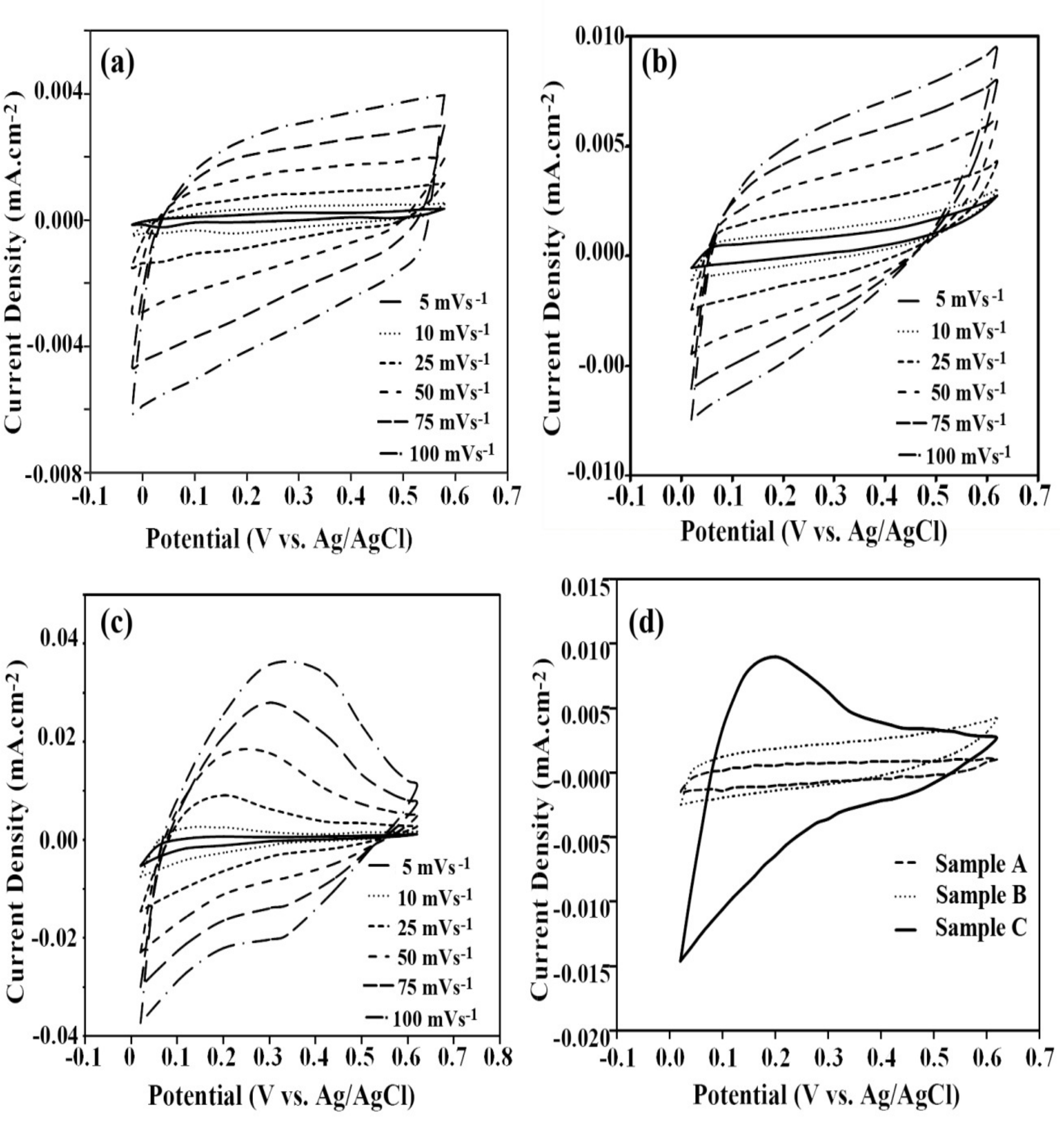

Figure 4.24 The (a) CVs for sample A in 1 M Na_2SO_4, (b) CVs for sample B in 1 M Na_2SO_4, (c) CVs for sample C in 1 M H_2SO_4, and (d) overlaid CVs for samples A, B and C at a scan rate of 5 mV s^{-1}.

$$C=I/VxA \tag{4.6}$$

Specific capacitance for sample C was calculated using equation (4.5) since the CV curve is not a mirror symmetry where E_1, E_2 are the cut-off potentials in cyclic voltammetry, i(E) is the instantaneous current, $\int_{E_1}^{E_2} i(E)dE$ is the total voltammetric charge obtained by integration of the positive and negative sweep in cyclic voltammograms. $(E_2 - E_1)$ is the potential window width.

The values for specific capacitance calculated for sample A, sample B and sample C using a scan rate of 5 mVs^{-1} are 16 $\mu F\ cm^{-2}$, 52 $\mu F\ cm^{-2}$ and 118 $\mu F\ cm^{-2}$, respectively. The specific capacitance of sample B is higher than sample A due to the larger aspect ratio and specific surface area, as shown by the FESEM results. A higher anodization time will not only increase the tube length but also decrease the stratified layer on the tube wall surface of this bamboo-type titania nanotube, therefore resulting in a larger aspect ratio.

Longer nanotubular structures also help in the transportation of ions and facilitate the charging of the double layer (Kim et al., 2009). Titania nanotube annealing at 500°C in NH_3 also enhanced the specific capacitance as shown by sample C. However, the improved electrochemical capacitance for this sample is not from nitrogen doping of titania nanotubes but from the anatase phase, the oxygen vacancies and the non-stoichiometry from the reduction of Ti^{4+} to Ti^{3+}, as shown by the XRD and XPS results. The annealing temperature used in this study is not sufficient to promote the nitridation process.

4.3.5 Electrochemical impedance spectroscopy

EIS analysis has been carried out to further investigate the interfacial ion diffusion and charge transfer process of titania nanotubes electrode/electrolytes system. Figure 4.25(c) and 4.25(d) show the Nyquist diagrams of titania nanotube electrodes in 1 M Na_2SO_4 and 1 M H_2SO_4 electrolytic media. Complex impedance measurement is conducted with a frequency range of 0.01 Hz to 100 kHz under a constant potential of 0 V vs. Ag|AgCl and ac-voltage amplitude of 5mV.

The EIS for the sample in 1 M Na_2SO_4 as shown in Figure 4.25(c) shows electrical double layer characteristics with 45^o impedance line. The non-vertical slope of the low frequency impedance results from the surface roughness of titania nanotube porous electrode. The EIS for sample in 1 M H_2SO_4 as shown in Figure 4.25(d) shows that the pseudocapacitance characteristics exhibits depressed semicircles at the high frequency region and can be ascribed to a resistance to charge transfer due to faradaic reactions taking place at the electrodes. At the low frequency region for sample in 1 M H_2SO_4, a straight line can be ascribed to Warburg impedance related to the ion diffusion of electrolyte within the pores of electrode. From EIS observations above, it can be concluded that charge storage activities of ammonia annealed titania nanotubes differ based on electrolyte used. The effect of ammonia annealing is more pronounced when the electrode is studied in 1 M H_2SO_4 compared to 1 M Na_2SO_4.

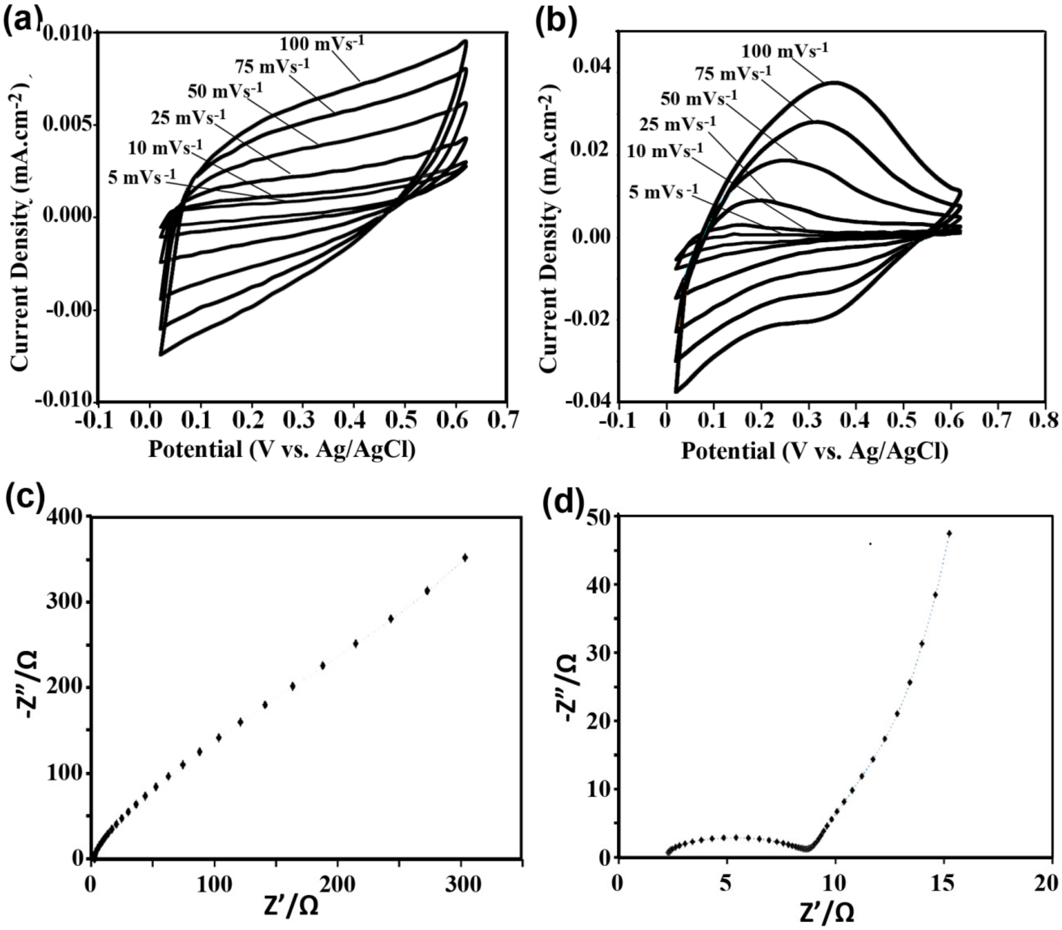

Figure 4.25 (a) CVs for NH_3 annealed titania nanotubes in 1 M Na_2SO_4, (b) CVs for NH_3 annealed titania nanotubes in 1 M H_2SO_4, (c) EIS for NH_3 annealed titania nanotubes in 1 M Na_2SO_4, and (d) EIS for NH_3 annealed titania nanotubes in 1 M H_2SO_4.

4.3.6 Galvanostatic charge-discharge testing

Figure 4.26 shows charge-discharge curves for sample in 1 M Na_2SO_4 and sample in 1 M H_2SO_4 using same applied potential study in cyclic voltammetry from 0 volt to 0.6 volts and applied current of 2 microampere. Charge-discharge test for sample in 1 M Na_2SO_4 shows identical behavior with its cyclic voltammetry indicates that the electrical double layer capacitance is based on charge separation at interface. Charging and discharging curves is mirror-like implying that the charge-discharge process is reversible.

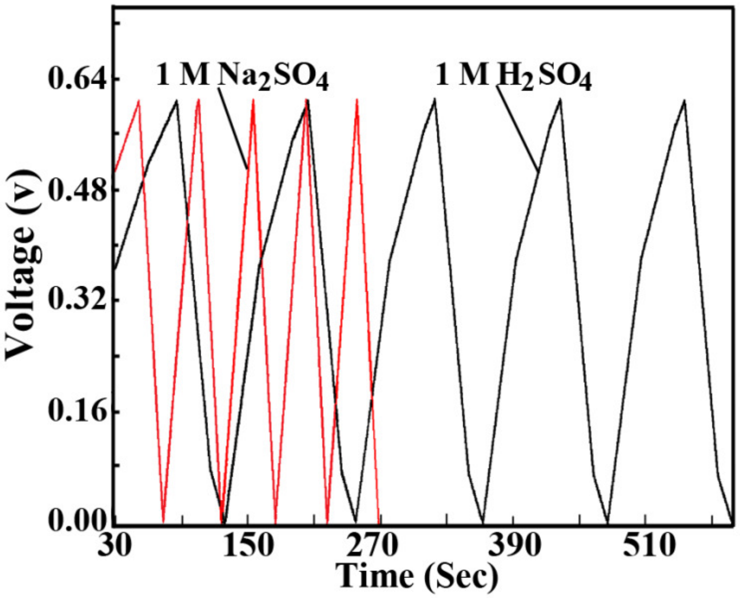

Figure4.26 : Charge-discharge curves for NH_3 annealed titania nanotubes in 1 M Na_2SO_4 and in 1 M H_2SO_4.

In contrast to the sample in 1 M Na_2SO_4, it was observed that the charge and discharge curves for sample in 1 M H_2SO_4 is not identical with a slight non-linear curve, which typically indicates a reaction in the charging process. The time taken to charge from 0 V to 0.6 V and to discharge from 0.6 V to 0 V for sample in 1 M H_2SO_4 is also longer than the sample in 1 M Na_2SO_4. This shows that the sample in H_2SO_4 has a larger specific capacitance than the sample in 1 M Na_2SO_4. The specific capacitance (C) of the electrodes was calculated form equation (4.8):

$$C = C/A = I/[(dV/dt) \times A] \tag{4.8}$$

where I is the charge-discharge current, dV/dt is the scan rate and A is the surface area of the working electrode. The specific capacitance of the sample in 1 M Na_2SO_4 is 52 µF cm^{-2} and in 1 M H_2SO_4 is 118 µF cm^{-2}. The specific capacitance values of titania nanotubes in 1 M H_2SO_4 is two orders of magnitude higher than the titania nanotubes in 1 M Na_2SO_4. Annealing in ammonia has changed surface properties of titania nanotubes by creating oxygen vacancies and reduction of Ti^{4+} to Ti^{3+}, thus increasing its electrical conductivity.

Crystallinity change of the titania nanotubes from amorphous to anatase phase has contributed to a change in electrical conductivity of the annealed surface. In addition, larger specific capacitance can only be shown in 1 M H_2SO_4, a redox type electrolyte due to fast electron transfer at the electrolyte/electrode interfaces. Proton intercalation also may contribute to higher specific capacitance of the sample in H_2SO_4. During the reverse potential scan to more negative values gave rise to a cathodic process. This process was consistent with the reduction of Ti^{4+} sites in the TiO_2 [32]. Therefore, it corresponds to reversible conduction-band filling accompanied by proton insertion [22] (Eq. (1)). This process is schematically shown below:

$$Ti^{4+}(TiO_2) + e^-(Ti) + H^+(aq) \rightarrow Ti^{3+}(TiO_2) + H^+(TiO_2)$$

Moreover, as proposed in the literature, the titania nanotubular channels, as a form of open porosity, facilitate the ionic mass transfer through mesopores by providing pathways throughwhich the dynamic sheath of solvent molecules, the salvation shell, can easily pass (Salari et al., 2011; Santiago et al., 2006; Santiago et al., 2008; Roy et al., 2011). The higher ionic mass transfer consequently results in higher capacitance values.

4.4 The fourth project: Enhancing electrochemical capacitance of anodized titania nanotubes using Box-Behnken design and Response Surface Method (RSM)

4.4.1 Galvanostatic charge-discharge testing

The same applied potential and current density were used for all the measurements of the charge-discharge test. Figure 4.27 shows the charge-discharge profile for the titaniananotubes from 0 to 0.6 V with a current density of 20 µA. The specific capacitance is calculated according to the following equation:

$$C = \frac{I\Delta t}{A\Delta V} \tag{4.9}$$

where C (F cm^{-2}) is the specific capacitance, I (mA) is the discharge current, A (cm^2) is the nominal surface area, ΔV (V) and Δt (s) represent the potential drop during discharge and total discharge time respectively. The preliminary study of titania nanotubes using initial anodization parameters of potential (45 V), time (60 min) and NH_4F concentration (0.5 wt %) gives specific capacitance of 105 µF cm^{-2} for a discharge time of 31.5 s.

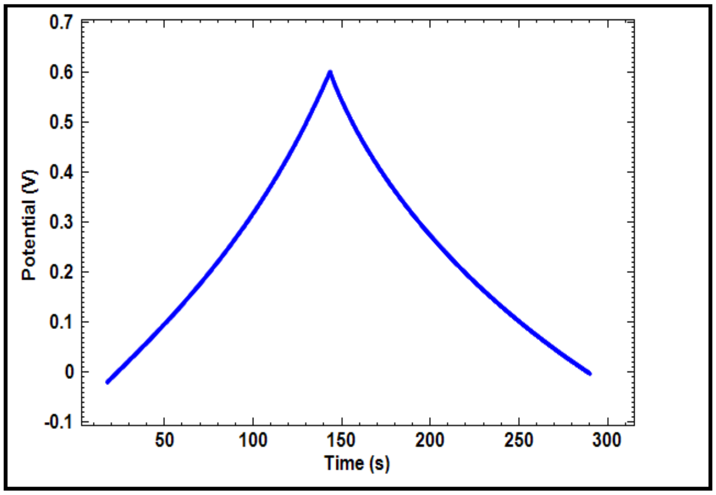

Figure 4.27 Charge-discharge curve of anodic titania nanotubes in 1 M Na_2SO_4 for preliminary study using anodization time, voltage and NH_4F concentration of 60 min, 45 V and 0.5 wt%, respectively.

4.4.2 Model build-up and ANOVA analysis

Box–Behnken statistical experiment design and the RSM were used to investigate the effects of the three independent variables on the response functions and to determine the optimal conditions to maximize the titania nanotube discharge time in 1 M Na_2SO_4. The experiment design consisted of 15 experiment runs, using three anodization factors (anodization time, applied potential and ammonium fluoride concentration) as shown in Table 4.6 with all the factors having a minimum, centre

Table 4.6 The actual and coded level of factors for Box-Behnken design

Factors	Range and levels		
Coded level	1	0	-1
Time (min)	40	80	120
Voltage (V)	30	40	50
NH_4F concentration (wt%)	0.3	0.4	0.5

point and maximum level. The optimization procedure involves evaluating the response of the statistically designed combinations, estimating the coefficients by fitting the experimental data to the response functions, predicting the response of the fitted model and checking the adequacy of the model.

Table 4.7 Box-Behnken design and experimental results

Order	Run	Time (min)	Voltage (V)	NH_4F (wt%)	Discharge Time (min)
1	7	40	30	0.4	11.7
2	5	120	30	0.4	21.1
3	1	40	50	0.4	29.7
4	15	120	50	0.4	36.2
5	6	40	40	0.3	26.6
6	8	120	40	0.3	31.6
7	10	40	40	0.5	20.1
8	11	120	40	0.5	40.8
9	13	80	30	0.3	11.8
10	3	80	50	0.3	10.5
11	9	80	30	0.5	31.4
12	2	80	50	0.5	33.1
13	4	80	40	0.4	42.5
14	14	80	40	0.4	41.3
15	12	80	40	0.4	43.2

The application of RSM offers an empirical relationship between the response function and the independent variables. The mathematical relationship between the response function (Y) and the independent variables (X) can be approximated by a quadratic polynomial equation as follows:

$$Y = b_o + b_1X_1 + b_2X_2 + b_3X_3 + b_{12}X_1X_2 + b_{13}X_1X_3 + b_{23}X_2X_3 + b_{11}X_{21} + b_{22}X_{22} + b_{33}X_2 \quad (4.10)$$

Table 4.7 shows a design matrix for Box-Behnken design and the discharge time as the response function (Y). From the table, Run 15 has the highest discharge time (43.2 minute) and Run 10 has the lowest discharge time (10.5 minute). FESEM is used to examine the surface morphology of the highest and the lowest discharge time value. From the Figure 4.28, the highest discharge time sample shows highly ordered titania nanotubes structure while sample with the lowest discharge time has bundle-type titania nanotubes. This bundle-type titania nanotubes reduced specific surface area, as a result lower specific capacitance was obtained.

The correlation of the response function and different dependent variables were determined by Design-expert (Stat-Ease) regression software. The equations below illustrates the relationship of the three variables and the response function (Y).

$$Y = 42.33 + 2.31A + 4.19B + 8.50C - 0.72AB + 3.99AC + 0.75BC - 4.79A^2 - 12.87B^2 - 7.76C^2 \tag{4.11}$$

On the basis of the coefficients in Eqs. (4.10) and (4.11), it can be said that ammonium flouride concentration (C) has a more profound effect on discharge time of anodic titania nanotubes in 1 M Na_2SO_4. The combination of ammonium flouride (C) and anodization time (A) is also greater than the other two factor combinations. It is reported (Liu et al., 2011) that the anodization time and ammonium flouride concentration will define the tube length and improve aspect ratio, thus increasing discharge time and specific capacitance.

The analysis of variance (ANOVA) is shown in Table 4.8. The ANOVA of regression model demonstrates that the model in Eqs. (4.10) and (4.11) are significant.

Table 4.8 Analysis of variance for model of anodic titania nanotubes discharge time

Source	Sum of Square	dF	Mean Square	F Value	p-value Prob. > F
Model	1651.2C	9	183.47	4.79	0.0495
A-Time	42.65	1	42.65	1.11	0.3394
B-Voltage	140.37	1	140.37	3.67	0.1136
C-NH_4F	577.34	1	577.34	15.09	0.0116
AB	2.10	1	2.10	0.05	0.824
AC	63.61	1	63.61	1.66	0.2537
BC	2.24	1	2.24	0.06	0.8186
A^2	84.59	1	84.59	2.21	0.1972
B^2	611.75	1	611.75	15.99	0.0103
C^2	222.29	1	222.29	5.81	0.0609
Residual	191.33	5	38.27		
Lack of Fit	189.49	3	63.16	68.41	0.0144
Pure Error	1.85	2	0.92		
Cor Total	1842.54	14			

R^2 = 0.8962, Adj.R^2 = 0.7092, Pred.R^2 = -0.6477, and C.V. = 21.5 %

The goodness of fit of the model can be checked by the determination coefficient (R^2). The value of R^2 (0.896) for the regression model close to 1 indicates a high degree of correlation between the observed and predicted value. This means the model can be expected to explain about 89% of variation in the response. The lack-of-fit measures the failure of the model to represent data in the experimental domain at points which are not included in the regression. The non-significant value of lack-of-fit (>0.05) revealed that the quadratic model is statistically significant for the response. There is only a 4.95% chance that a model F-value this large could occur due to noise. In this case, ammonium flouride concentration (C) is a significant model term. The lack of fit F-value of 68.41 also implies that the lack of fit is significant. There is only a 1.44% chance that a lack of fit F-value this large could occur due to noise.

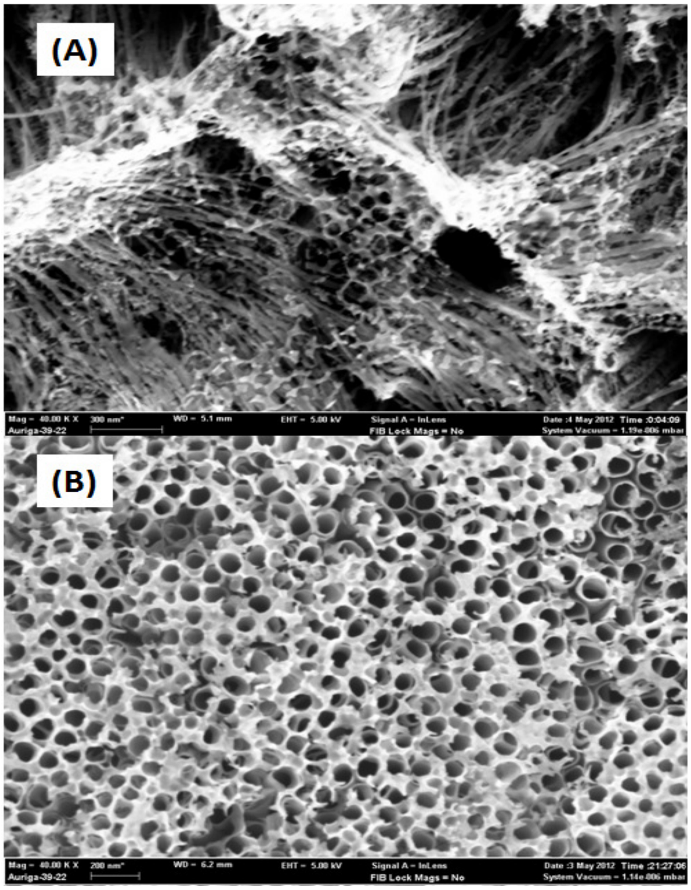

Figure 4.28 FESEM micrographs of anodized titania nanotubes for different specific electrochemical capacitance value (a) The lowest and (b) The highest

4.4.3 Effect of parameters, optimum condition and verification

Figure 4.29 shows the contour plot and 3-D response surface plots for the relationship between anodization time (A), potential (B) and ammonium flouride concentration (C) on the discharge time of anodic titania nanotubes in 1 M Na_2SO_4.

The numerical optimizationfrom software calculation was chosen in order to find the specific point that maximizes the desirability function. The desired goal was selected by adjusting the weight or importance that might alter the characteristics of a goal. The main objective of optimization was to maximize the discharge time by recalculating all responsible factors using desirability functions.

The optimized anodization parameters were 97.78 min (anodization time), 39.11 V (applied voltage) and 0.42 wt % (ammonium flouride concentration) and resulted in a maximum discharge time of 43.69 s. Using equation (4.9), the specific capacitance obtained after optimization is 145.6 $\mu F\ cm^{-2}$.

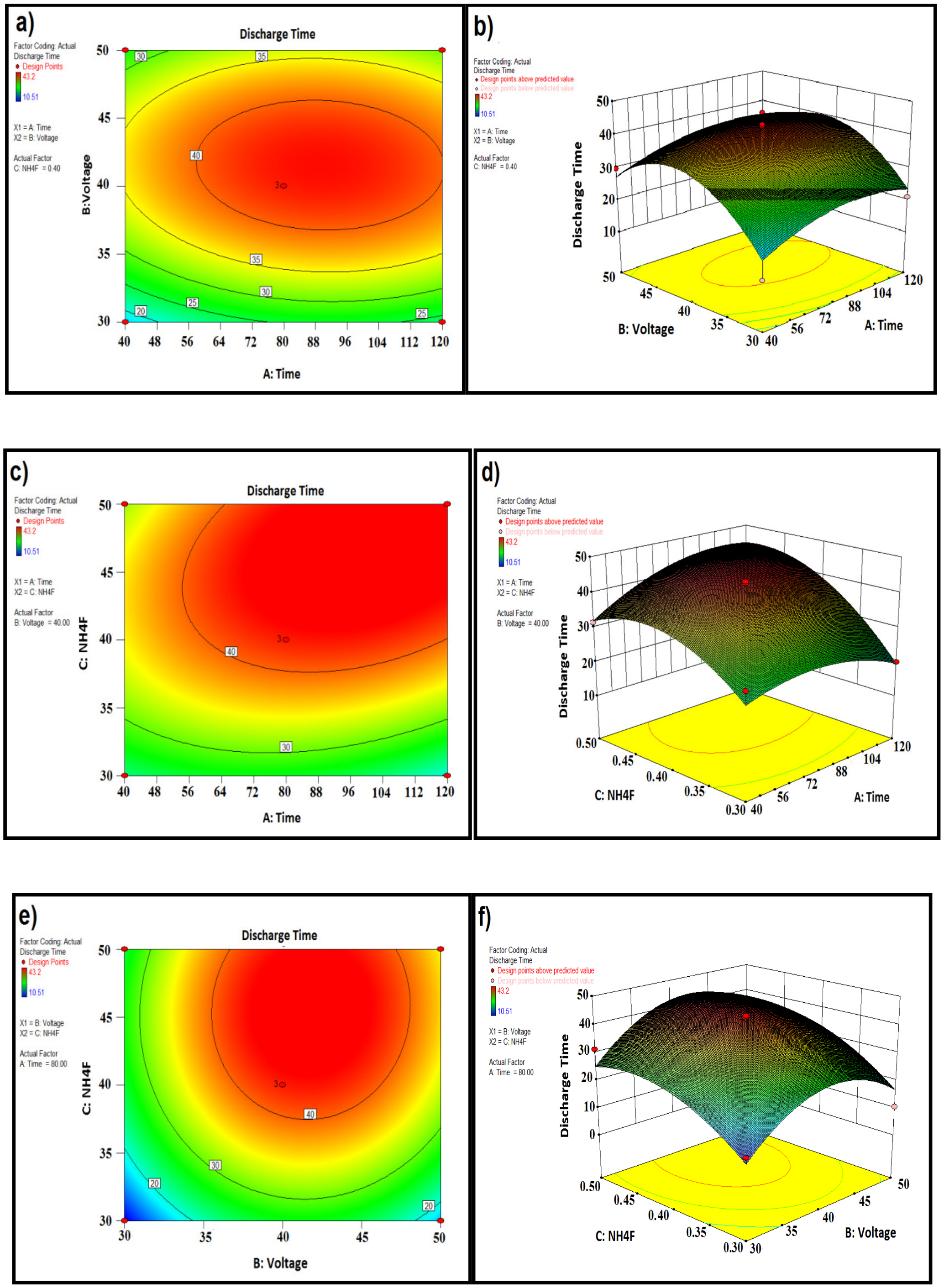

Figure 4.29 Contour plot and 3D response surface graphs for anodic titania nanotube discharge time versus anodization paramater (a,b) discharge time versus time and applied voltage (c,d) discharge time versus time and ammonium fluoride concentration (e,f) discharge time versus ammonium fluoride concentration and applied voltage.

4.5 The fifth project : Enhancing electrochemical capacitance of anodized titania nanotubes using EMIM hydrogensulfate ionic liquid as electrolyte

4.5.1 Cyclic voltammetry

In order to increase electrochemical capacitance and widen the voltage operational window, 1-ethyl-3-methyl imidazolium (EMIM) hydrogensulfate ionic liquid is used as an electrolyte. Dissociated and high concentrations of cations and anions make up the composition of ionic liquids, and can be used alone in supercapacitor as an electrolyte where it acts as both the solute and solvent. Ionic liquid is stable and non-volatile even at high operating voltages (>3.5 V) without decomposition. Furthermore, the ionic liquid is non-flammable, which is an attribute that will improve the safety of the EDLCs. Figure 4.30 shows the anion and cation structures of EMIM hydrogen sulfate ionic liquid.

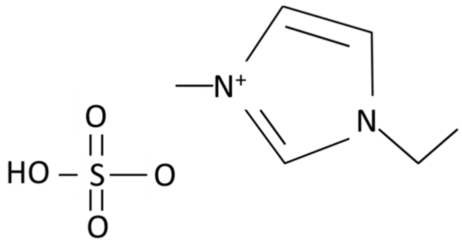

Figure 4.30 Anion and cation structure of EMIM hydrogen sulfate ionic liquid

The electrochemical performance of the titania nanotubes was elucidated by cyclic voltammetry of EMIM hydrogensulfate ionic liquid at room temperature as shown in Figure 4.31 (a) and Figure 4.31 (b).

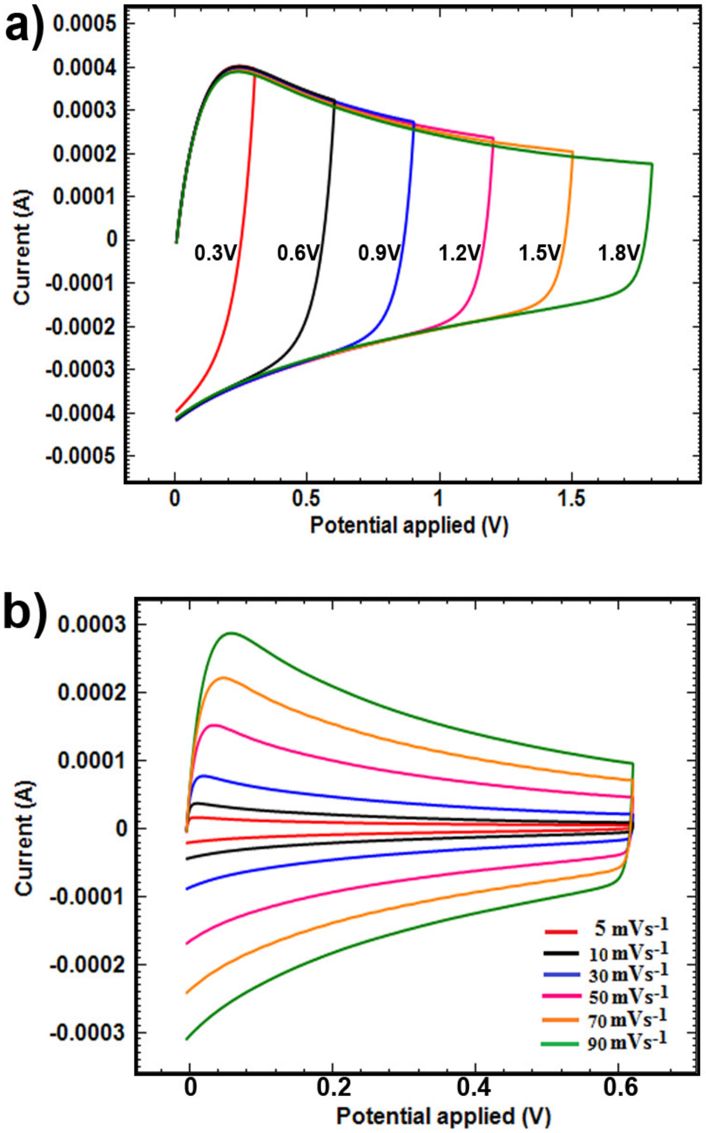

Figure 4.31 Cyclic voltammograms of anodized titania nanotubes in EMIM hydrogensulfate (a) with different operating voltages from 0 V to 1.8 V (b) with different scan rates from 5 mVs^{-1} to 90 mVs^{-1}.

Figure 4.31(a) shows CV plots of anodized titania nanotubes in EMIM hydrogensulfate with different operating voltages from 0 V to 1.8 V at a scan rate of 5 mVs^{-1}. From the figure, the CV curve obtained is identical with the CV obtained in aqueous 1 M Na_2SO_4 as presented in the previous Figure 4.19b. The CV retains the symmetrical rectangular shape for each operating voltage suggestive of typically pure electrical double layer behaviour of the device. No redox peaks are observed in each operating voltage. However, it is evident that a peak curve occurs when the current density reaches a maximum value at around 0.2 V and decreases for larger potential due to the saturation of surface anion concentration at the electrode surface. This phenomenon is not a surface redox reaction and usually found in large concentrations of electrolyte such as in EMIM hydrogensulfate ionic liquid (Wang and Pilon, 2012; Kornyshev et al., 2011).

The experimental CV data plotted in Figure 4.31(b) with scan rates from 5 mVs^{-1} to 90 mVs^{-1} shows that the CVs have nearly symmetric rectangular shape for all scan rates. This suggests that anodized titania nanotubes hold high charge storages and high rate capabilities in EMIM hydrogensulfate ionic liquid. This can be attributed to the fact that a fast change in the surface potential resulted in a large local electric field and thus a large current density (Wang and Pilon, 2012). This also confirms the formation of efficient electrical double layer and fast charge propagations within the electrodes (Liu et al. 2011). Based on these results, ionic liquid can be used to widen the voltage limitation of aqueous electrolyte for high power supercapacitor application.

4.5.2 Galvanostatic charge-discharge testing

Figure 4.32 shows galvanostatic charge-discharge testing for anodized titania nanotubes in EMIM hydrogensulfate ionic liquid which was recorded from 0 V to 0.6 V using current density from 4 μA cm^{-2} to 10 μA cm^{-2}. It is evident that the charge-discharge results show a triangular shape for all current densities which represents good charge-discharge reversibility, efficient charge-discharge rates and perfect electrical double layer capacitance (Salari et al., 2011). Moreover, the discharge curve consists of two sections: a sharp decrease of potential followed by a slow drop of potential which is due to the IR drop at the titania nanotube interface and charge redistribution during discharge process respectively (Kang et al., 2012; Niu et al., 2004). By using the equation (4.9), the specific capacitance for this anodized titania nanotubes in EMIM hydrogensulfate is 1.58 mF cm^{-2} for a current density of 10 µA cm^{-2}.

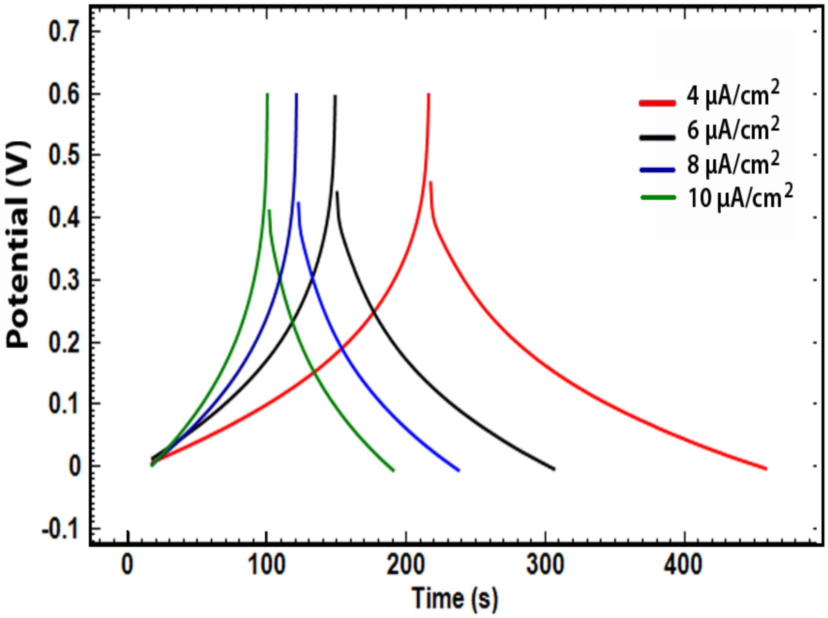

Figure 4.32 Galvanostatic charge-discharge curves of anodized titania nanotubes in EMIM hydrogensulfate using different current densities from 4 µA cm^{-2} to 10 µA cm^{-2}.

The higher specific capacitance of the titania nanotubes in EMIM hydrogensulfate compared with the ones in Na_2SO_4 is caused by a few reasons. First, ionic liquid contains high concentration of cations and anions that are involved in charge storage activities, thus providing a greater specific capacitance. Second, the charge storage mechanism of the ionic liquid is different compared to that in aqueous electrolyte. Charge storage mechanism of titania nanotubes in Na_2SO_4 is explained by using classical electrical double layer principles such as Gouy-Chapman or Stern model while the charge storage mechanism of the electrode interface in ionic liquid electrolyte such as in EMIM hydrogensulfate ionic liquid is still debatable. Kornyshev et al. (2011) has explained the storage mechanism of the latter using the overscreening and crowding theory as shown in Figure 4.33(a) and Figure 4.33(b).

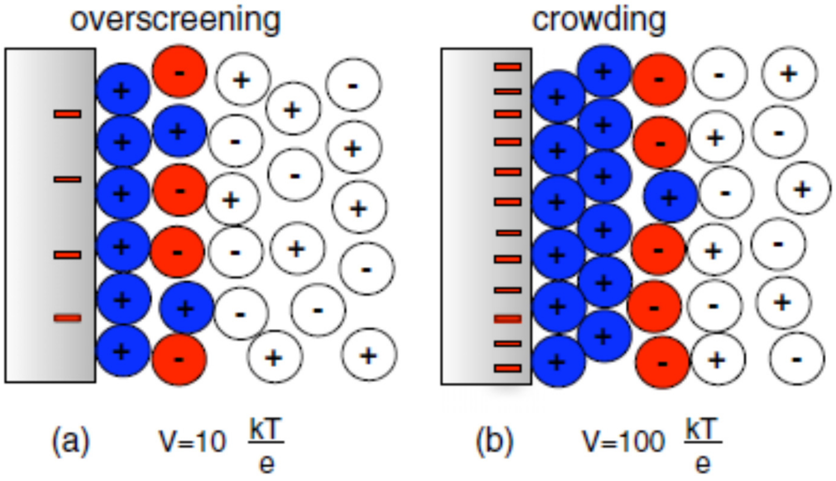

Figure 4.33 Ionic liquid double layer framework at electrode interface (a) overscreening stage (b) crowding stage

In this theory, at a low and moderate voltage, a monolayer of counterions overscreens the surface charge, where it is rectified by an overabundance of second monolayer coions. The counterion crowding spreads across two monolayers and controls overcrowding at a high voltage and thus, causes an overabundance of coions in the third monolayer. The diffuse double layer made up of colored ions is more condensed compared to the quasineutral bulk liquid made up of white ions, due to the nature of electrostriction. This stacking double layer explains the greater specific capacitance offered by EMIM hydrogensulfate ionic liquid.

4.6 The sixth project : Influence of flat-band potential on semiconducting properties of anodized titania nanotubes

4.6.1 Cyclic voltammetry

All the obtained CV plots for the titania nanotubes so far show identical shapes where the more negative area is always larger than the positive area. This section will discuss this characteristic in great detail. Figure 4.34 shows the cyclic voltammogram obtained in water at pH 2 (0.01 M H_2SO_4) using the scan rates from 5 mV s^{-1} to 30 mV s^{-1}. The scan was done separately from 0 V to 0.6 V and from 0 V to -0.6 V and both scans are plotted in the same graph.

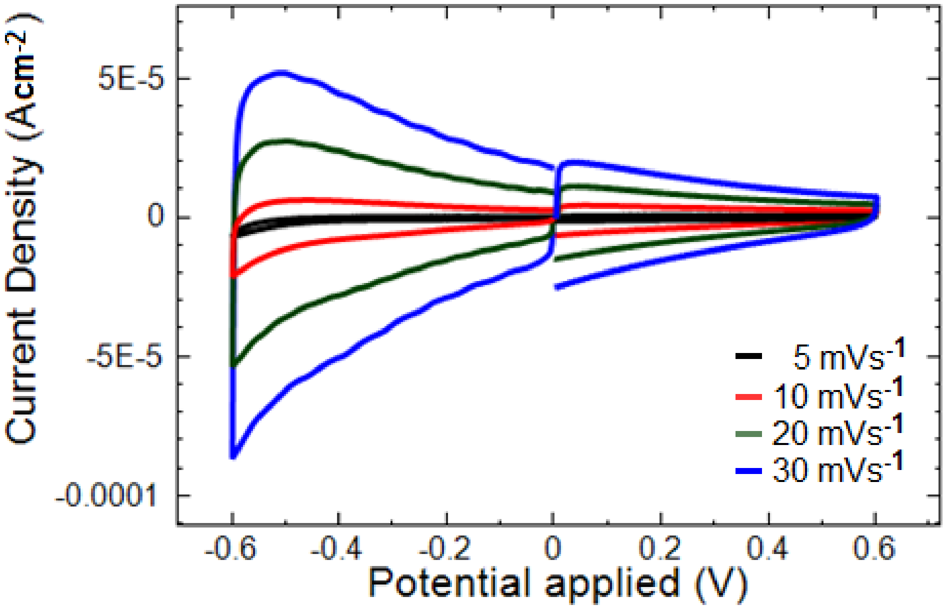

Figure 4.34 Cyclic voltammogram of titania nanotubes in water at pH 2 (0.01 M H_2SO_4) using the scan potential of 0 V to 0.6 V and 0 V to -0.6 V

From this graph, the cathodic current shows a behaviour that rises exponentially in all curves, either positive scan or negative scan. Once the return voltage is attained, a distinct anodic peak is revealed especially for 30 mV s^{-1} scan rate. At lower scan rate such as at 5 mV s^{-1}, formation of anodic peak is comparatively smaller. This behaviour shows the loss of current rules, although the collection of charge occurs at the titania nanotube surface. In these conditions, a large positive peak at a more electronegative potential is observed corresponding to discharge of the charge accumulated in the capacitor while the current was negative (Fabregat-Santiago et al., 2003). It is common knowledge that the linear increase of peak current with the scan rate occurs if it is controlled by the capacitive behaviour. At the increasing scan rate speed, the total charge participating in the process of polarization and the cycle increase reversibility is indicative of the higher influence that the charge accumulation mechanism has. The reason behind this higher influence of charge accumulation at cathodic area or at more negative potential was further analyzed by determination of flat-band potential using Mott-Schottky analysis.

4.6.2 Mott-Schottky analysis

The active surface area of the titania nanotubes produces higher current density values at more electronegative potentials compared to positive potentials. The comparatively small current density at more electropositive potentials for all the CV plots in Figure 4.34 can be justified by Mott-Schottky analysis to determine the flat band potential and charge carrier density of the titania nanotubes. Figure4.35 depicts Mott-Schottky curves in water at pH 2 (0.01 M H_2SO_4) using 100 Hz at potential scan from -0.6 V to 0.0 V. A positive slope of the plot confirms the excess of electron in titania nanotubes (n-type semiconductor). The Mott-Schottky plots are linear in the potential range from 0 to -0.15 V vs Ag/AgCl. The Mott-Schottky equation can be expressed as follows:

$$\frac{1}{c^2} = \left(\frac{2}{q\varepsilon\varepsilon_0 N_D}\right)\left(E - E_{fb} - \frac{kT}{q}\right) \tag{4.12}$$

where the symbols have the following meaning: C, the real capacity of the space charge layer; q, elementary charge (1.6 x 10^{-19} C); ε_0, vacuum permittivity (8.85 x 10^{-14} F cm^{-1}); ε, dielectric constant of the semiconductor; N_D, concentration of donors in the semiconductor; E, applied external bias; E_{fb}, flat-band potential; k, Boltzmann's

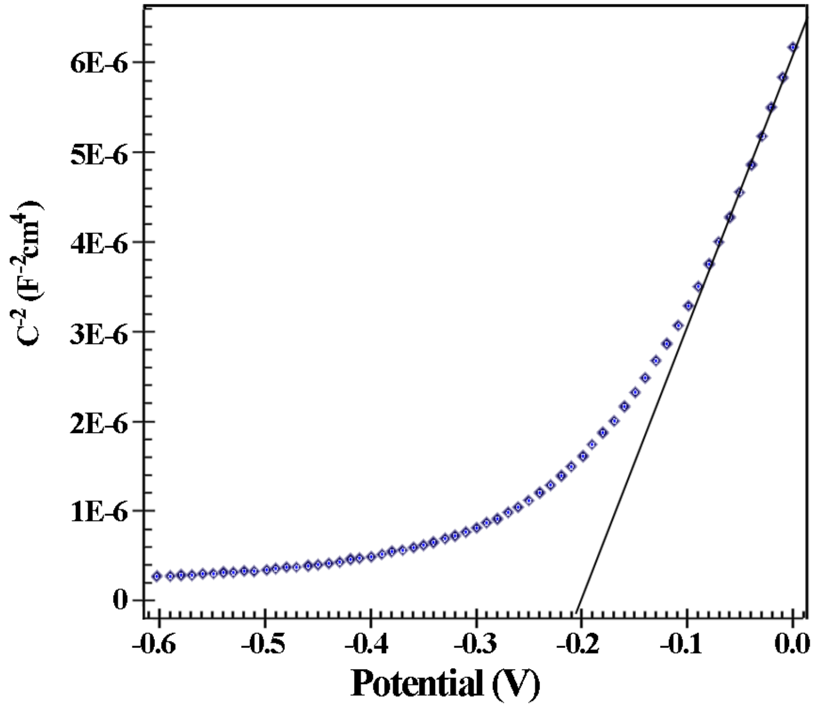

Figure4.35 Mott-Schottky plot for anodized titania nanotubes for the 1800 s sample in 1 M Na_2SO_4 using potential scan at frequency, f = 100 Hz

constant;T, absolute temperature. Thus, the flat band potential is given by the extrapolation to C^{-2}=0 from the C^{-2} vs E plots. The estimated flat band potential, E_{fb} at f=100 Hz is –0.21 V. Mott-Schottky conditions stipulate that the semiconductor electrode should be blocking at more positive potentials (Sakai et al., 2004; Munoz et al., 2007).

When the CV scan is done at a more negative potential approaching the flat band potential, conductivity of titania and its capacitance will exponentially increase. The capacitance increase is due to the unpinning of the Fermi level that occurs at potentials more negative than the flat-band potential allowing the Fermi level to approach the conduction band. More electrons are accumulated at the electrode surface, attracting counter ions and a higher electrochemical capacitance is obtained. As a result, larger CV is obtained at a more negative potential.

4.6.3 Electrochemical impedance spectroscopy

The influence of the flat-band potential on semiconducting properties of titania nanotubes were further analyzed using electrochemical impedance spectroscopy. Figure 4.36 and 4.37 show the Nyquist plot and Bode plot of titania nanotubes in water at pH 2 (0.01 M H_2SO_4) at different applied potentials, respectively. At an applied potential more positive than the flat-band potential such as 0 V (Figure 4.36a and 4.37a), non-ideal capacitive behaviour can be seen due to pore size distribution since each pore would have a different penetration depth depending on its dimensions. At negative potential such as -0.6 V, the titania nanotubes changed from blocking electrode to passing behaviour. To confirm this, the equivalent circuits of $R_1(R_2C_{SC})(R_3C_S)$ as shown in Figure 4.38 is used to fit the experimental data (Munoz et al., 2007).

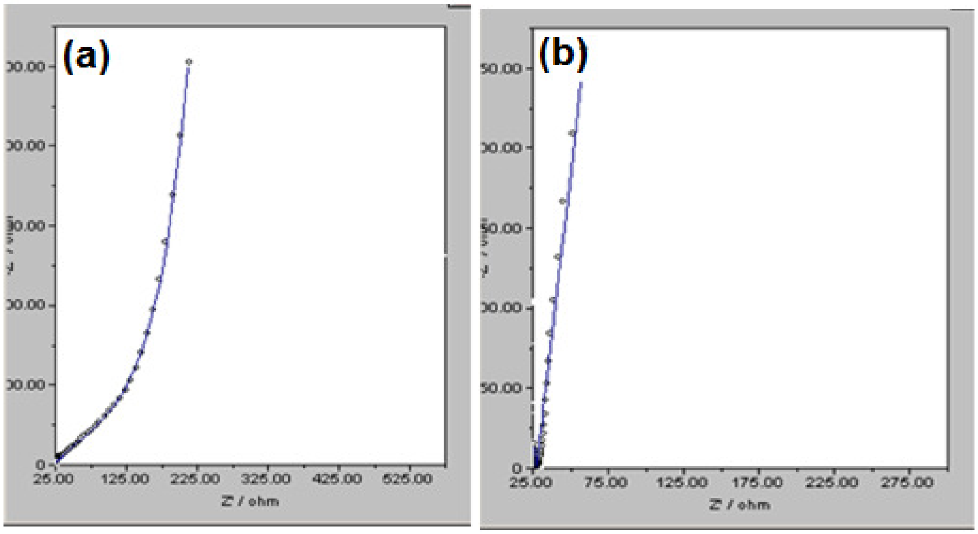

Figure 4.36 Nyquist plot of titania nanotubes in water at pH 2 (0.01 M H_2SO_4) at different applied potentials (a) 0 V and (b) - 0.6 V

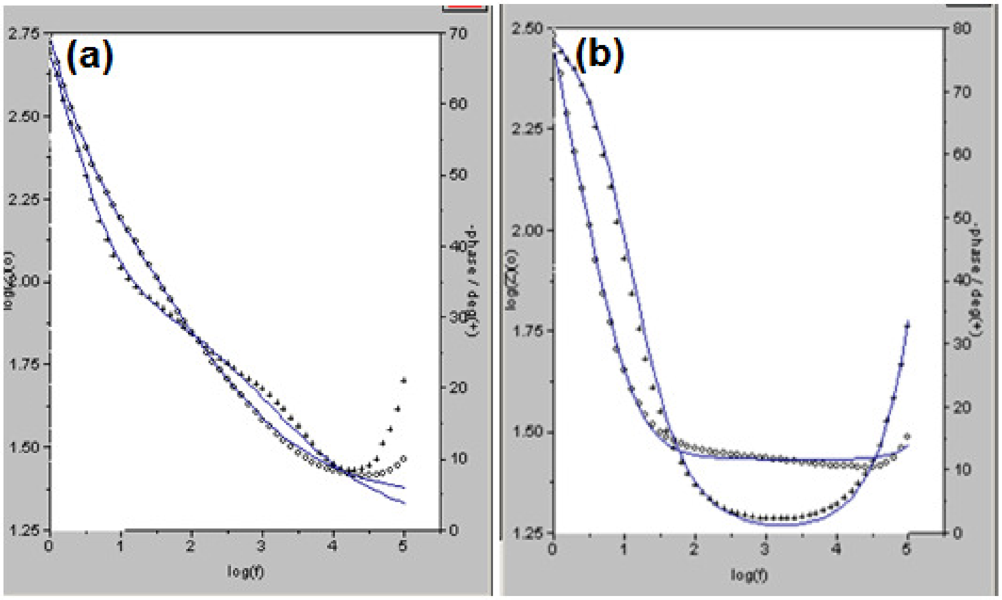

Figure 4.37 Bode plot of titania nanotubes in water at pH 2 (0.01 M H_2SO_4) at different applied potentials (a) 0 V and (b) - 0.6 V

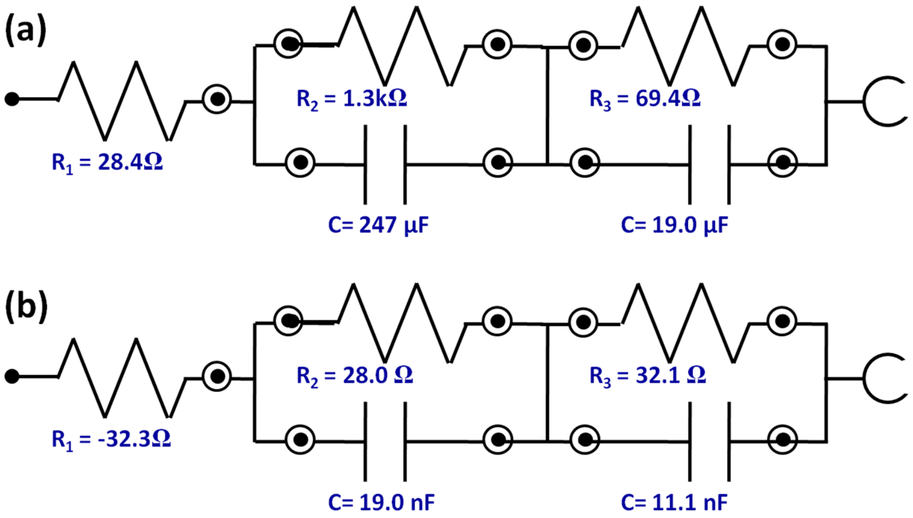

Figure 4.38 Circuit used to fit experimental results and circuit paramaters obtained after fitting for different applied potentials. (a) 0 V and (b) – 0.6 V

From the circuit, R1 is referred to as electrolyte resistance, R2 is the resistance of compact oxide at the bottom of the nanotubes and R3 is the resistance between the titania nanotube wall and the electrolyte (Munoz et al., 2007). The circuit parameters obtained after fitting of the EIS for different applied potentials are also shown in Figure 4.38. From the figure, the resistance of R2 and R3 of 0 V (Figure 4.38a) are reduced from 1.3 kΩ to 28 Ω and from 69.4 Ω to 32.1 Ω, respectively after the applied potential is changed from 0 V to - 0.6 V. This reduction shows the influence of the flat-band potential on changing the resistance of titania nanotubes from high resistance to low resistance. At the more negative than the flat-band potential, more electrons will be accumulated at the nanotubes, thus increasing the conductivity of the titania nanotubes. The titania nanotubes changed from blocking electrodes at low bias to passing electrodes at high bias where a Faradaic reaction takes place. At the more negative potential than the flat-band potential, proton intercalation also occurs. This phenomenon explains a larger cathodic area obtained in all the CV curves for the titania nanotubes. This property can be exploited to increase the capacitance of the titania nanotubes especially in unsymmetrical supercapacitor application where the titania nanotubes is used only as a negative electrode.

4.7 The seventh project: Synthesis, characterization and electrochemical capacitance of NiO-Titania nanotubes composite for pseudocapacitor application based on fast surface redox

The titania nanotube was prepared using the anodization method in electrolyte containing 75 vol % glycerol, 25 vol % DI water and 0.5 wt% ammonium fluoride at 20 V for 1 hour. The titania nanotube was successfully deposited with NiO nanoparticles via potentiostatic electrodeposition at -1.25 V in 0.02 M $Ni(Ac)_2$ aqueous solution for 30 min. After electrodeposition, the samples were annealed at 200^{o}C for about 2 hours in a muffle furnace to convert the Ni to NiO nanoparticles. Figure 4.39 shows the potentiostatic electrodeposition curves of NiO nanoparticles onto titania nanotubes substrate surface. During the reduction reaction of nickel ions, the metallic nickel will be produced on the cathodic surface of the titania nanotubes substrate. The reduced nickel is then converted to NiO after the annealing regime (Xie et al., 2009; Prasad and Meura, 2004; Xing et al., 2004).

From the electrodeposition curve (Figure 4.39), the steady-state condition indicates that the electroreduction reaction had a very constant working potential throughout the potentiostatic process. As the standard redox potential is – 0.257 V versus NHE for Ni2+ +2e–→Ni and 0 V for 2H+ + 2e–→H2, this allows metallic nickel to be electrodeposited on the titania nanotube surface as well as the electrochemical formation of hydrogen under the experimental conditions mentioned above.

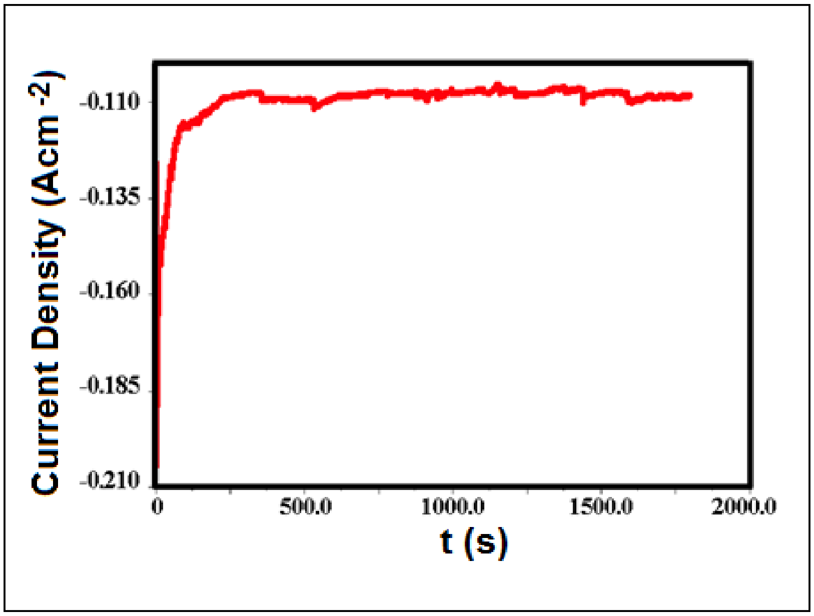

Figure 4.39 Potentiostatic curve of electrodeposition of NiO nanoparticles on titania nanotubes substrate

4.7.1 FESEM micrographs

Figure 4.40 shows an FESEM micrographs of titania nanotubes surface before and after NiO electrodeposition. From Figure 4.40(a), highly ordered, vertically oriented and well separated titania nanotubes were obtained after electrochemical anodization. The nanotubes are approximately 90 nm in diameter and 1 μm in length. After potentiostatic electrodeposition, the NiO particles were clearly observed as shown in Figure 4.40 (b). The spherical NiO particles are mostly deposited on the top of the nanotube opening and smaller sized NiO nanoparticles were also deposited inside the nanotubes as shown in Figure 4.41.

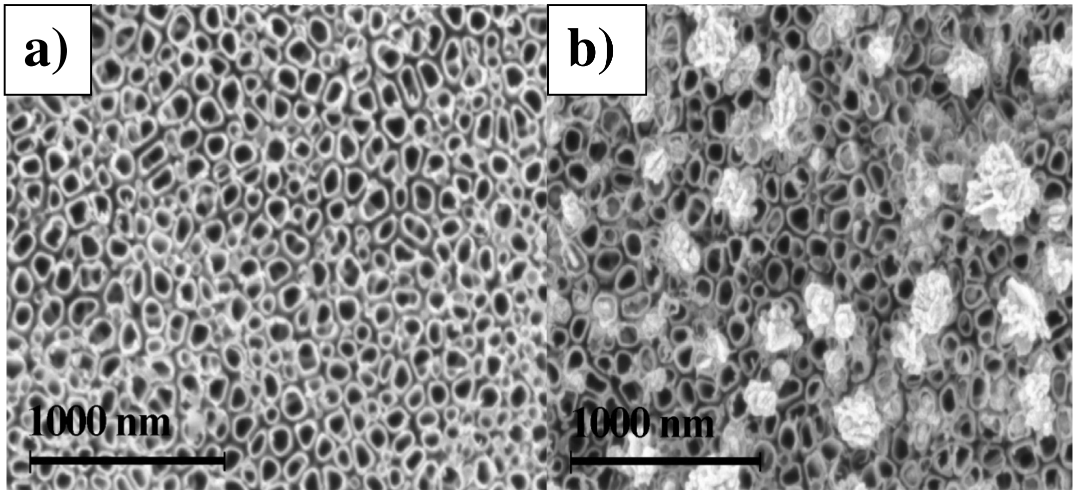

Figure 4.40 FESEM micrographs of titania nanotubes surface. (a) Before electrodeposition of NiO, (b) After electrodeposition of NiO

From a close up observation, the particles has nanoflake surface, thus increasing its specific surface area. This is a crucial characteristic because the capacitive behaviour in pseudocapacitor application is governed by area of the surface and reactivity of the surface of electroactive materials. For example, Lang et al, 2008 has made a comparison between two NiO morphologies (particles and nanoflakes). They found that the network-like structure which consists of interconnected nano-flakes shows anisotropic morphology characteristics and the formation of a loosely packed microstructure in the nanometer scale. The unique structure plays a basic role in the morphology requirement for electrochemical accessibility of electrolyte OH^- to the NiO active material and a fast diffusion rate within the redox phase. In addition, it is believed that different structures might lead to different electrochemical behaviour (Jiang et al., 2011). These results suggest the importance of rational design and synthesis of ultrathin nanomaterials for high-performance energy applications.

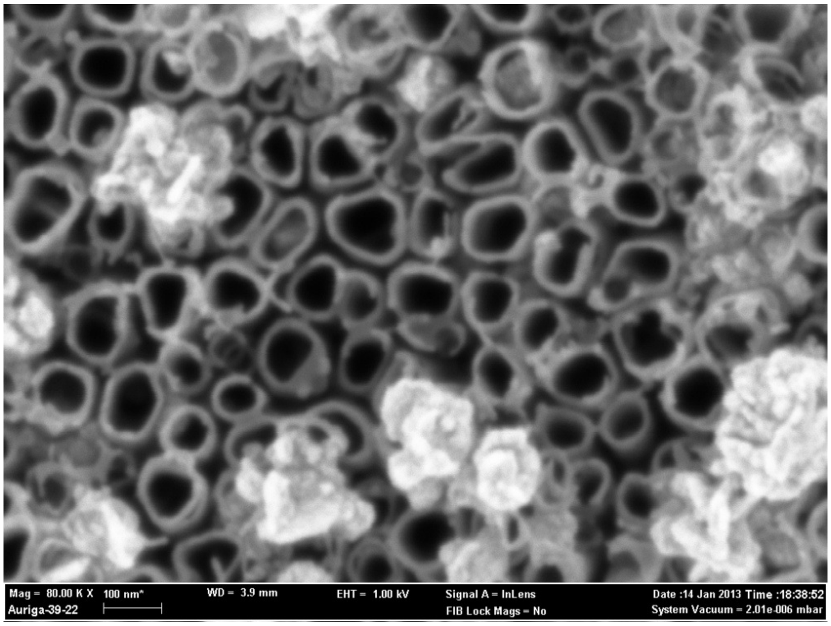

Figure 4.41 Nickel oxide nanoparticles loaded on pore opening and inside the titania nanotubes

4.7.2 X-ray diffractogram

Figure 4.42 shows the overlaid XRD pattern for titania nanotubes and titania nanotubes-NiO composite. Owing to the same substrate materials, both titania nanotubes and titania nanotubes-NiO composites have similar characteristic diffraction peaks at $2\theta=25.4^{o}$ of *h k l* (101), 48.2^{o} of *h k l* (200) planes for anatase titania and 40.4^{o} of *h k l* (101), 38.5^{o} of *h k l* (002) planes for crystallized Ti metal. Compared with titania nanotubes graph, titania nanotubes-NiO curve exhibit novel characteristic peaks at $2\theta=43.5°$ of *h k l* (2 0 0) and $37.5°$ of *h k l* (1 1 1) planes, which is fully attributed to NiO crystal with cubic syngony (Xie et al., 2008).

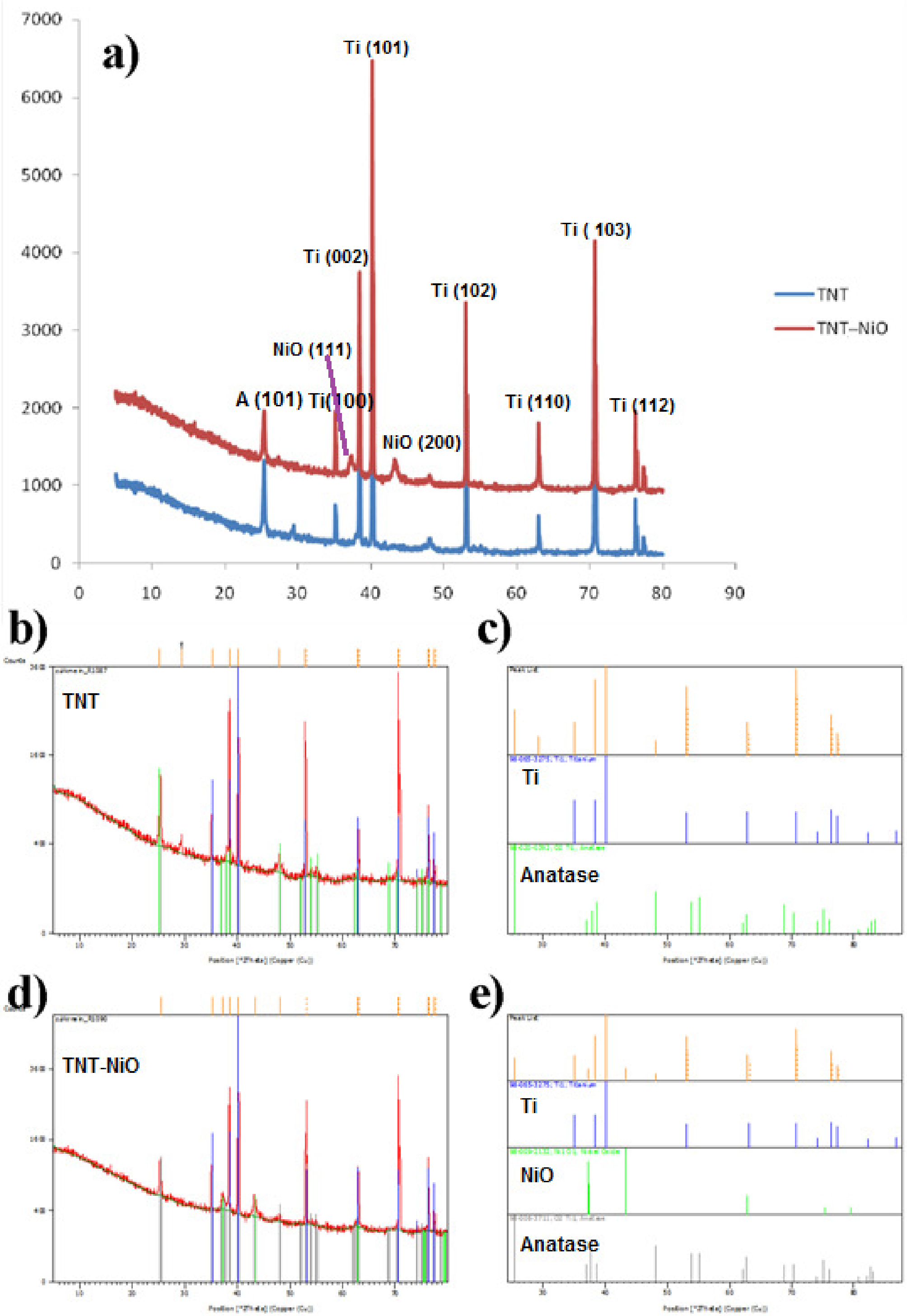

Figure 4.42 XRD pattern for titania nanotubes and titania nanotubes-NiO composite (a) Overlay XRD curve, (b,c) titania nanotubes and (c,e) titania nanotubes-NiO

4.7.3 Cyclic voltammogram

Figure 4.43 shows the cyclic voltammetry of titania nanotubes and titania nanotubes-NiO in 1 M KOH scan from 0 V to 0.6 V using scan rates of 5 mV s^{-1} to 70 mV s^{-1}. From the CV plot of titania nanotubes (Figure 4.43a), no redox peak is found suggesting that the charge storage mechanism mainly comes from electrical double layer or non-faradaic adsorption of OH^-. However, redox peak is observed for the CV plots of titania nanotubes-NiO at about 0.48 V and 0.16 V (Figure 4.43b). This characteristic is associated to the production of nickel oxy-hydroxide and its reversible exchange to the product of nickel oxide, where the equivalent electrode reaction is shown as

$$NiO + zOH^- - ze^- \leftrightarrow NiO(OH) + (1-z)NiO + ze^-$$

Based on the calculation described in previous project, electrochemical capacitance of titania nanotubes improved from 0.42 mF cm^{-2} to 4.65 mF cm^{-2}. This value is lower than that reported by Xie et al. (2008) mainly due to less nickel oxide loading on the titania nanotubes electrode.

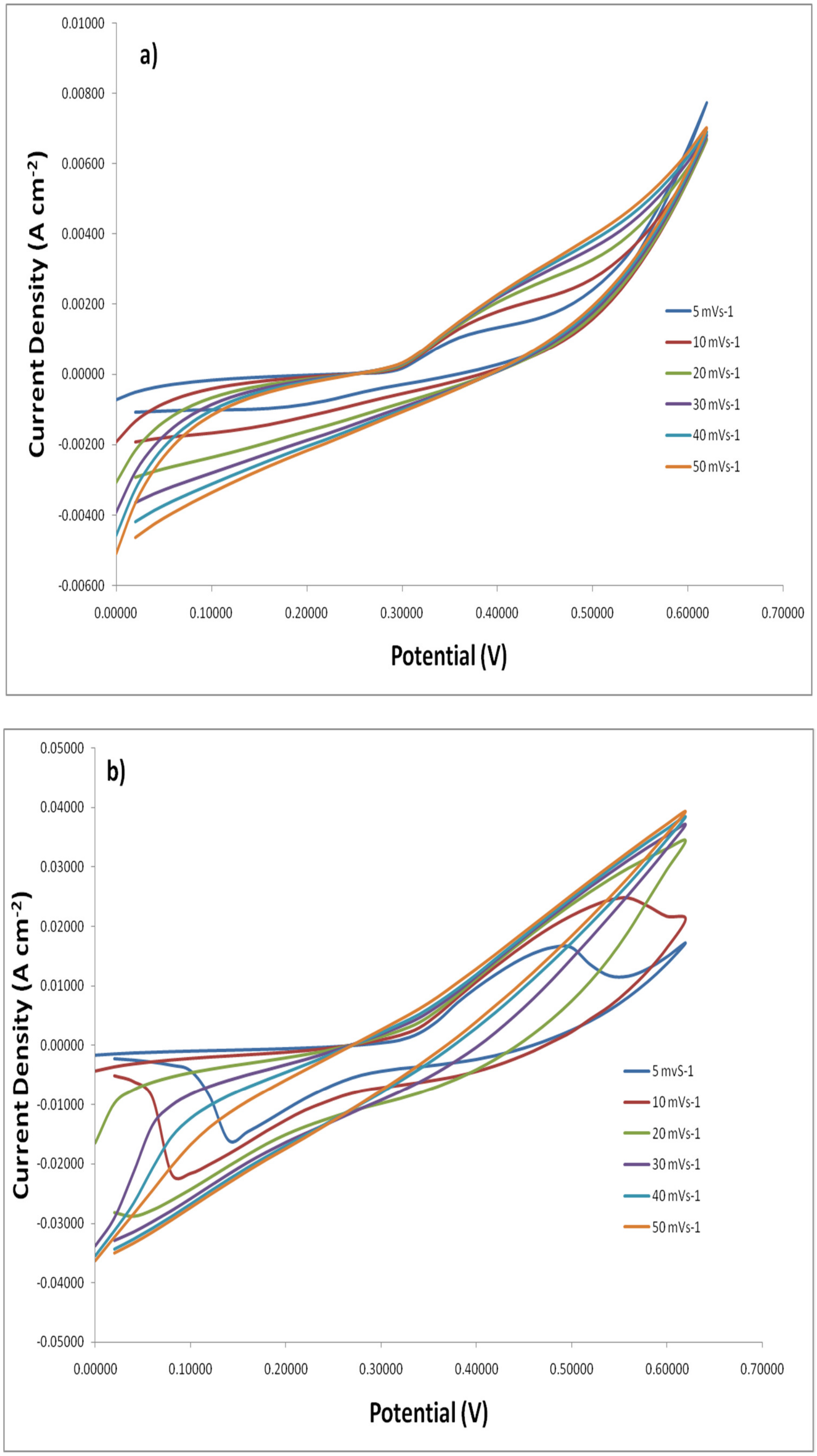

Figure 4.43 Cyclic voltammogram of titania nanotubes and titania nanotubes/NiO composite in 1 M KOH using scan rates from 5 mV s^{-1} to 50 mV s^{-1} at potential scans from 0 V to 0.6 V

CHAPTER 5

5.1 CONCLUSION & SUGGESTION FOR FUTURE WORKS

Throughout the thesis, synthesis and characterization of anodized titania nanotubes for supercapacitor application has been studied and covered in seven separate projects. The conclusion of each project is listed as follows.

1) Highly-ordered and vertically oriented titania nanotubes were succesfully synthesized using electrochemical anodization under optimum conditions in electrolyte containing ethylene glycol, 0.5 wt % ammonium flouride and 2 vol % DI water. The nanotubes were 1.2 µm in length, 60 nm in diameter and 15 nm in wall thickness. The chemical composition and crystal structure have been investigated after annealing in low vacuum furnace from 300 °C to 600 °C. Based on EDX, the annealing temperature and the low vacuum annealing used in this study is not sufficient to induce non-stoichiometric and point defect.

   Exposure to the environment during sample handling will refill the vacated O-element after low vacuum annealing. XPS was used to confirm the EDX results where no Ti^{3+} shoulder at lower binding energy on the Ti $2p_{3/2}$ is detected. XRD results showed that the anatase structure found for the samples were between 300 °C to 500 °C. Above that temperature ranges, the rutile structure started to appear. Based on this project, the selection of annealing temperature, duration and annealing gas is important in tuning the surface morphology, crystal structure and chemical composition of titania nanotubes for supercapacitor.

2) The formation of titania nanotubes can be explained in stages. In the initial stage, a compact oxide layer with nanoscale pit formation takes place. Then, the pits transform into larger and deeper pores with an increase in the anodization time due to the integration of the smaller pores with the larger ones, finally creating the self-ordered titania nanotubes. The effect of anodized titania surface on electrochemical capacitance improvement of titania material was investigated by cyclic voltammetry. The porous structure of the nanotubes increased the electrochemical capacitance from 18.3 μF cm^{-2} for 10 s sample anodization time to 49.9 μF cm^{-2} for 1800 s sample. The CV shape changes from a nearly symmetrical rectangular shape to an x-axis symmetry with higher current density as the anodization duration increases due to the enhanced specific surface area of the nanotubular structure. However, changing the surface morphology alone will not significantly increase the specific capacitance as the material is still poorly electroactive for better charge storage properties.

3) Bamboo type titania nanotubes has been introduced to increase surface area of titania nanotubes. Although titania nanotubes exhibit excellent reversibility and fast charge–discharge behavior, the storage capacity is still much lower than that of other established materials due to low electrical conductivity of titania material itself. Annealing this material in NH_3 using optimized conditions will improve the electrochemical capacitance due to the oxygen vacancies and the reduction of Ti^{4+} to Ti^{3+}. Nitridation of this sample by NH_3 annealing at 500°C did not occur, which suggests that the larger electrochemical capacitance of this sample is due to the

electron donating effect. The introduction of surface defects by annealing in NH_3 increased the specific capacitance value from 52 μF cm^{-2} to 118 μF cm^{-2}.

4) Using experimental design of response surface methodology (RSM), we have shown that anodization parameter such as ammonium fluoride concentration is an important factor and contributes directly to higher discharge time and specific capacitance while a combination of ammonium fluoride and anodization time will produce longer nanotubes and contribute in high aspect ratio of anodic titania nanotubes. The Box-Behnken design is used to develop mathematical models for predicting the discharge time of titania nanotubes. By using desirability function to achieve maximum discharge time and recalculating all the contributed factors, specific capacitance of titania nanotubes improved from 105 μF cm^{-2} to 145.6 μF cm^{-2}. After investigation using FESEM, the sample that showed the highest specific capacitance has complete nanotube structure compared to the sample with the lowest capacitance.

5) Enhanced electrical double layer capacitance of anodized titania nanotubes using EMIM hydrogensulfate ionic liquid as electrolytes with a specific capacitance of 1.58 mF cm^{-2} has been achieved. This enhancement comes from two reasons. First, the ionic liquid electrolytes contain very high concentration of anion and cation, thus more charge are involved in storage activities. Second, the charge storage mechanism of titania in ionic liquid is different compared to that in aqueous electrolyte. The stacking double layer based on the theory of ionic overscreening and crowding has contributed in this enhancement. Morever, the use of EMIM hydrogensulfate as electrolytes for titania nanotube supercapacitor will promote

versatility to supercapacitor design due to the wide operating voltage up to 3.5 V of this ionic liquid compared with 1 V of aqueous electrolyte.

6) Flat-band potential study has been performed to justify the CV shapes of titania nanotubes. By using Mott-Schottky analysis in low molarity sulphuric acid at pH 2, flat-band potential of – 0.21 V has been obtained. This flat-band potential explained the n-type characteristics of titania nanotubes where larger cathodic CV area will always be found in all CV graphs. When the CV is scanned at a more negative potential than flat-band potential, conductivity of titania will increase. The capacitance increase is due to the unpinning of the Fermi level allowing the Fermi level to approach the conduction band. More electrons will be accumulated at the electrode surface, thus more counter ions will be attracted and higher electrochemical capacitance is obtained. This n-type characteristic can be exploited to achieve greater electrochemical capacitance especially in unsymmetrical supercapacitor applications.

7) Conversion of charge storage mechanism of titania nanotubes from the electrical double layer capacitance to the fast surface redox reaction was achieved by potentiostatic electrodeposition of nickel oxide into the nanotubes in 0.02 M nickel acetate for 30 minutes. By using FESEM, nickel oxide has nanoflakes surface thus contributed in increasing the specific surface area. Compared to the 2θ of titania nanotubes, NiO contained two new peaks at $2\theta=43.5\ ^{o}C$ and $37.5\ ^{o}C$ which can be ascribed to NiO with cubic syngony. After CV is scanned from 0 V to 0.6 V using a scan rate of 5 mV s^{-1} and to 70 mV s^{-1}, two redox peaks at 0.48 V and 0.16 V is obtained. This characteristic was associated with the formation of nickel oxy-hydroxide and its back conversion to nickel oxide product. The specific capacitance

of the electrode in 1 M KOH electrolyte has improved significantly from 0.42 mF cm^{-2} for titania nanotubes electrode to 4.65 mF cm^{-2} for titania nanotubes/NiO composite electrode.

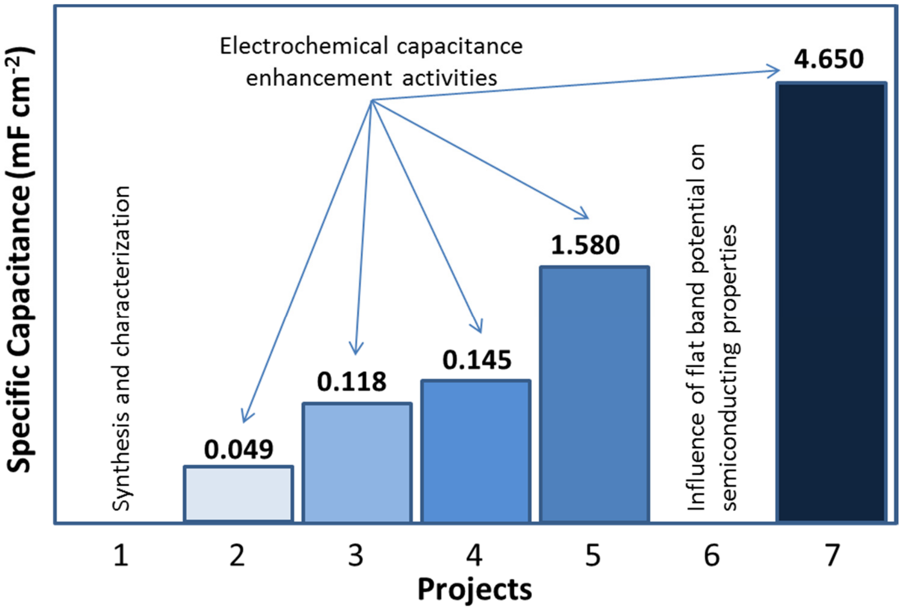

Figure 5.1 Specific electrochemical capacitance enhancement obtained for each project

From the conclusion of each project above, the objectives to synthesize and characterize titania nanotubes for supercapacitor application was successfully achieved. The electrochemical capacitance was greatly improved up to 4.65 mF cm^{-2} as shown in Figure 5.1. Furthemore, all the methods applied in this thesis can be applied in various types of supercapacitor applications such as in aqueous supercapacitor, low and high power supercapacitor, high energy supercapacitor, high voltage supercapacitor, redox type supercapacitor and unsymmetrical supercapacitor.

For future works, this proof of concepts can be packaged for the target application. The durability and reliability such as cyclability, coulombic efficiency and self-discharge can be further investigated in detail.

REFERENCES

Albu, S. P., Kim, D., & Schmuki, P. (2008). Growth of aligned TiO_2 bamboo-type nanotubes and highly ordered nanolace. Angewandte Chemie International Edition, 47, 1916 –1919.

Albu, S. P., Ghicov, A., Aldabergenova, S., Drechsel, P., LeClere, D., Thompson, G.E., Macak, J.M., & Schmuki, P. (2008). Formation of double-walled TiO_2 nanotubes and robust anatase membranes. *Advanced Materials*, 20, 4135-4139.

Albu, S. P., Tsuchiya, H., Fujimoto, S., & Schmuki, P. (2010). TiO_2 nanotubes – annealing effects on detailed morphology and structure. *European Journal of Inorganic Chemistry*, 27, 4351-4356.

Ali, G., Chen, C., Yoo, S. H., Kum, J. M., & Cho, S. O. (2011). Fabrication of complete titania nanoporous structures via electrochemical anodization of Ti. *Nanoscale Research Letters*, 6, 332-342.

Armstrong, R.D., Horrocks, B.R., (1997). The double layer structure at the metal-solid electrolyte interface, *Solid State Ionics,* 94, 181-187.

Bai, J., Zhou, B., Li, L., Liu, Y., Zheng, Q., Shao, J., Zhu, Y., Cai, W., Liao, J., Zou, L., (2008). The formation mechanism of titania nanotube arrays in hydrofluoric acid electrolyte, *Journal of Material Science*, 43, 1880–1884.

Beranek, R., Hildebrand, H., & Schmuki, P. (2003). Self-organized porous titanium oxide prepared in H_2SO_4/HF electrolytes. *Electrochemical and Solid-State Letter*, 6, B12-B14.

Beranek, R., Tsuchiya, H., Sugishima, T., Macak, J. M., Taveira, L., Fujimoto, S., Kisch, H., Schmuki, P., (2005). Enhancement and limits of the photoelectrochemical response from anodic TiO_2 nanotubes, *Applied Physic Letter*, 87, 243114.

Berger, S., Kunze, J., Schmuki, P., LeClere, D., Valota, A., Skeldon, P., Thompson, G.E. (2009). A lithographic approach to determine volume expansion factors during anodization: Using the example of initiation and growth of TiO_2-nanotubes, *Electrochimica Acta,* 54, 5942.

Bhargava, Y. V., Nguyen, Q. A. S., Devine, T. M., (2009). Initiation of organized nanopore/nanotube arrays in titanium oxide II. Nanopore size and spacing, *Journal of Electrochemical Society,* 156, E62.

Bonnefoi, L., Simon, P., Fauvarque, J. F., Sarrazin, C., & Dugast, A. (1999). Electrode compositions for carbon power supercapacitors. *Journal of Power Sources*, 79, 149-155.

Chau, T.N., Sung, Y.-T., Wang, B.-B., Yang, W.-D. (2012). Study on the photocatalytic degradation of methylene blue dye on titanate nanotube powders prepared by methanol-thermal process, *Applied Mechanics and Materials*, 234, 11-16.

Chang, J-K., Huang, C-H., Lee, M-T., Tsai, W-T., Deng, M-J., & Sun, I-W. (2009). Physicochemical factors that affect the pseudocapacitance and cyclic stability of Mn oxide electrodes. *Electrochimica Acta*, 54, 3278–3284.

Chen, J.S., Lou, X.W., (2009). The superior lithium storage capabilities of ultra-fine rutile TiO_2 nanoparticles, *Journal of Power Sources,* 195(9), 2905-2908

Choudhury, N.A., Sampath, A., Shukl, A.K., (2010). Hydrogel-polymer electrolytes for electrochemical capacitors: an overview. *Energy Environ. Sci.,* 2, 55–67

Conway, B.E., Birss, V., Wojtowicz, J., (1997). The role and utilization of pseudocapacitance for energy storage by supercapacitors, *Journal of Power Sources,* 66, 1-14.

Conway, B. E., (1999). Electrochemical Supercapacitors, Scientific Fundamentals and Technological Applications, Kluwer Academic/Plenum Publishers: New York, 221–241.

Conway, B.E., Pell, W.G., (2003). Double-layer and pseudocapacitance types of electrochemical capacitors and their applications to the development of hybrid devices, *Journal of Solid State Electrochemistry*, 7, 637–644.

Deng, L., Chen, Y., Yao, M., Wang, S., Zhu, B., Huang, W., Zhang, S., (2010). Synthesis, characterization of B-doped TiO_2 nanotubes with high photocatalytic activity, *Journal of Sol-Gel Science and Technology*, 53(3), 535-541.

Diebold, U., (2002). Structure and properties of TiO_2 surface; A brief review, *Applied Physics A*, A 76, 1-7.

Endut, Z., Hamdi, M., & Basirun, W.J. (2013). Pseudocapacitive performance of vertical copper oxide nanoflakes, *Thin Solid Films*, 528, 213–216.

Fabregat-Santiago, F., Mora-Sero, I., Garcia-Belmonte, G., & Bisquert, J. (2003). Cyclic voltammetry studies of nanoporous semiconductors. Capacitive and reactive properties of nanocrystalline TiO_2 electrodes in aqueous electrolyte, *Journal of Physical Chemistry B*, 107, 758-768.

He, Y-B., Li, G-R., Wang, Z-L., Su, C-Y., & Tong, Y-X., (2011). Single-crystal ZnO nanorod/amorphous and nanoporous metal oxide shell composites: Controllable electrochemical synthesis and enhanced supercapacitor performances. *Energy and Environmental Science*, 4, 1288–1292.

Jha, H., Hahn, R., & Schmuki, P. (2010). Ultrafast oxide nanotube formation on TiNb, TiZr and TiTa alloys by rapid breakdown anodization. *Electrochimica Acta*, 55, 8883-8887.

Jiang, H., Zhao, T., Ma, J., Yan, C., & Li, C. (2011). Ultrafine manganese dioxide nanowire network for high-performance supercapacitors. *Chemistry Communications*, 47, 1264–1266.

Jiang, H., Zhao, T., Li, C., & Ma, J. (2011). Hierarchical self-assembly of ultrathin nickel hydroxide nanoflakes for high-performance supercapacitors. *Journal of Materials Chemistry*, 21, 3818–3823.

Jiang, R., Huang, T., Liu, J., Zhuang, J., & Yu, A. (2009). A novel method to prepare nanostructured manganese dioxide and its electrochemical properties as a supercapacitor electrode, *Electrochimica Acta*, 54, 3047–3052.

Kim, J-H., Zhu, K., Yan, Y., Perkins, C. L., & Frank, A. J. (2010). Microstructure and pseudocapacitive properties of electrodes constructed of oriented NiO-TiO_2 nanotube arrays, *Nano Letters*, 10, 4099–4104.

Kim, J.K., Zhu, K., Yan, Y., Perkins, C., Frank, A.J., (2010). Microstructure and pseudocapacitive properties of electrodes constructed of oriented NiO-TiO_2 nanotube arrays, *Nano Letters*, 10, 4099–4104.

Kim, J-H., Kang, S. H., Zhu, K., Kim J. Y., Neale, N. R., & Frank, A. J. (2011). Ni–NiO core–shell inverse opal electrodes for supercapacitors. *Chemistry Communications*, 47, 5214–5216.

Kubiak, P., Pfanzelt, M., Geserick, J., Hörmann, U., Hüsing, N., Kaiser, U., Wohlfahrt-Mehrens, M. (2009). Electrochemical evaluation of rutile TiO_2 nanoparticles as negative electrode for Li-ion batteries, *Journal of Power Sources,* 194(2), 1099-1104.

Kornyshev, A., Fedorov, M., (2008). Ionic Liquid Near a Charged Wall: Structure and Capacitance of Electrical Double Layer, *The Journal of Physical Chemistry B*, 112(28), 11868–11872.

Kotz, R., Carlen, M., (2000). Principles and applications of electrochemical capacitors, *Electrochimica Acta*, 45, 2483–2498.

Krause, S. (2007). Impedance Methods, *Encyclopedia of Electrochemistry,* 196-228.

Lai, Y. K., Huang, J-Y., Zhanga, H-F., Subramaniam, V-P., Tang, Y-X., Gong, D-G., Lokhande, C. D., Dubal, D. P., & Joo, O.-S. (2011). Metal oxide thin film based supercapacitors *Current Applied Physics*, 11, 255-270.

Lang, J-W., Kong, L-B., Wu, W-J., Luo, Y-C., & Kang, L. (2008). Facile approach to prepare loose-packed NiO nano-flakes materials for supercapacitors, *Chemistry Communications*, 4213–4215.

Lang, J., Yan, X., & Xue, Q. (2011). Facile preparation and electrochemical characterization of cobalt oxide/multi-walled carbon nanotube composites for supercapacitors, *Journal of Power Sources*, 196, 7841– 7846.

Lee, J., Ju, H., Lee, J.K., Kim, H.S., Lee, J. (2010). Atomic layer deposition of TiO_2 nanotubes and its improved electrostatic capacitance. *Electrochemistry Communications,* 12(2), 210-212.

Lee, J., Jho, J.Y., (2011). Fabrication of highly ordered and vertically oriented TiO_2 nanotube arrays for ordered heterojunction polymer/inorganic hybrid solar cell, *Solar Energy Materials and Solar Cells*, 95(11), 3152-3156.

Lewandowski, A., Galin´ski, M., (2004). Carbon–ionic liquid double-layer capacitors, *Journal of Physics and Chemistry of Solids,* 65, 281–286.

Liu, R., Hsieh, C. H., Yang, W. D., Qiang, L. S., Wu, J. F., (2011). Applying the statistical experimental method to evaluate the process conditions of TiO_2 nanotube arrays by anodization method. *Current Applied Physics*, 11, 1294–1298.

Liu, R., Duay, J., Lee, S.B., (2011). Heterogeneous nanostructured electrode materials for electrochemical energy storage. *Chemical Communications,* 47, 1384–1404.

Liu, X., Liu, Z., Zheng, J., Yan, X., Li, D., Chen, S., Chu, W., (2011). Characteristics of N doped TiO_2 nanotube arrays by N_2-plasma for visible light-driven photocatalysis, *Journal of Alloys and Compounds* 509, 9970– 9976.

Lokhande, C.D., Dubal, D.P., Joo, O.S., (2011). Metal oxide thin film based supercapacitors, *Current Applied Physics*, 11, 255-270.

Lu, X., Wang, G., Zhai, T., Yu, M., Gan, J., Tong, Y., & Li, Y. (2012). Hydrogenated TiO_2 Nanotube Arrays for Supercapacitors, *Nano Letters*, 12, 1690−1696.

Macak, J. M., Gong, B. G., Hueppe, M., & Schmuki, P. (2007). Filling of TiO_2 nanotubes by self-doping and electrodeposition, *Advanced Materials*, 19, 3027–3031.

Macak, J.M., Tsuchiya, H., Taveira, L., Aldabergerova, S., & Schmuki, P. (2005). Smooth anodic TiO_2 nanotubes, *Angewandte Chemie*, 117, 7629–7632.

Macak, J.M., Schmuki, P., (2006). Anodic growth of self-organized anodic TiO_2 nanotubes in viscous electrolytes, *Electrochimica Acta,* 52, 1258–1264.

Masuda, H., Fukuda*, K., (1995).* Ordered metal nanohole Arrays by two-step replication of honeycombstructure of anodic alumina, *Science, 268*, *1466*-1468.

Meher, S. K., Justin, P., & Rao, G. R. (2011). Nanoscale morphology dependent pseudocapacitance of NiO: Influence of intercalating anions during synthesis, *Nanoscale*, 3, 683–692.

Mi, L., Xu, P., Wang, P.N., (2008). Experimental study on the bandgap narrowings of TiO_2 films calcined under N_2 or NH_3 atmosphere, *Applied Surface Science,* 255, 2574-2580.

Mohapatra, S. K., Raja, K. S., Misra, M., Mahajan, V.K., & Ahmadian, M. (2007). Synthesis of self-organized mixed oxide nanotubes by sonoelectrochemical anodization of Ti–8Mn alloy. *Electrochimica Acta*, 53, 590-597.

Mor, G.K., Varghese, O.K., Paulose, M., Mukherjee, N., Grimes, C.A., (2003). Fabrication of tapered, conical-shaped titania nanotubes, *Journal of Material Research*, 18, 11.

Mor, G. K., Shankar, K., Paulose, M., Varghese, O.K., Grimes, C.A., (2005). Enhanced photocleavage of water using titania nanotube arrays, *Nano Letters*, 5, 191-195.

Mor, G.K., Shankar, K., Paulose, M., Varghese, O.A., Grimes, C.A., (2006). Use of highly-ordered TiO_2 nanotube arrays in dye-sensitized solar cells, *Nano Letters*, 6, 215-218.

Mor, G.K., Varghese, O.K., Paulose, M., Shankar, K., Grimes, C.A., (2006). A review on highly ordered, vertically oriented TiO_2 nanotube arrays: Fabrication, material properties, and solar energy applications, *Solar Energy Materials & Solar Cells*, 90, 2011–2075.

Munoz, A.G., Chen, Q., Schmuki., P. (2007). Interfacial properties of self –organized TiO_2 nanotubes studied by impedance spectroscopy, *Journal of Solid State Electrochemistry*, 11, 1077-1084.

Munoz, A.G., (2007). Semiconducting properties of self-organized TiO2 nanotubes, *Electrochimica Acta*, 52, 4167-4176.

Pan, X., & Ma, X., (2004). Phase transformations in nanocrystalline TiO_2 milled in different milling atmospheres. *Journal of Solid State Chemistry*, 177, 4098–4103.

Pandolfo, A.G., Hollenkamp, A.F., (2006). Carbon properties and their role in supercapacitors, *Journal of Power Sources*, 157,11.

Paramasivam, I., Macak, J.M., Selvam, T., Schmuki, P.,(2008). Electrochemical synthesis of self-organized TiO_2 nanotubular structures using an ionic liquid (BMIM-BF4), *Electrochimica Acta*, 54, 643–648.

Park, K.-H., Jin, E.M., Gu, H.B., Shim, S.E., Hong, C.K. (2009). Effects of HNO_3 treatment of TiO_2 nanoparticles on the photovoltaic properties of dye-sensitized solar cells, *Materials Letters,* 63 (26), 2208-2211.

Patake, V. D., Pawar, S. M., Shinde, V. R., Gujar, T. P., & Lokhande, C. D. (2010). The growth mechanism and supercapacitor study of anodically deposited amorphous ruthenium oxide films. *Current Applied Physics*, 10, 99–103.

Prasad, K. R., & Miura, N. (2004). Electrochemically deposited nanowhiskers of nickel oxide as a high-power pseudocapacitive electrode. *Applied Physics Letter*, 85, 4199–4201.

Qiu, J., Yu, W., Gao, X., Li, X. (2006). Sol-gel assisted ZnO nanorod array template to synthesize TiO_2 nanotube arrays, *Nanotechnology*, 17(18), 4695-4698.

Qiu, J., Yu, W., Gao, X., Li, X. (2007). Fabrication and characterization of TiO_2 nanotube arrays having nanopores in their walls by double-template-assisted sol-gel, *Nanotechnology*, 18(29), 295604.

Raja, K. S., Gandhi, T., & Misra, M. (2007). Effect of water content of ethylene glycol as electrolyte for synthesis of ordered titania nanotubes. *Electrochemistry Communications*, 9, 1069–1076.

Roy, P., Berger, S., & Schmuki. P. (2011). TiO_2 nanotubes: synthesis and applications. *Angewandte Chemie International Edition*, 50, 2904-2939.

Roy, P., Kim, D., Lee, K., Spiecker, E., Schmuki, P., (2010). TiO_2 nanotubes and their application in dye-sensitized solar cells, *Nanoscale*, 2, 45-59.

Sakai, N., Ebina, Yasuo., Takada,K., Sasaki, T., (2004). Electronic band structure of titania semiconductor nanosheets revealed by electrochemical and photoelectrochemical studies, *Journal of the American Chemical Society*, 126, 5851-5858.

Salari, M., Aboutalebi, S. H., Konstantinov, K., & Liu, H. K. (2011). A highly ordered titania nanotube array as a supercapacitor electrode, *Physical Chemistry Chemical Physics*, 13, 5038–5041

Salari, M., Konstantinov, K., & Liu, H. K., (2011). Enhancement of the capacitance in TiO2 nanotubes through controlled introduction of oxygen vacancies. *Journal of Materials Chemistry*, 21, 5128–5133.

Santara, B., Giri, P.K, (2013). Impact of reaction temperature, stirring and co-solvent on the solvothermal synthesis of anatase TiO_2 and TiO_2/titanate hybrid nanostructures: Elucidating the growth mechanism, *Materials Chemistry and Physics*, 137 (3), 928-936.

Santiago, F.F., Randriamahazaka, R. Zaban, A., Bisquert, J., (2006). Chemical capacitance of nanoporous-nanocrystalline TiO_2 in a room temperature ionic liquid, *Physical Chemistry Chemical Physics*, 8, 1827–1833.

Santiago, F.F., Eva, M.B., Bisquert, J., Mor, G.K., Shankar, K., Grimes, C.A., (2008). High carrier density and capacitance in TiO_2 nanotube arrays induced by electrochemical doping, *Journal of American Chemistry Society*, 130, 11312-11316.

Shannon, R. D., & Pask, J. A., (1965). Kinetics of the anatase-rutile transformation. *Journal of The American Ceramic Society*, 48, 391–398.

Shankar, K., Basham, J.I., Allam, N.K., Varghese, O.K., Mor, G.K., Feng, F., Paulose, M., Seabold, J.A., Choi, C.S., Grimes, C.A., (2009). Recent advances in the use of TiO_2 nanotube and nanowire arrays for oxidative photoelectrochemistry, *Journal of Physical Chemistry C, 113,* 6327-6359.

Sharma, P., Bhatti, T.S., (2010). A review on electrochemical double-layer capacitors. *Energy Conversion and Management*, 51, 2901–2912.

Stoller, M.D., Park, S., Zhu, Y., An, J., Ruoff, R.S. (2008). Graphene-based ultracapacitors, *Nano Letter*, 8, 10.

Sun, L. Zhang, S., Sun, X., He, X., (2010). Effect of the Geometry of the Anodized Titania Nanotube Array on the Performance of Dye-Sensitized Solar Cells, *Journal of Nanoscience and Nanotechnology*, 10, 4551-4561.

Sundar, L., Sun, L., Chen, Z., & Lin, C-J. (2010). Nitrogen-doped TiO_2 nanotube array films with enhanced photocatalytic activity under various light sources, *Journal of Hazardous Materials* 184, 855–863.

Toupin, M., Brousse, T., & Be´langer, D. (2002). Influence of microstucture on the charge storage properties of chemically synthesized manganese dioxide. *Chemistry of Materials*, 14, 3946-3952.

Taveira, L. V., Macak, J. M., Tsuchiya, H., Dick, L. F. P., Schmuki, P., (2005) Initiation and growth of self-organized TiO_2 nanotubes anodically formed in $NH_4F/(NH_4)_2SO_4$ electrolytes, *Journal of Electrochemical Society*, 152, B405.

Wang, H., Pilon, L., (2011). Accurate simulations of electric double layer capacitance of ultramicroelectrodes, *Journal of Physical Chemistry C*, 115(33), 16711-16719.

Wang, J., Polleux, J., Lim, J., Dunn, B., (2007). Pseudocapacitive contributions to electrochemical Energy Storage in TiO_2 (anatase) nanoparticles, *Journal of Physical Chemistry C*, 111, 14925−14931.

Wua, C-M., Fan, C-Y., Sun, I-W., Tsai, W-T., & Chang, J-K. (2011). Improved pseudocapacitive performance and cycle life of cobalt hydroxide on an electrochemically derived nano-porous Ni framework, *Journal of Power Sources*, 196, 7828– 7834.

Xia, X-H., Tu, J-P., Mai, Y-J., Wang, X-L. Gu, C-D., Zhao, X-B. (2011). Self-supported hydrothermal synthesized hollow Co_3O_4 nanowire arrays with high supercapacitor capacitance. *Journal of Materials Chemistry*, 21, 9319–9325.

Xiao, P., Fang, H., Cao, G., Zhang, Y., Zhang, Z., (2010). Effect of Ti^{n+} defects on electrochemical properties of highly-ordered titania nanotube arrays, *Thin Solid Films*, 518, 7152-7155.

Xiao, P., Zhang, Y., & Cao, G. (2011). Effect of surface defects on biosensing properties of TiO2 nanotube arrays, *Sensors and Actuators B*, 155, 159–164.

Xie, K., Li, J., Lai, Y., Lu, W., Zhang, Z., Liu, Y., Zhou, L., & Huang, H. (2011). Highly ordered iron oxide nanotube arrays as electrodes for electrochemical energy Storage. *Electrochemistry Communications*, 13, 657–660.

Xie, Y., Huang, C., Zhou, L., Liu, Y., & Huang, H. (2009). Supercapacitor application of nickel oxide–titania nanocomposites. *Composites Science and Technology*, 69, 2108–2114.

Xie, Y., & Fu, D. (2010). Photochemical performance and electrochemical capacitance of titania nanocomplexes. *Materials Research Bulletin*, 45, 628–635.

Xie, Y., & Fu, D. (2010). Supercapacitance of ruthenium oxide deposited on titania and titanium substrates, *Materials Chemistry and Physics*, 122, 23–29.

Xie, Y., Zhou, L., Huang, C., Huang, H., Lu, J., (2008). Fabrication of nickel oxide-embedded titania nanotube array for redox capacitance application, *Electrochimica Acta*, 53, 3643–3649.

Xing, W., Li, F., Yan, Z. F., & Lu, G. Q. (2004). Synthesis and electrochemical properties of mesoporous nickel oxide. *Journal of Power Sources*, 134, 324–330.

Xu, N., Riley, J., (2011). Nonlinear analysis of a classical system: The double-layer capacitor, *Electrochemistry Communications*, 13(10), 1077-1081.

Yang, Y., Kim, D., Yang, M., Schmuki, P., (2011). Vertically aligned mixed V_2O_5–TiO_2 nanotube arrays for supercapacitor applications, *Chemical Communications*, 47, 7746-7748.

Yasuda, K., Macak, J. M., Berger, S., Ghicov, A., Schmuki, P., (2007). Mechanistic aspects of the self-organization process for oxide nanotube formation on valve metals, *Journal Electrochemistry Society*, 154, C472.

Yoon, S., Kang, E., Kim, J. K., Lee, C. W., & Lee, J. (2011). Development of high-performance supercapacitor electrodes using novel ordered mesoporous tungsten oxide materials with high electrical conductivity. *Chemistry Communications*, 47, 1021–1023.

Yu, H., Ma, J., Zhang, Y., Zhang, X., & Shi, W. (2011). Cyclic voltammetry studies of TiO_2 nanotube arrays electrode: Conductivity and reactivity in the presence of H^+ and aqueous redox systems. *Electrochimica Acta*, 56, 6498– 6502.

Zeng, Q.G., Zhang, Z.M., Ding, Z.J., Wang, Y., Sheng, Y.Q. (2007). Strong photoluminescence emission of Eu:TiO_2 nanotubes, *Scripta Materialia*, 57 (10), 897-900.

Zhang, Y., Feng, H., Wu, X., Wang, L., Zhang, A., Xia, T., Dong, H., Li, X., & Zhang, L. (2009). Progress of electrochemical capacitor electrode materials: A review. *International journal of hydrogen energy*, 34, 4889–4899.

Zhang, Z., Wang, X., Long, J., Gu, Q., Ding, Z., & Fu, X. (2010). Nitrogen-doped titanium dioxide visible light photocatalyst: Spectroscopic identification of photoactive centers, *Journal of Catalysis*, 276, 201–214.

Zwilling, V., Aucouturier, M., Ceretti, E.D., (1999). Anodic oxidation of titanium and TA6V alloy in chromic media. An electrochemical approach, *Electrochimica Acta*, 45, 921.

Zwilling, V., Ceretti, E.D., Forveille, A.B., David, D., Perrin, M. Y., Aucouturier, M., (1999). Structure and physicochemistry of anodic oxide films on titanium and TA6V alloy. *Surface Interface Analysis*, 27, 629.

APPENDIX A - List of Publications

1) Zulkarnain Endut, Mohd Hamdi Abd Shukor, Wan Jeffrey Basirun, "*Supercapacitance of bamboo-type anodic titania nanotube arrays*" Surface & Coatings Technology 215 (2013) 75–78

2) Zulkarnain Endut, Mohd Hamdi Abd Shukor, Wan Jeffrey Basirun, "*Pseudocapacitive performance of vertical copper oxide nanoflakes*", Thin Solid Films 528 (2013) 213–216

3) Zulkarnain Endut, Mohd Hamdi Abd. Shukor, Wan Jeffrey Basirun, "*An investigation on formation and electrochemical capacitance of anodized titania nanotubes*," Applied Surface Science 280 (2013) 962– 966

4) Zulkarnain Endut, Mohd Hamdi Abd. Shukor, Wan Jeffrey Basirun, "*Optimization and functionalization of anodized titania nanotubes for redox supercapacitor*", Thin Solid Films 549 (2013) 306–312